

Spring 2020

Remote Sensing and Social Sensing for Improved Flood Awareness and Exposure Analysis in the Big Data Era

Xiao Huang

Follow this and additional works at: <https://scholarcommons.sc.edu/etd>



Part of the [Geography Commons](#)

Recommended Citation

Huang, X.(2020). *Remote Sensing and Social Sensing for Improved Flood Awareness and Exposure Analysis in the Big Data Era*. (Doctoral dissertation). Retrieved from <https://scholarcommons.sc.edu/etd/5851>

This Open Access Dissertation is brought to you by Scholar Commons. It has been accepted for inclusion in Theses and Dissertations by an authorized administrator of Scholar Commons. For more information, please contact digres@mailbox.sc.edu.

REMOTE SENSING AND SOCIAL SENSING FOR IMPROVED FLOOD AWARENESS
AND EXPOSURE ANALYSIS IN THE BIG DATA ERA

by

Xiao Huang

Bachelor of Engineering
Wuhan University, 2015

Master of Science
Georgia Institute of Technology, 2016

Submitted in Partial Fulfillment of the Requirements

For the Degree of Doctor of Philosophy in

Geography

College of Arts and Sciences

University of South Carolina

2020

Accepted by:

Cuizhen Wang, Major Professor

Zhenlong Li, Committee Member

Michael E. Hodgson, Committee Member

David B. Hitchcock, Committee Member

Cheryl L. Addy, Vice Provost and Dean of the Graduate School

© Copyright by Xiao Huang, 2020
All Rights Reserved.

DEDICATION

To my advisor, Dr. Cuizhen Wang.

To my wife, Meng Jin.

To my family.

To all who support me and doubt me.

To those suffered from the coronavirus.

ACKNOWLEDGEMENTS

First and foremost, I want to thank my advisor, Dr. Cuizhen Wang. You are an awesome mentor and have always been there for me. I would not have achieved this much if you had not been my advisor. I also want to thank my committee members Dr. Zhenlong Li, Dr. Michael Hodgson, and Dr. David Hitchcock, for your timely feedback and support throughout my entire Ph.D. career.

I want to thank Drs. Caroline Nagel and Kirstin Dow, and Jean Ellis for their support on writing recommendation letters, organizing student events, and forwarding opportunities to me constantly. To my friends and colleagues, thank you for supporting me all the way.

My Ph.D. journey is a dream full of blessings. It could not have been better.

ABSTRACT

Floods are among the most devastating hazards on Earth, posing great threats to a large amount of population in the world. As the severity and frequency of flood events have noticeably increased, there is a growing need to improve the flood awareness and exposure analysis to assist flood mitigation. Fortunately, the Era of Big Data has fostered many innovative spatial data sources as well as spatial data analytics. This dissertation advances the existing flood monitoring studies by obtaining enhanced flood awareness via the development of a data fusion enable and deep learning supported flood monitoring framework that systematically integrates remotely sensed observation with in situ documentation from crowdsourcing platforms. In addition, this dissertation advances flood exposure studies via the application of long-term nighttime remote sensing series for the estimation of hurricane exposure in U.S Atlantic/Gulf coasts and the development of a spatially explicit population disaggregation method for comparative assessment of the exposed population within 100-year floodplains in the entire Conterminous United States (CONUS). In the Big Data Era, the important theoretical, methodological, and contextual knowledge gained in this study could greatly benefit local authorities and federal agencies for better preparedness of flood as well as other types of natural disasters in a geospatial framework.

TABLE OF CONTENTS

Dedication.....	iii
Acknowledgements.....	iv
Abstract.....	v
List of Tables	vii
List of Figures.....	ix
Chapter 1: Introduction.....	1
Chapter 2: Remote Sensing-Social Sensing Integrated Flood Modeling	5
Chapter 3: Deep Learning Supported Automatic Flood Relevant VGI Retrieval from Social Media Sources	29
Chapter 4: Hurricane-induced Disaster Exposure in the U.S. Atlantic/Gulf Coasts	64
Chapter 5: Benchmarking the Population Exposure to Flood Risks in the Conterminous U.S.....	92
Chapter 6: Conclusions.....	130
References.....	135
Appendix A: Supporting Tables	153
Appendix B: Manuscript Copyright Release	156

LIST OF TABLES

Table 2.1 Detailed statistics of five gauges	11
Table 2.2 The three DEM-reclassified categories in the research area based on the reference water height and maximum water height at each gauge.....	15
Table 2.3 The RFP and HWMs within USGS inundation area.	26
Table 3.1 Layer functionality summary.....	38
Table 3.2 Visual training set.....	45
Table 3.3 Textual training set	46
Table 3.4 Visual CNN performance	48
Table 3.5 Word2Vec training results (top 5 neighboring words with their cosine- similarity distances)	51
Table 3.6 Textual CNN performance.....	51
Table 3.7 Visual-textual fused classification accuracy.....	54
Table 3.8 Visual-textual fused classification compared with textual only	55
Table 4.1 DMSP/OLS Satellites and overlays in corresponding years	70
Table 4.2 DMSP/OLS NTL intercalibration coefficients	78
Table 4.3 Hurricane-prone zonal summary of Mann-Kendall and Theil-Sen test.....	85
Table 4.4 Sum of VANUI value and change percentage in the top 5 most populated MSAs in the north and south of the study area.....	88
Table 5.1 Summary of open access 100-year floodplain products used in this chapter.....	100
Table 5.2 Statistics of block group R (P_R) included in this chapter.....	104

Table 5.3 The top 10 ranked counties by the total population exposed to
100-year fluvial/pluvial and coastal floods (F/P + Coastal).....116

Table 5.4 The top 10 ranked counties by the proportion of the population exposed
to 100-year fluvial/pluvial and coastal floods (F/P + Coastal)116

LIST OF FIGURES

Figure 2.1 (a) Hurricane Joaquin; (b) Rainfall status in SC and the research area of this chapter.....	9
Figure 2.2 (a) The ALI image (panchromatic), locations of the verified tweets, and stream gauges; (b) Water height readings at the five stream gauges.	12
Figure 2.3 Methodology overview.....	14
Figure 2.4 The IFP derived from DEM and gauges. The background is the black-and-white display of the ALI image.	20
Figure 2.5 Comparison of the flood probability before and after integrating the NDWI.	21
Figure 2.6 Final RFP and subset comparisons with the EFP.....	23
Figure 2.7 Tweet examples and visual comparison of EFP and RFP with high-res Google Earth images acquired on Oct 7.	24
Figure 2.8 The RFP compared with USGS HWMs and USGS Inundation map.....	25
Figure 2.9 The EFP in the whole research area and in area within USGS inundation area.....	26
Figure 3.1 Conceptual workflow.	36
Figure 3.2 Transfer learned model from Inception-v3.....	37
Figure 3.3 Word embedded CNN architecture.	40
Figure 3.4 Fusion of visual and textual information.....	43
Figure 3.5 Research area for two flooding cases with their geotagged tweets; (a) Continental U.S; (b) South Carolina flood in 2015 with 934,896 geotagged tweets from Oct 2 nd to Oct 9 th ; (c) Houston flood in 2017 with 501,516 geotagged tweets from Aug 25 th to Sep 1 st	44
Figure 3.6 Model performance of the visual CNN.	49

Figure 3.7 (a) Textual CNN ROC curve for all five folds; (b) Training accuracy curve for fold one; (c) Training loss curve for fold one.	53
Figure 3.8 ROC curves of the six algorithms using visual-textual fused vector (Z_{fused}) and using textual vector ($Z_{textual}$) alone.	56
Figure 3.9 Eight examples of the classification results.....	58
Figure 4.1 Historical storm tracks from the North Atlantic Basin (in red) and from the Eastern Pacific Basin (in green)	69
Figure 4.2 (a) Historical storm tracks from the North Atlantic Basin; (b) Normalized storm track density weighted by wind speed; (c) Hurricane-prone zones.....	77
Figure 4.3 DMSP/OLS NTL intercalibration in L.A. metropolitan and City of San Diego; (b1) Correlation between F162006 and reference year F162007; (b2) Correlation between F101992 and reference year F162007; (b3) Correlation between F152003 and reference year F162007	78
Figure 4.4 (a) $NDVI^{MVC}$ series from AVHRR in the overlaying years; (b) $NDVI^{MVC}$ series from MODIS in the overlaying years; (c) linear regression between AVHRR and MODIS using stratified sampling; (d) comparison of histograms between MODIS and AVHRR.	80
Figure 4.5 The VANUI distribution in the study area in 1992 (a); The subfigures demonstrate the VANUI variations in 1992, 2002, and 2013 in five selected urban cities: Philadelphia (b), Charlotte (c), Atlanta (d), Houston (e), and Orlando (f)	82
Figure 4.6 Yearly statistics of percent area with VANUI larger than 0 in Zone 1(a), Zone 2 (b), Zone 3 (c) and Zone 4 (d).....	84
Figure 4.7 Maps of the 22-year Mann-Kendall trend and Theil-Sen slope in the study area	87
Figure 5.1 FEMA 100-year floodplain availability in CONUS at county level (FEMA floodplain retrieved on April 1 st , 2019).....	99
Figure 5.2 General workflow of estimating the population exposed to 100-year floods in the CONUS using national building footprints.	102
Figure 5.3 Age composition exposed to 100-year floodplains in the CONUS.....	108
Figure 5.4 Race composition exposed to 100-year floodplains in the CONUS	110

Figure 5.5 Composition of ethnicity, tenure, employment, and poverty in FEMA (F/P + Coastal) with the composition from the entire U.S.	112
Figure 5.6 Population distributed in the JRC (a), GAR (b), and FEMA (F/P) (c) floodplains.....	114
Figure 5.7 Total population distributed in RFCON and FEMA (F/P + Coastal).....	114
Figure 5.8 County-level differences between exposed population from GAR and FEMA (F/P) in proportion to the county population (a2) associated with county count histogram (a1); County-level G_i^* Z score distribution (b2) associated with county count histogram (b1).	118
Figure 5.9 County-level differences between exposed population from JRC and FEMA (F/P) in proportion to the county population (a2) associated with county count histogram (a1); County-level G_i^* Z score distribution (b2) associated with county count histogram (b1).	119
Figure 5.10 County-level differences between exposed population from RFCON and FEMA (F/P + Coastal) in proportion to the county population (a2) associated with county count histogram (a1); County-level G_i^* Z score distribution (b2) associated with county count histogram (b1)	120
Figure 5.11 Comparison between flood exposure analysis based on centroids of geographic units (block groups) (a) and based on building footprints (b).	122

CHAPTER 1

INTRODUCTION

Flood is one of the most powerful forces on Earth, posing devastating threats to all population in the world. Despite the advances in flood-related studies and the implementation of national hazard reduction policies, the flood-induced damages follow an increasing trend (Pielke and Downton, 2000). Globally, one-third of annual natural disasters and economic losses and more than half of all victims are flood-induced (Douben, 2006). In the United States, extreme rainfalls and floods have accounted for an annual loss of 82 lives and economic damage averaging \$7.96 billion each year in 1984-2013, according to NOAA's National Weather Service (NWS, 2018). In 2005 alone, direct flood damage claimed 43 lives and a total of \$55.33 billion, approximately 8 times of the thirty-year average. As the severity and frequency of flood events have noticeably increased, there is a growing need of a rapid flood mapping approach for better understanding of flood exposure via the means of Big Data techniques to reduce flood-related fatalities and economic losses.

Among all the flood-related mitigation activities, flood mapping is critical for flood mitigation (Tran et al., 2008), emergency response (Levy et al., 2007), and post-event damage assessment (van der Sande et al., 2003). Flood mapping is able to provide situational awareness for the public and quickly draws attention to certain areas where immediate actions are needed. As it is often difficult and dangerous to conduct simultaneous field surveys during the disaster event, the non-contact techniques have often

been used to collect information and contribute to flood mapping. Big Earth Data, i.e., satellite observations, have long been used to monitor flood coverage and its dynamic development. Although remote sensing imagery is able to provide a synoptic view over a large area, the limited temporal resolution due to a satellite's long revisit cycle and heavy cloud cover (especially for optical remote sensing) during a flood event have hindered its application in real-time flooding analysis. Social sensing has witnessed increasing attention due to the popularity of crowdsourcing approaches. Volunteered geographical information (VGI), a crowdsourcing approach, provides an alternative approach to reporting a flood in real-time (Triglav-Čekada and Radovan, 2013; McDougall and Temple-Watts, 2012). With increasing numbers of sound crowdsourcing platforms being built, there is an up-surging interest of utilizing VGI to aid the rapid flood mapping process and to gain a better flooding situation awareness (Li et al., 2018; Horita et al., 2015; Schnebele et al., 2014). However, the challenge of extracting useful information from a massive VGI pool in an automated manner still remains. Recently, the rapid development of deep learning (DL) makes the automation of rapid VGI classification possible by showing great potential in classifying both pictures (Krizhevsky et al., 2012) and texts (Kim, 2014). Those state-of-the-art machine learning algorithms have significantly boosted the efficiency in terms of handling user-generated big data.

A better understanding of flood exposure is also essential for authorities to reduce flood-related losses. Hurricane induced floods have posed significant threats to people residing in the U.S Atlantic and Gulf Coasts (Landsea et al., 2010). In these hurricane-prone areas, a better understanding of the temporal and spatial dynamics of human settlement is needed for improved damage assessment and sustainable urban planning.

Fortunately, satellite-derived nighttime light (NTL) data provides a unique and direct observation of human settlement via night lights (Ceola et al., 2014; Ceola et al., 2015) and can reflect the human settlement dynamics in the coastal regions for a long time. For the flood exposure nationwide, the 100-year floodplain (1% of annual exceedance probability), produced by the Federal Emergency Management Agency (FEMA), has been commonly used as the longstanding marker for analyzing flood exposure (Blessing et al., 2017). Numerous estimations have been conducted based on the boundary of FEMA 100-year floodplain to estimate the exposure of floods and how this exposure is distributed nationwide (Crowell et al., 2010; Qiang et al., 2017; Yager et al., 2018). Those estimations, however, usually failed to capture the great heterogeneity of population distribution and failed to compare the results from multiple floodplain products. Thus, a comparative assessment of the flood exposure considering the heterogeneous distribution of the population is in great need.

This dissertation is organized into six chapters. The objectives of the remaining chapters are described as follows:

- **Chapter 2:** designing an advanced data fusion flood model that integrates remote sensing imagery, water gauges, and social media for near real-time flood mapping.
- **Chapter 3:** automating the retrieval of flood relevant social media posts using state-of-the-art deep learning algorithms considering both textual and visual information.
- **Chapter 4:** exploring the hurricane-induced disaster exposure in the Atlantic/Gulf Coasts using historical storm tracks and nighttime remote sensing imagery.

- **Chapter 5:** benchmarking the population exposure of flood risks in the CONUS via national building footprint dataset and comparing its assessment from multiple floodplain products.
- **Chapter 6:** summarizing previous chapters and presenting concluding remarks for this dissertation.

CHAPTER 2

REMOTE SENSING-SOCIAL SENSING INTEGRATED FLOOD MODELING¹

2.1 INTRODUCTION

Intensive studies on flood mapping have been conducted, which could be generally categorized into three major groups based on the timing of data acquisition and analysis: 1) real-time (RT) flood mapping, i.e., utilizing real-time data from water gauge sensors, timely official flooding reports or crowdsourcing; 2) near real-time (NRT) mapping, i.e., utilizing data shortly after the flooding event, usually with a lag of several days; and 3) post-event flood mapping, i.e., utilizing data long after the flooding event, mostly for long-term damage assessment after a severe flood.

The RT flood mapping has witnessed increasing attention due to the ubiquity of stream gauge implementation and the popularity of crowdsourcing approaches. Real-time mapping techniques have the ability to produce a relatively coarse but timely flood assessment that is crucial for rapid flood mitigation and response. Water height readings collected from the installed stream gauges, commonly applied along with the local Digital

¹ Huang, X., Wang, C., & Li, Z. (2018b). Reconstructing flood inundation probability by enhancing near real-time imagery with real-time gauges and tweets. *IEEE Transactions on Geoscience and Remote Sensing*, 56(8), 4691-4701. Reprinted with permission from the publisher.

Elevation Model (DEM), is one of the most commonly used real-time data for rapid flood mapping (Sanders, 2007). The U. S. Geological Survey (USGS), for example, provides water height information at each stream gauge at 15-min intervals. However, limitations do exist because 1) those gauges are dispersedly distributed, resulting in insufficient information acquisition and when 2) water levels rise beyond the measuring limits, resulting in no water height records (Li et al., 2018). Volunteered geographical information (VGI), a type of crowdsourcing approaches, provides an alternative approach to reporting a flood at the exact time of its occurrence (Triglav-Čekada and Radovan, 2013; McDougall and Temple-Watts, 2012). Defined by Goodchild (2007), VGI describes the concept of citizens as sensors, allowing rich voluntary information to be provided in the form of text, images, and videos to aid geospatial and temporal analysis. With increasingly sound crowdsourcing platforms becoming available, there is an up-surgng interest of utilizing VGI to aid the rapid flood mapping process and to gain a better flooding situation awareness (Li et al., 2018; Horita et al., 2015; Echnebele et al., 2014; Fohringer et al., 2015; Wang et al., 2018). However, compared to authoritative information, the largely untrained VGI providers and its built-in assertive characteristics strongly restrict its functional utility (Jackson et al., 2013; Feick and Roch, 2013; Haworth and Bruce, 2015). Bearing this limitation, VGI is often expected to take a supplemental role and to act as an augmentative source for traditional datasets.

The NRT flood mapping deals with data within a few days of delay, an invaluable data source for disaster monitoring and relief efforts (Smith, 1997). As a major component of NRT data source, remotely sensed (RS) imagery can provide significant mapping capabilities that have been widely used to monitor flooding extent and to assess its damages

(Wang et al., 2002; Brivio et al., 2002; Joyce et al., 2009). Compared to the real-time data, RS images render a synoptic view in a large geographic area, significantly contributes to a holistic understanding of flooding situations. Among all flood-related indicators derived from RS images, the Normalized Difference Water Index (NDWI) has been extensively used as an indicator of land surface wetness (Mallinis et al., 2011). A broad range of applications leveraging NDWI for flooding related purposes have been conducted, including water coverage delineating (McFeeters, 1996), flood hazard mapping (Jain et al., 2006) and flood prone area identification (Jain et al., 2005). The NDWI provides rich wetness information that is more valuable in flooding analysis than traditional water delineation approaches. However, the inherent restrictions within the near real-time RS imagery somehow hamper its utility. For example, the coarse temporal resolution (i.e., long revisit cycle) and extreme weather conditions (i.e., cloud cover during a storm) heavily prevent RS sensors from acquiring timely images (Fazeli et al., 2015). For images acquired after a flood event, the information in the temporal gap between flooding peaks and image acquisitions is lost.

These inherent limitations from both RT and NRT sources can be reciprocally compensated. The spatially isolated RT data can be used to enhance the delayed image observations, thus compensating for the information loss in both spatial and temporal dimensions. Data obtained from RS sensors, though in a delayed manner, provides a spatially continuous view that is superior to the isolated stream gauge records and the uncertain posts from social media. The combined information leads to the reconstruction of flood extent and flood risks during an event. Guided by this idea, attempts have been made to integrate the NRT images with RT sources. Wang et al. (2002) found that the

integration of Landsat TM images and river gauge readings overcame the flooding underestimation issue due to the lack of penetration of RS sensors in vegetation canopies. Schnebele and Cervone (2013) improved the RS flood assessment by combining satellite imagery with high temporal-resolution ground data. More fusion of NRT and RT data can be found in a number of flood studies (Schnebele et al., 2014; Cervone et al., 2015; Musser et al., 2016). As part of this dissertation research, Huang et al. (2018) found that surface wetness derived from NRT remote sensing images serves as a great weighting factor for RT flood-related tweets.

This chapter designs a method that reconstructs flood inundation probability by fusing the real-time stream gauge data and social media (tweets) to enhance the near real-time NDWI layer derived from RS imagery. The 2015 SC Flood event in Columbia, SC is explored here as a case study. The flood inundation probability is reconstructed by offsetting the information loss in the time gap while preserving the distributions of land surface wetness. A global enhancement module is first developed by combining the NDWI surface and stream gauge data to gain a general flood inundation probability distribution. Then a novel morphological operator-based local enhancement module is presented by considering the verified tweets as a local source of real-time flooding. The model output is validated via the USGS survey points and USGS inundation map released four months after the event (Musser et al., 2016). The term “flooding probability” (FP) refers to flood inundation probability, a probability of a certain area being inundated during a flood event.

2.2 RESEARCH AREA AND DATASETS

2.2.1 Hurricane Joaquin and the 2015 SC Flood in Columbia, SC

Hurricane Joaquin is the strongest Atlantic hurricane of non-tropical origin in the satellite era (Berg, 2016). Started as a tropical storm on September 29, it continued to strengthen and evolve into a hurricane on September 30. Figure 2.1a shows the path of Hurricane Joaquin released by the National Hurricane Center (NHC), National Oceanic and Atmospheric Administration (NOAA) (Figure 2.1a).

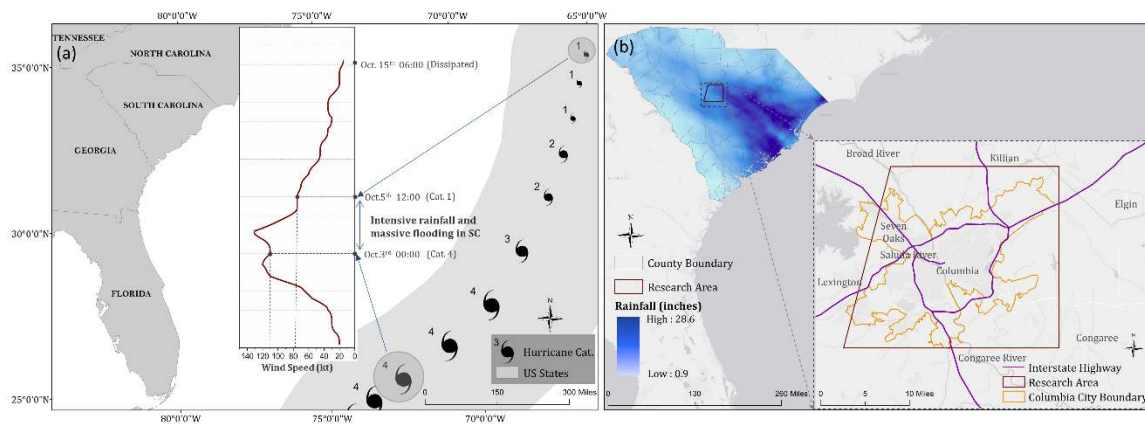


Figure 2.1 (a) Hurricane Joaquin; (b) Rainfall status in SC and the research area of this chapter.

Hurricane Joaquin contributed to record rainfall in SC from October 1 to 6 with some areas received more than 20 inches of rainfall. The widespread record-breaking rainfall caused catastrophic floods from the central part of the SC to the coast, resulting in 19 fatalities and approximately \$1.5 billion damage losses in the state (Feaster et al., 2015). Around 410 roads and bridges were closed, at least 17 dams were damaged, and more than 50,000 residents experienced a massive power failure (Feaster et al., 2015; Murphy, 2015).

The capital city in SC, Columbia, also experienced widespread and devastating floods led by the storm. This densely populated area covers Richland County and Lexington County in the central part of SC (Fig 2.1b). Congaree River, joined by Broad

River and Saluda River in the north, is the major flowing waterbody across its metropolitan area. During this 5-day lasting flood, Columbia was significantly impacted in all aspects. In this chapter, The City of Columbia and its nearby surroundings were chosen as the research area.

2.2.2 Datasets and preprocessing

The datasets used in this study can be roughly broken into four categories based on the data acquisition period, which include real-time data, near real-time data, post-event data, and accessory data.

Real-time dataset

Water height readings of five stream gauges located in the research area were downloaded. The five gauges are numbered u02162093, u02169000, u02169500, u02169506 and u02169570. The USGS provides water height data for those gauges at a 15-min interval. Their spatial locations are marked in Figure 2.2a.

To evaluate the rainfall effects, the highest existing water height reading at each gauge was extracted. The reference water height was assumed the water height reading at 9:00 AM, October 1 (a stable stage before the flooding event) in this study (Table 2.1). It should be noted that the maximum water height readings in Table 2.1 do not necessarily represent the maximum water level in streams. Sensors in some gauges failed to record water height due to a variety of reasons, leading to the missing records for a certain period of time (as shown in Figure 2.2b). Given the incomplete height readings, the maximum water height readings in Table 1 denote the highest readings available for each gauge. Both the maximum and reference water height readings are later translated to the elevation based on their base height (a datum conversion process is involved).

Table 2.1 Detailed statistics of five gauges.

Gauge Number	Gauge base height (<i>ft</i>)	Datum shift (<i>ft</i>)	Maximum water height reading (<i>ft</i>)	Maximum water height Reached time	Reference water height reading (<i>ft</i>) ^a
# 02162093	199.10	-0.794	18.93	Oct 4 th 5:07:00 AM	0.56
# 02169000	149.46	-0.787	8.33	Oct 3 rd 7:45:00 AM	2.91
# 02169500	113.02	-0.787	31.83	Oct 4 th 5:52:00 PM	3.91
# 02169506	165.55	-0.781	12.40	Oct 4 th 2:22:00 AM	0.98
# 02169570	137.38	-0.778	8.34	Oct 6 th 0:00:00 AM	3.17

Note. The datum for gauge base height is NGVD 29 while the datum for DEM used in this study is NAVD 88. A conversion tool in VERTCON (https://beta.ngs.noaa.gov/cgi-bin/VERTCON/vert_con.prl) is used to convert them to a uniform datum (NAVD 88).

^a Reference water height readings from all five gauges were obtained at Oct 1st 9:00 AM

The tweets pool used in this study has been generated using the Twitter Stream API and REST API in the previous study (Li et al., 2018). All geotagged tweets within the research area between October 3 and 6 were downloaded, then manually checked to make sure that their information was coordinates-relevant and flood-relevant. After the spatial restraint and keywords restraint, a total of 49 flood-related tweets with content covering text, photo, or both were selected within the research area (Figure 2.2a). Their contents are flood-related and matched well with their intrinsic longitude and latitude. Tweets labeled “law enforcement” are official flash flood warnings issued by local authorities.

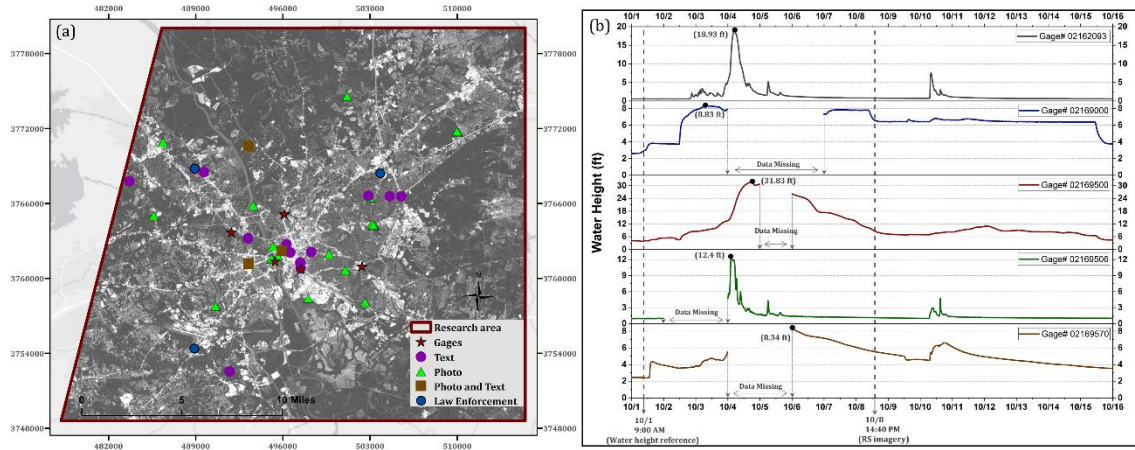


Figure 2.2 (a) The ALI image (panchromatic), locations of the verified tweets, and stream gages; (b) Water height readings at the five stream gages.

Near real-time satellite image

The near real-time satellite image used in this study was acquired from the EO-1 Advanced Land Imager (ALI) on Oct 8th 14:40 PM, the earliest cloud-free satellite multispectral image available in this flood event to my best knowledge. The EO-1 renders 30-m resolution in multispectral bands and 10-m in a panchromatic band covering the research area (Fig 2a). Given the slight haze existence and atmosphere interference, an atmospheric correction together with haze removal function was applied in the ATCOR2 module of ERDAS/IMAGINE. The corrected surface reflectance image was converted to a NDWI image to represent land surface wetness, using the formula proposed by Gao (1996):

$$NDWI = \frac{\rho_{green} - \rho_{SWIR}}{\rho_{green} + \rho_{SWIR}} \quad (2.1)$$

where ρ_{green} and ρ_{SWIR} represent the green and short-wave infrared band, respectively. Google earth provides several high-res scenes on Oct 7th, two days after the flooding peak. However, due to their small coverage, they were used for visual comparison and verification purposes.

Post-event dataset

After the 2015 SC Flood, the USGS surveyors conducted field surveys to collect water height marks to aid in documenting the high-water events. The USGS survey points for the 2015 flood event in SC were downloaded through USGS Short-Term Network (STN) Portal (<https://stn.wim.usgs.gov/STNDataPortal/#>). The dataset contains a total of 574 water height marks (HWM) in SC, and 337 within the research area. To ensure the data quality, we only selected HWMs with quality remarks “Good” and “Excellent”. After the spatial and quality restriction, a total of 277 good-quality HWMs were extracted within the research area.

The official inundation map was acquired from USGS Flood Inundation Mapping (FIM) Program (https://water.usgs.gov/osw/flood_inundation), an authoritative flood inundation source. It should be noted that USGS only surveyed the area within the flood zone. Although not covering the whole research area, the valuable binary flood extent and field surveyed HWMs provided by USGS are the only official post-event data available at the time of writing.

Accessory dataset

The DEM elevation data at 3-meter resolution was obtained from the South Carolina Department Natural Resources (<http://www.dnr.sc.gov/GIS/lidar.html>). The high-res Google Earth images acquired soon after the flood was later available in the research area. They were visually compared with the modeled results for comparative analysis. Other spatial datasets (Shapefiles), including city, county, and state boundaries, were retrieved from local authorities.

2.3 METHODS

In this chapter, the proposed flood reconstruction model consists of three modules: 1) generating an initial flooding probability (IFP) merely based on water height readings at five gauges and DEM (Water Height Module); 2) generating an enhanced flooding probability (EFP) by globally enhancing the NDWI surface derived from the RS image with the IFP (Global Enhancement Module) via kernel smoothing, standardization and aggregation functions; and 3) generating reconstructed flooding probability (RFP) by locally enhancing the EFP with the verified tweet points via a morphological operation (Local Enhancement Module). A detailed flowchart is outlined in Figure 2.3.

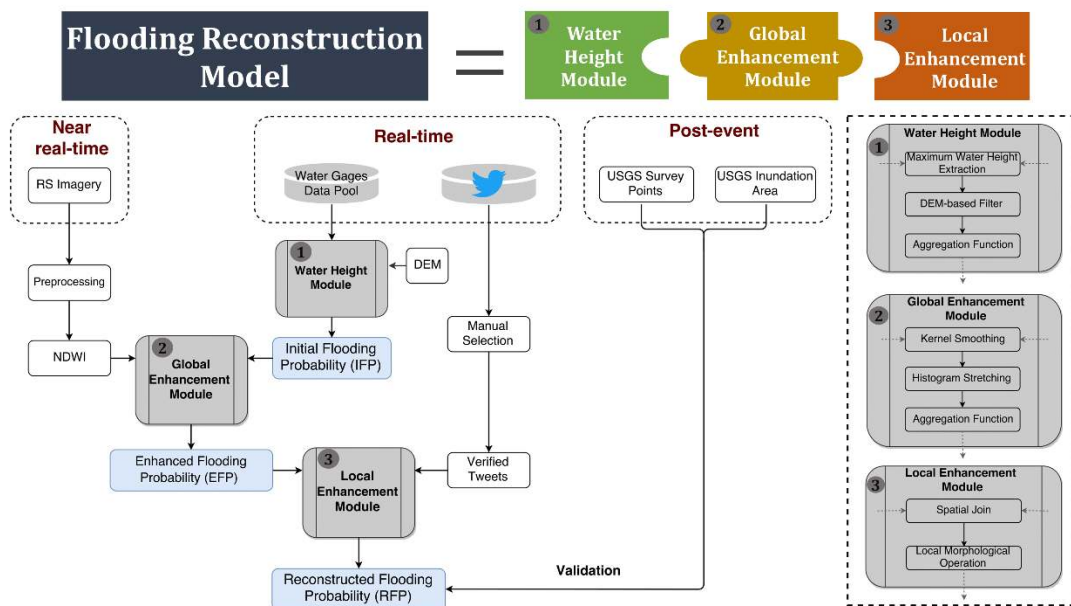


Figure 2.3 Methodology overview.

2.3.1 Water height module

This module integrates the DEM and water height points to generate an Initial Flooding Probability (IFP) layer by building an initial flood water surface. The maximum readings of water height at stream gauges represented this point's real-time water height during the

flood event. Data from all five gauges were used in the model to compensate for the uncertainty from local topological unevenness.

With the readings at a given gauge, the elevation at each pixel of the research area is compared against the reference water height and maximum water height (listed in Table 2.1) and is classified as one of the three categories: water body, flooded areas, and non-flooded areas. If the elevation of a pixel below the reference water height, it is more likely natural water body. If its evaluation is above the maximum height, it is not likely to be flooded (non-flooded). If the elevation is in between, we assume that it is flooded. Different elevation thresholds are applied when compared with readings at different gauges (Table 2.2). Different weights are given to the three categories to approximate their proneness to flooding. Natural water bodies are assigned a weight of 2. The Non-flooded areas have a weight of 0 because areas higher than the maximum water height are not likely to be flooded. Areas in between are assigned a weight of 1.

Table 2.2 The three DEM-reclassified categories in the research area based on the reference water height and maximum water height at each gauge.

Gauge Number	DEM range (<i>ft</i>)		
	Water Body	Flooded areas	Non-flooded areas
# 02162093	<198.866	[198.866, 217.236)	≥217.236
# 02169000	<151.583	[151.583, 157.003)	≥ 157.003
# 02169500	<116.143	[116.143, 144.063)	≥ 144.063
# 02169506	<165.749	[165.749, 177.169)	≥ 177.169
# 02169570	<139.772	[139.772, 144.942)	≥ 144.942

Five weight layers (W_Layer) are extracted since we have five gauges in the research area. An aggregation function was applied to extract the Initial Flooding Probability (IFP) layer:

$$IFP = \sum_{i=1}^n W_Layer_i \quad (2.2)$$

where $n=5$, denoting five separate layers from five gauges within the research area. The resulted IFP has a weight range of [0,10].

2.3.2 Global enhancement module

This module incorporates both land surface wetness and topographic characteristics by integrating the NDWI surface with the IFP from the water height module. The integration of wetness analysis and DEM-based analysis aids in 1) compensating the information lost between the NRT RS image and RT water height readings; and 2) providing additional flooding awareness for areas with high elevation where the DEM-based IFP fails to cover. Even the NDWI layer represents the wetness conditions a few days after the flood event, areas with high wetness indicates that they are prone to flooding during the event. Integrating the spatially dynamic distributions of wetness into the IFP, a comprehensive situational awareness of the flooding probabilities is achieved.

The Global Enhancement Module begins with a quartic kernel smoothing function, which places a moving 2-D kernel over the data layer to achieve an estimation of the density at the kernel center. In this module, a kernel smoothing function is applied to both NDWI and IFP layers. The kernel smoothed IFP layer, namely $IFPs$, is mathematically defined as:

$$IFPs_{(x,y)} = \frac{1}{nh^2} \sum_{i=0}^n K\left(\frac{IFP_x - x_i}{h}\right) K\left(\frac{IFP_y - y_i}{h}\right) \quad (2.3)$$

where h and n denote the bandwidth and sample size of the kernel, respectively. The $IFPs_{(x,y)}$ represents the density estimation at location (x, y) . The bandwidth h of kernel K is initially set to 1000 meters for calculational convenience. The kernel function K used in this chapter is the quartic kernel, which is calculated as:

$$K(u) = \frac{15}{16}(1 - u^2)^2 \quad (2.4)$$

where variable u has to meet a cut-off requirement: $|u| \leq 1$.

Similarly, the ALI-derived NDWI is smoothed using the same kernel function and parameter settings. The result is named $NDWI_s$. Both $NDWI_s$ and IFP_s is then normalized to the $[0, 1]$ using a max-min normalization, namely IFS_n and $NDWI_n$, respectively. The normalization process makes these layers mathematically comparable, greatly facilitating the calculation and interpretation.

After the normalization, we notice that the IFS_n is distributed consistently and distinguishably in its value range. However, the $NDWI_n$ values are mostly clustered in its middle range (around 0.5). To better spread out these most frequent values, a modified logistic stretch function is applied to $NDWI_n$. The contrast enhancement function is defined as follows:

$$S_NDWI_n = \frac{L}{1 + e^{-k(NDWI_n + a)}} \quad (2.5)$$

where S_NDWI_n represents $NDWI_n$ after the logistic stretch, k is the coefficient that controls the steepness of the curve, a is the x-value of midpoint and L measures the maximum value of the curve. The constants L , a and k are set as 1, 0.5 and 10, respectively.

Finally, an Enhanced Flooding Probability (EFP) is produced by aggregating the IFS_n and S_NDWI_n as bellow:

$$EFP = IFS_n + S_NDWI_n \quad (2.6)$$

2.3.3 Local enhancement module

The EFP layer could be locally enhanced around the verified flood-related tweets locations, which are the local areas that were actually flooded during the 2015 SC Flood event. The

local enhancement around these locations involves a morphological dilation process that significantly boosts the flood probability of the local areas around a flood tweet point. According to Tobler's law, areas closer to a verified tweet point are more likely to be flooded. Therefore, pixels surrounding the tweet point could be locally enhanced for their flooding probability, and those closer to the tweet point receive stronger enhancement.

It is reasonable to assume that this local enhancement follows a morphological dilation pattern centered at this tweet point. Assigning a domain of areas with a search radius centered at a tweet point, at a pixel (x, y) , the dilation process is mathematically defined as:

$$g(x, y) = (EFP \oplus e)(x, y) = \max\{EFP(x - a, y - b) | (x - a, y - b) \in D_s; (a, b) \in D_e\} \quad (2.7)$$

where D_s denotes the domain of areas within a search radius from the tweet point. D_e denotes the domain of a structuring element e . Term g represent the dilated output at (x, y) .

To take the distance-decay effect into consideration, a distance-related coefficient c is introduced to the function:

$$RFP(x, y) = \frac{g(x, y) - EFP(x, y)}{c} + EFP(x, y) \quad (2.8)$$

where $RFP(x, y)$ denotes the final result of the modified dilation process which takes distance decaying into account at location (x, y) . The coefficient c is defined as $c = \frac{r}{r-d}$.

Where r denotes the radius of the search area and d denotes the distance from (x, y) to the tweet point.

Within the search area of a tweet, the dilation process selects the maximal value and adjusts the enhancement strength based on the distance of a pixel towards the tweet

point. Initially, a square-shaped structuring element with a length of 10 pixels (300 meters) was chosen and a search radius was set to be 1000 meters.

2.4 RESULTS AND DISCUSSION

2.4.1 The Initial Flooding Probability (IFP)

The integration of DEM and water height readings at five river gauges generated the IFP for the entire research area. The individual weight layers based on different gauges could vary due to the uncertainty induced by local DEM variance. Each layer provides its own estimation based on a single gauge reading, rendering a local flooding probability prediction. Fig 4a1-4a5 demonstrate five individual flood extent weight layer extracted from their river gauges. The flood extents they measured are different from each other due to the unevenness of local terrain. Exceptionally, the weight layer based on Gauge 02169500 varies significantly from other gauges (Figure 2.4 (a4)). The integration of all gauges greatly reduces the uncertainties induced by local DEM variations and provides an overall representation of flooding probability in the research area (Figure 2.4 (b1)). DEM is an important topological characteristic of flooding morphology. By taking it into consideration, the IFP serves as a valuable initial layer for the integration of other data sources.

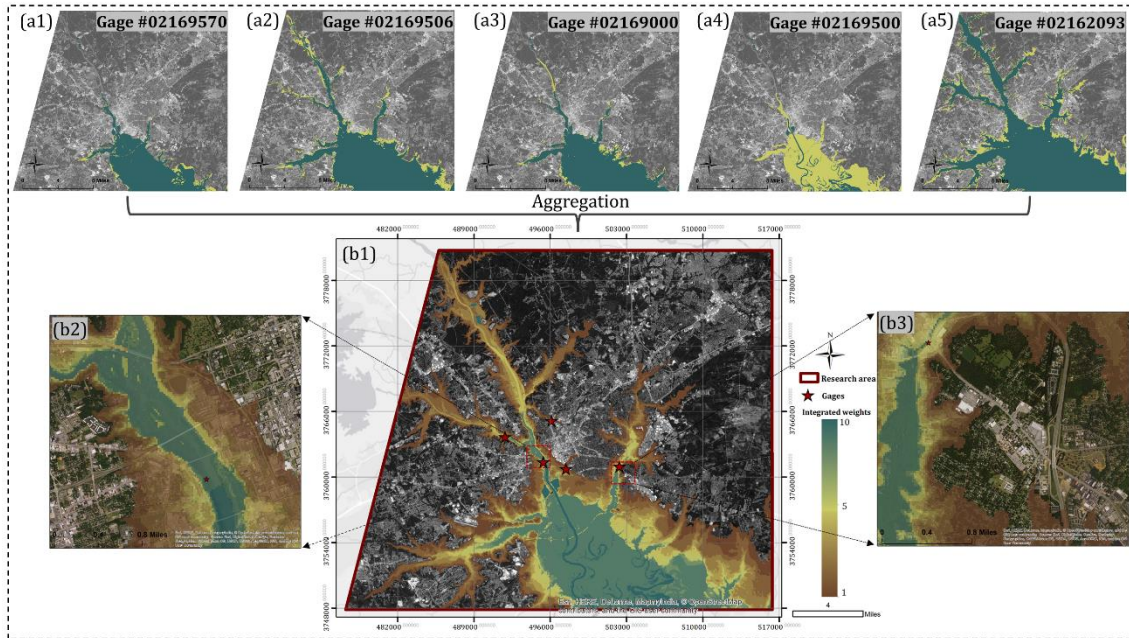


Figure 2.4 The IFP derived from DEM and gauges. The background is the black-and-white display of the ALI image.

The aggregated IFP layer in Figure 2.4 (b1) has integer values ranging from 0 to 10, indicating different levels of flood proneness. The IFP value with 0 represents the areas at elevations higher than the maximum recorded water height of all gauges, therefore, is not possibly flooded. IFP value with a maximum 10 represents areas lower than the maximum water height of all gauges and, therefore, has the highest potential of being flooded. Areas with 0 IFP are left transparent to show the background image in the figure. Fig 4b1 reveals a massive flood occurrence in the south of the research area (IFP value = 10), and high flooding probabilities following the Congaree River (Figure 2.4 (b2)) and Gills Creek (Figure 2.4 (b3)) in downtown Columbia.

2.4.2 The Globally Enhanced Flooding Probability (EFP)

EFP takes wetness into consideration by Enhancing DEM based measurement (IFP_n) with soil wetness derived from remote sensing imagery (S_NDWI_n). Figure 2.5 compares the

distributions of the flooding probabilities before and after the NDWI-implemented global enhancement.

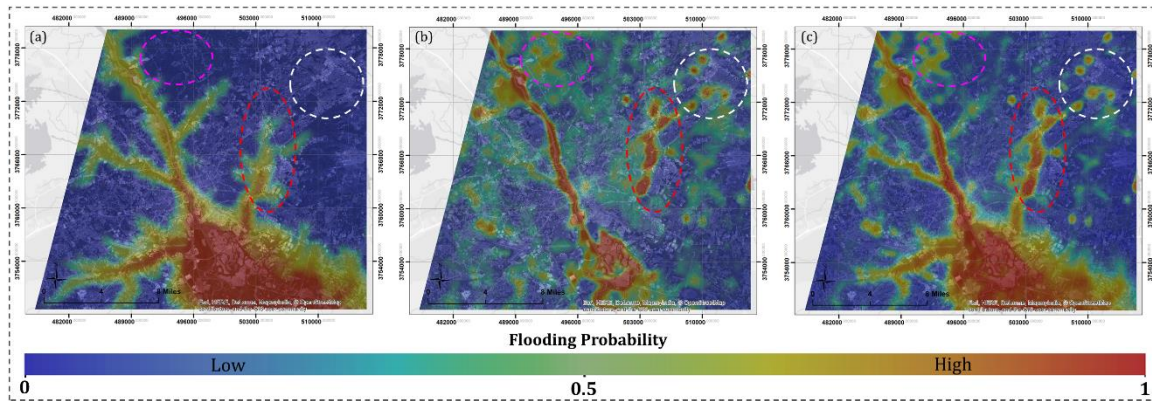


Figure 2.5 Comparison of the flood probability before and after integrating the NDWI.

In Figure 2.5a, the IFP_n successfully identifies the low-elevation flooded areas along the major stream channels. The extensive area of high flooding probability in the south of the research area was actually flooded due to its low elevation during the event. The flooded areas in the south end of Figure 2.5a are not well identified in Figure 2.5b due primarily to the time lag of image acquisition. The image was taken three days after the flooding peak, and floods in local areas have retreated. Therefore, the IFP_n has a distinctive real-time advantage over S_NDWI_n .

On the other hand, with the spatially continuous NDWI, Fig 5b reveals the hot spots of high wetness in high elevation zones (highlighted by circles). Areas in high elevations are also likely to be flood-prone due to its local topographic unevenness and land use types. In Figure 2.5b, these local areas are fairly identified by their high land surface wetness. Therefore, the S_NDWI_n renders holistic wetness information, largely contributing to identifying areas at higher elevations where IFP_n fails to cover.

As integration of IFP_n and S_NDWI_n , the EFP obviously provides a better estimation by taking advantage of both aspects (Figure 2.5c). In a spatial perspective, it not

only keeps high flooding probability in lower elevations and alongside river channels demonstrated by IFP_n , but also highlights the potentially flooded regions in higher elevations as suggested by the high wetness in S_NDWI_n . In a temporal perspective, EFP compensates the time lag from remote sensing imagery by incorporating real-time river gauge readings. Figure 2.5 demonstrates that, by considering DEM/gauges and wetness together, a more comprehensive, global flooding probability estimation is achieved.

2.4.3 The Reconstructed Flooding Probability (RFP)

RFP is a result of a local enhancement from EFP via a morphological dilation process. It utilizes the spatial and temporal advantage provided by verified flood-related tweets. (Figure 2.6). The in-situ information provided by verified flood-related tweets aids in higher accuracy of local flooding probability adjustment. Their inherent real-time characteristic reconstructs the flood surface by enhancing the flooding probabilities of their surrounding pixels and expanding the projected inundation. From EFP to RFP , the local enhancement module considers tweets as input and significantly adjusts the EFP layer using additional verified information provided by Twitter users. Several comparisons of EFP and RFP are shown in the subsets marked in Figure 2.6. Subset b1, c1, and d1 represent the flooding probabilities in EFP . Subset b2, c2, and d2 represent the flooding probabilities after the local enhancement in RFP . Significant modifications can be observed as flooding probabilities around the tweets (black dots) in subset b2, c2, and d2 are much higher than those in subset b1, c1 and d1 respectively. Those modifications indicate that supplemental real-time data sources like tweets can greatly aid in identifying locations ignored in EFP .

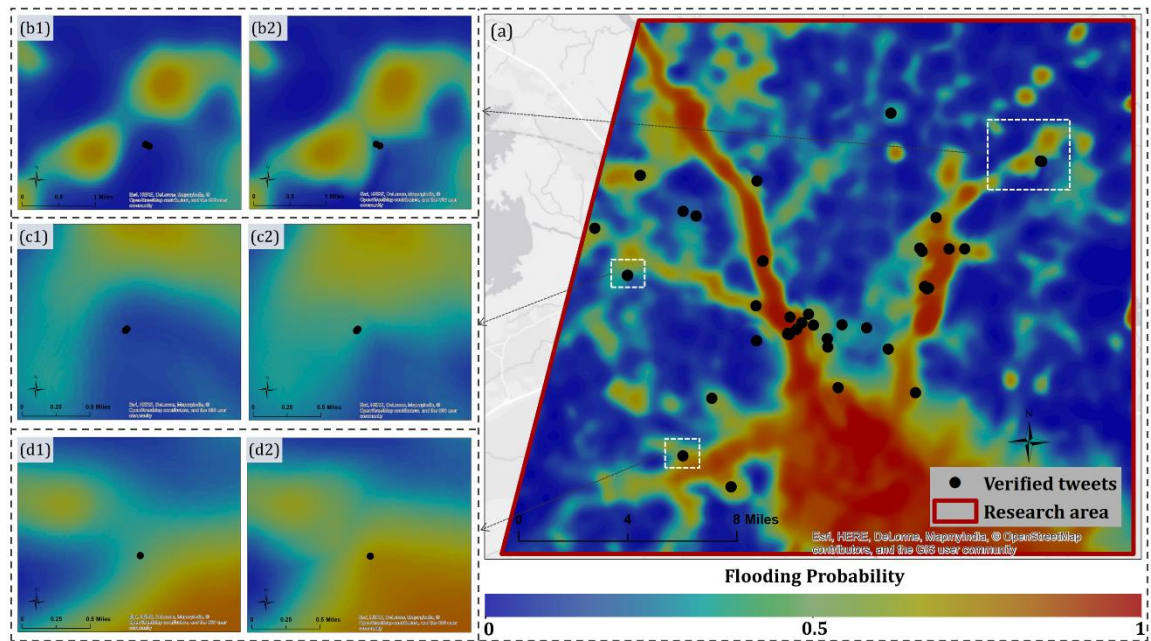


Figure 2.6 Final RFP and subset comparisons with the EFP.

In Figure 2.7, a more detailed comparison before and after the tweet-implemented flood probability (EFP vs. RFP) is performed by visually checking with the high-res Google Earth images (a1 and b1 in Figure 2.7) acquired on Oct. 7th, two days after the flooding. Figure 2.7 (a2) and (b2) are the EFP in the imaged subsets, and Figure 2.7 (a3) and (b3) are the locally enhanced RFP from (a2) and (b2), respectively, using those tweets (black dots) in each subset.

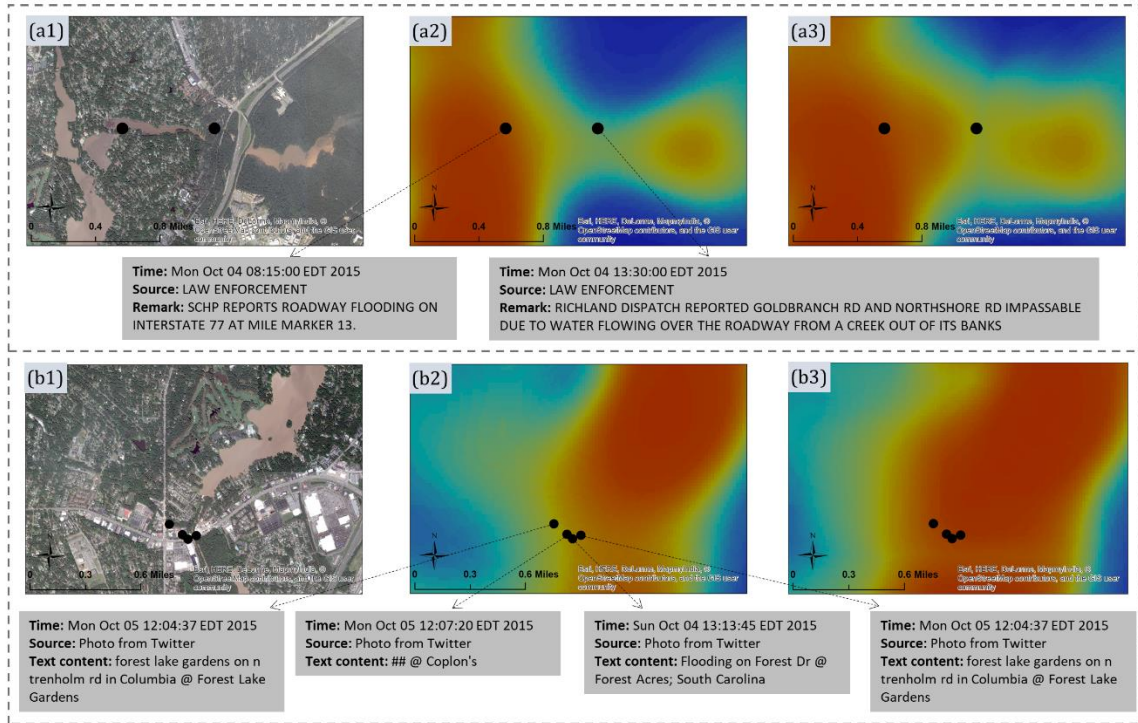


Figure 2.7 Tweet examples and visual comparison of EFP and RFP with high-res Google Earth images acquired on Oct 7.

It is obvious that EFP (Figure 7 (a2) and Fig 2.7 (b2)) can actually reveal the local floods as shown in the corresponding Google Earth images (Figure 2.7 (a1) and Figure 2.7 (b1)). However, some flooded areas indicated by the verified tweets are not well spotted either on Google Earth images or the EFP, for instance, the four tweets marked in b1. This is partly due to the time discrepancy between the tweets and images as those high-res images were taken on Oct 7th while the flood reached its peak around Oct 5th. Compared to the EFP, the RFP (a3 and b3) boosts the flooding probabilities surrounding a certain tweet, resulting in a reasonable probability adjustment via the crowdsourcing data. Examples in Figure 7 illustrate that even a small amount of real-time supplemental VGI from social media can significantly adjust the flooding probability at the local scale, thus improving the reconstruction of the flood probability distributions during a flood event.

2.4.4 Comparison with the USGS HWMs and inundation map

The RFP was compared with two major post-event flooding data sources, the USGS surveyed HWMs, and the officially released inundation map (Figure 2.8). In general, the USGS inundation area (Figure 2.8b) shows a similar pattern as the RFP (Figure 2.8a). In the results, areas with higher probability match well with the USGS-mapped inundated area. Beyond the USGS survey boundary, the results extracted the areas with high probabilities all over the research area. For example, in the subset along Gills Creek (Figure 2.8c), it is obvious that more areas closer to the creek with relatively high flooding potential were successfully identified beyond the existing boundary.

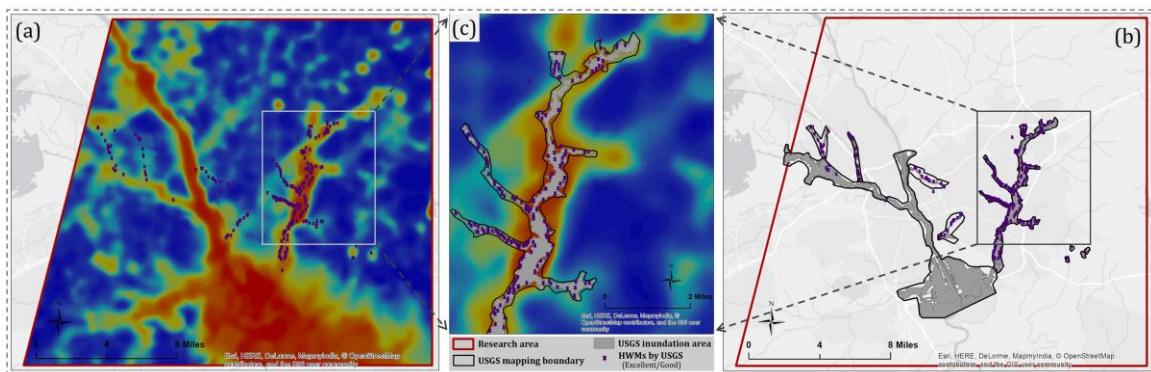


Figure 2.8 The RFP compared with USGS HWMs and USGS Inundation map

An RFP histogram comparison was conducted between the whole research area and those within the USGS inundated boundary (Figure 2.9). The result suggests a “U” shape histogram for the flooding probability within the research area where the histogram peaks occur in both low and high end, suggesting a bimodal distribution pattern with a mean flood probability of 0.34 (Figure 2.9a). After confining RFP within the USGS inundation boundary, it reveals a mono-modal pattern with a peak in high flooding probabilities with a mean of 0.83, a dramatic increase from 0.34. Detailed statistics can be seen in Table 2.3, where 62.41% of pixels constrained within the boundary have the flooding probabilities

larger than 80%. This indicates that areas within the USGS inundation boundary tend to have significantly higher flooding potentials than areas beyond the boundary.

We also extracted the flooding probability at the HWMs, the post-event manually surveyed ground truth points provided by USGS field surveyors. It is suggested that 67.15% of the HWMs have the flooding probabilities higher than 0.6 (Table 2.3). Given the fact that those HWMs are not likely to be distributed inside water bodies where highest flooding probabilities exist, but rather mostly alongside river channels and lake boundaries, the RFP in this chapter matches well with the HWMs.

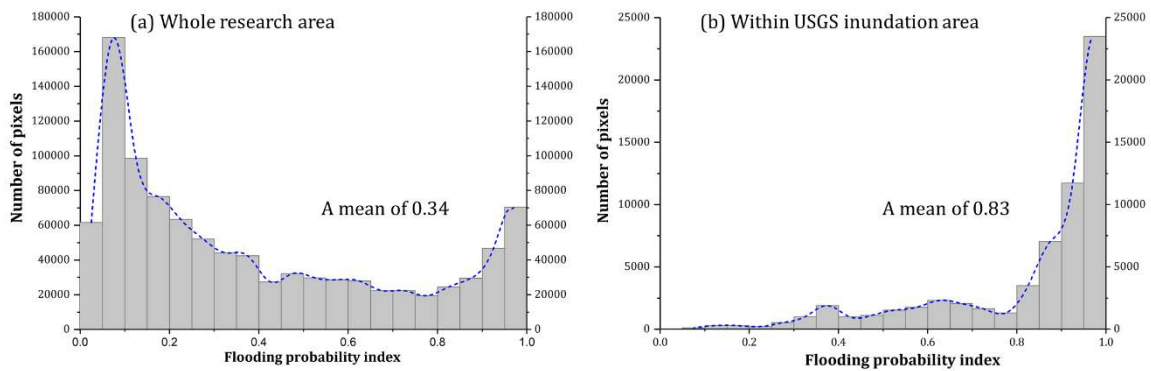


Figure 2.9 The EFP in the whole research area and in area within USGS inundation area.

Table 2.3 The RFP and HWMs within USGS inundation area.

RFP	Number of pixels (%)	Number of HWMs (%)
0 ~ 0.2	1153 (01.84%)	20 (7.22%)
0.2 ~ 0.4	4905 (07.80%)	27 (9.75%)
0.4 ~ 0.6	7406 (11.78%)	44 (15.88%)
0.6 ~ 0.8	10167 (16.17%)	69 (24.91%)
0.8 ~ 1.0	39236 (62.41%)	117 (42.24%)
Total	62876 (100.00%)	277 (100.00%)

In short, this chapter develops a flood reconstruction model that logistically combines the DEM, gauge readings, RS images, and social media, achieving a near real-time flooding probability estimation. The flooding surface derived from real-time DEM/gauge readings successfully identified the low-elevation flooded areas. The satellite-

derived NDWI contributes to identifying areas in high-elevation zone where DEM/gauge readings fail to cover. Further integration of real-time social media indicates that even a small amount of real-time Tweets data can significantly enhance the prediction of local floods. Superior to the official USGS map that has a delay of four months, the resulted RFP in this study is much less time- and labor-consuming and is not limited to the survey boundary. Its ability to provide continuous flooding probabilities largely contributes to a rapid and more accurate understanding of areas in need of urgent attention.

2.5 CONCLUDING REMARKS

As the severity of flood events has apparently increased, a comprehensive and rapid flood probability map is needed for local authorities to identify areas in need of attention and to mitigate flood-related damage. Taking the 2015 SC Flood as the study case, this chapter built a flooding reconstruction model to enhance the delayed remote sensed observation with spatially isolated real-time river gauges and Twitter data.

The primary findings of this chapter are: 1) the inclusion of multiple gauges compensates the uncertainties from local topological unevenness and the flaws of gauge data itself, and successfully identifies the low-elevation flooded areas; 2) Satellite-derived wetness contributes to identifying the high-elevation flooded areas, and its information loss due to delayed observation is compensated by integrating with the gauge and DEM-based flood layer; 3) Local enhancement with RT tweets proves that even a small amount of crowdsourcing data can largely improve the identification of high flood probability areas during a flood event.

The methodology designed in this chapter provides a spatially continuous probability surface that measures the likeliness of a certain area being inundated during a

flood event in a near real-time manner. The results in this chapter can greatly benefit local authorities and first responders for a rapid and comprehensive understanding of flooding situations. In addition, the proposed model could be generalized to other flooding cases. Other crowdsourcing databases could also be involved to provide supplemental information, aiding in a more robust local awareness. The methodology used in this chapter could seed a wide range of future flood studies for rapid and improved flood situational awareness in a city as well as at a regional level.

Although crowdsourcing platforms significantly improve the flood awareness acquisition, evidenced by promising results in this chapter, retrieving flood relevant posts remains a great challenge. On-topic social media posts (e.g., flood) only comprise a small proportion of the enormous volume of information in social media space. The 49 geotagged flood tweets used in this study were derived via the traditional keyword-matching approach and manual verification, a rather time/labor-consuming process. Given the characteristics of large volume and high streaming velocity of social media data, an automatic approach to retrieving on-topic social media posts is in great need. The following chapter (Chapter 3) designs a deep learning supported approach, aiming to automate the retrieval of on-topic social media posts.

CHAPTER 3

DEEP LEARNING SUPPORTED AUTOMATIC FLOOD RELEVANT VGI RETRIEVAL FROM SOCIAL MEDIA SOURCES²

3.1 INTRODUCTION

The rising of microblogging platforms renders us an important way to share information online, especially during severe disaster events. Social media, including Twitter, Facebook, and Flickr, empower millions of private citizens, as eyewitnesses, to voluntarily document their observations and thoughts in a highly up-to-date manner (Crampton, 2009; Ashktorab et al., 2014). Guided by the idea “citizen as sensors” proposed by Goodchild (2007), volunteers may contribute useful information regarding the intensity, severity as well as the extent of a disaster, providing time-critical situational awareness before authoritative information becomes available. Given the importance of on-topic (i.e., disaster-related) social media, extensive studies have attempted to harness useful volunteered information within social media for understanding and mitigating disasters, both natural and human-induced. Studies have demonstrated the utility of social media in mitigating a wide range of disasters including wildfire (Sutton et al., 2008; Slavkovikj et al., 2014; Ken and Capello, 2013; Vieweg et al., 2010), flood (Li et al., 2018; Huang et al., 2018a; Huang et

² Huang, X., Li, Z., Wang, C., & Ning, H. (2019a). Identifying disaster related social media for rapid response: a visual-textual fused CNN architecture. *International Journal of Digital Earth*, 1-23. Reprinted with permission from the publisher.

al., 2018b; Fohringer et al., 2015; Schnebele and Cervone, 2013; Schnebele et al., 2014; Avvenuti et al., 2016), earthquake (Yates and Paquette, 2010; Sakaki et al., 2010; Muralidharan et al., 2011; Yin et al., 2012; Resch et al., 2018; Avvenuti et al., 2018; Avvenuti et al., 2014; Earle et al., 2012), extreme precipitation and droughts (Tang et al., 2015; Ruiz Sinoga and León Gross, 2013; Hannak et al., 2012) and flu outbreak (Dredze, 2012; Schmidt, 2012; Gao et al., 2018; Lampos and Cristianini, 2012). The timely, individual-level characteristic coupled with their spatial context makes disaster-related social media a distinct source of ambient geospatial information (Stefanidis et al., 2013; Middleton et al., 2014; Verma et al., 2011) and a proxy to enhance disaster awareness (Gao et al. 2018; Imran et al., 2015).

Given the fact that on-topic social media only comprises a small proportion of the enormous volume of information in social media space, the practicality of social media has been greatly hampered by the limited approaches of automatic on-topic social media retrieval. The automation remains challenging because 1) the enormosity of social media pool that requires great computational power (Xu et al., 2016; Zikopoulos and Eaton 2011); 2) the complexity of the visual (picture) and textual (text) information that impedes the efficiency of traditional classification methods (Lew et al., 2006); and 3) the lack of integrated approach that considers fused characteristics from both visual and textual information (Gao et al., 2013). The first challenge has been addressed by the development of cloud computing, parallel computing, and the popular application of GPU (graphics processing unit) acceleration. The second challenge is being addressed with the advance of machine learning algorithms that greatly improve the classification accuracy of complex visual and textual information. For example, the state-of-the-art convolutional neural

network (CNN) techniques have achieved great performance on both picture labeling (Simonyan and Zisserman, 2014; Szegedy et al., 2017) and text classification (Kim, 2014). The third challenge, however, has not been thoroughly explored in the current literature. As two major components of a social media post, text and picture are both important when classifying on-topic social media posts. It is believed that the classification approach using a fused feature from visual and textual information allows cross-validation of each source, thus leading to better classification results (You et al., 2016). Therefore, the third challenge relies on an advanced visual-textual fused classification approach and merits further investigation.

This chapter presents an approach to automatically identifying on-topic social media posts by integrating their visual and textual information via a fused CNN architecture. Specifically, two CNN architectures are employed targeting on visual and textual posts of social media, respectively. The outputs of the two CNNs are further concatenated to form a fused representation, participating in the final classification step. Taking the 2015 SC flood and 2017 Houston flood as study cases, this chapter assesses the practicality of using visual-textual fused representation to label on-topic social media posts during a flood event. It also evaluates the performances of popular machine learning algorithms on the training of visual-textual fused vector. More importantly, it provides direct evidence on how much labeling accuracy can be achieved with the involvement of visual information.

3.2 RELATED WORK

3.2.1 Visual information labeling

The development of machine learning techniques enables the automation of labeling pictures via their visual characteristics. The traditional approaches have proven relatively efficient (Ofli et al., 2016; Gupta et al., 2013), including Random Forests that learns features via a multitude of decisive structures (Bosch et al., 2007); Support Vector Machines (SVM) that constructs one or multiple hyperplanes (Chapelle et al., 1999); and Naïve Bayes that learns probabilistically by assuming strong independence between features (McCann and Lowe, 2012). These baseline models have been outperformed by the rapidly evolving convolutional neural networks (CNNs) (Krizhevsky et al., 2012; Ciresan et al., 2011). Inspired by biological processes, CNN is a hierarchical neural network composed of input, output, and multiple hidden layers. Its form varies upon how those hidden layers are organized and realized. Since its proposal, CNN has been widely applied in various of fields that require advanced image processing technique, including remote sensing (Hu et al., 2015), social media analysis (Nguyen et al., 2017;), medical imaging processing (Bar et al., 2015), signal processing (Hershey et al., 2017) and video recognition (Yue-Hei Ng et al., 2015).

The great potential of CNN and the advance in high-performance computing markedly flourish the development of CNN architecture in picture recognition. AlexNet by Krizhevsky et al. (2012), for instance, consists of only 8 layers but was able to achieve a top 5 test error rate of 15.4% on ILSVRC (ImageNet Large-Scale Visual Recognition Challenge). VGG Net by Simonyan and Zisserman (2014) significantly improved the performance by utilizing a simpler but much deeper convolutional structure. Diverging

from the mainstream of stacking layers following a sequential structure, GoogleLeNet (Szegedy et al., 2015) used a composition of multiple inception modules and achieved improved performance (5.6% top-5 error) as well as computational efficiency. With a depth of up to 152 layers, the ResNet proposed by He et al. (2016) further improved the classification performance above human-level (3.57% top-5 error) by going deeper and leveraging residual networks.

In this chapter, the CNN architecture used to label visual information from social media is a transfer-learned and fine-tuned Inception-V3 architecture. More details about the architecture design and transfer learning phrase are presented in Section 3.3.1.

3.2.2 Textual information labeling

Apart from the success in picture labeling, CNN models have also shown a great potential in natural language process (NLP) and achieved excellent performances in semantic parsing (Yih et al., 2014), sentimental analysis (Ouyang et al., 2015), sentence modeling (Kalchbrenner et al., 2014), sentence labeling (Wang et al., 2012; Kim, 2014) and other NLP tasks (Sutskever et al., 2014). Within the NLP tasks, CNN models are able to capitalize on distributed word representations by first learning word vectors through neural language models, then forming a matrix to be used for classification (Zhang and Wallace, 2015; Collobert et al., 2011). Extensive studies have explored the capability of CNN in labeling texts to a certain topic. Kim (2014), for example, designed a simple one-layer CNN architecture for sentence classification utilizing word vectors trained by Mikolov et al. (2013) and achieved a remarkable classification accuracy across several datasets. Kalchbrenner et al. (2014) designed a CNN architecture by applying a dynamic K-Max Pooling strategy over linear sequences and found that it outperformed the baseline models,

including SVM and neural bag-of-words (NBOW). Feng and Sester (2018) found that CNN coupling with word vector representations performed better in flood-related text classification than traditional machine learning algorithms, including SVM, Random Forest, Logistic Regression, and Naïve Bayes. Lin et al. (2016) adopted Kim's network (Kim 2014) and tested on Weibo, a Chinese microblogging service, to extract information related to earthquakes and achieved accuracy up to 90.7% in labeling on-topic posts.

The strong performance achieved with those relatively simple CNN architectures suggests their great potentials in text labeling. The study in this chapter modifies the architecture proposed by Kim (2014) for text classification. More details can be found in Section 3.3.2.

3.2.3 Towards a fused labeling

The outstanding performances of CNN in picture and text classification have raised a tendency to merging visual and textual information towards a fused classification approach. Under the assumption that a visual-textual fused classification allows self-correction of intrinsic errors from a single source (You et al., 2016; Laura et al., 2017; Huang et al., 2019b), a fused classification method combines the features extracted from both pictures and texts and therefore leads to a more robust classification. This is especially the case when dealing with disaster-related social media posts where both their visual and textual information may contain important information. A few attempts have been made to combine visual and textual information. Huang et al. (2018c) proposed a visual-textual fused approach in labeling flood-related tweets by integrating flood sensitive words to remove wrongly classified pictures by CNN. However, it only proves that textual information (flood sensitive words) can be applied to refine the result from picture labeling.

You et al. (2016) designed a cross-modality regression for joint visual-textual sentimental analysis of social multimedia and achieved a great performance. Avgerinakis et al. (2017) proposed a visual and textual analysis by fusing the results from two modalities using non-linear graph-based techniques. Bischke et al. (2017) proposed a fused framework that combined both features to a single vector for final classification.

The visual-textual approach proposed in this chapter integrates a transfer-learned Inception-V3 architecture (extracting visual features) and modified word embedded CNN architecture (extracting textual features). More details can be found in Section 3.3.3.

3.3 METHODS

The conceptual workflow of the proposed methodology is presented in Figure 3.1. Texts and pictures from a social media post are refined in the pre-processing process and fed to visual CNN and textual CNN respectively for feature extraction. Well-trained on designed training datasets, both CNN architectures have the capability of providing feature vectors that describe the characteristics of texts and pictures. By concatenating the visual vectors and textual vectors, a fused feature vector is developed and input to the final classification architecture. The final output is a binary class (on-topic or off-topic) of any given social media post.

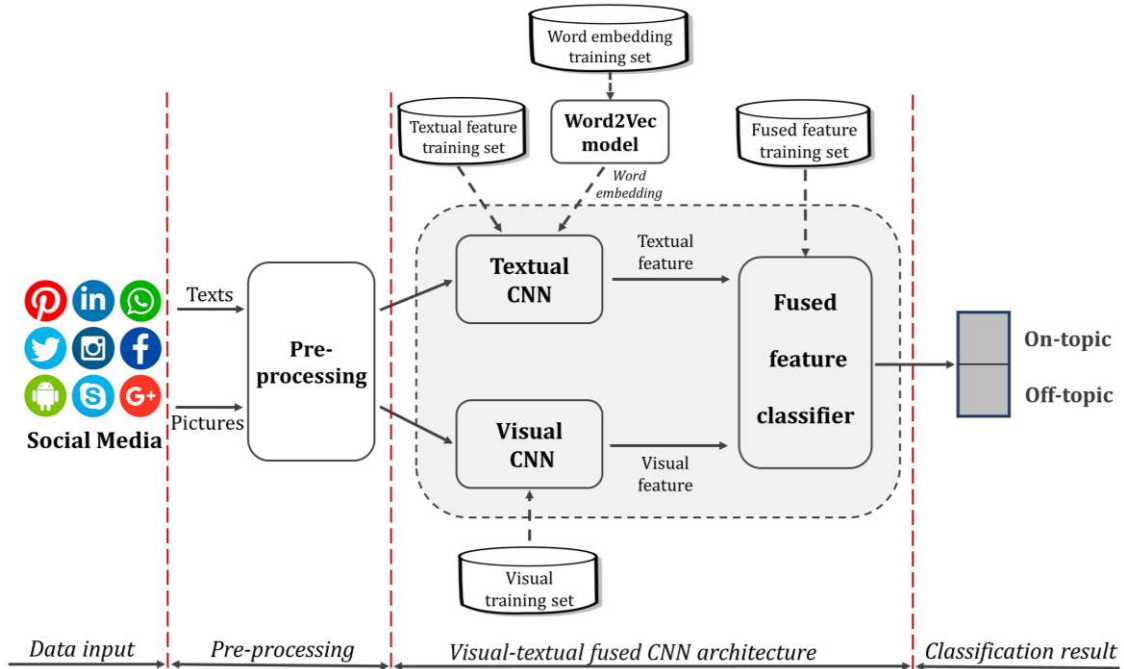


Figure 3.1 Conceptual workflow.

3.3.1 Transfer-learned and fine-tuned CNN architecture (Visual CNN)

Transfer learning is the technique that transfers the network weights on a previous task to a new task, under the assumption that features extracted from the previous dataset are generic enough to be useful in the context of a new dataset (Yosinski et al., 2014). The base model to tackle the visual classification problem in this chapter is Inception-V3 architecture with a 3.6 % top-5 error (Szegedy et al., 2016). To transfer this network to a binary classifier (on-topic or off-topic), several top layers specific to ILSVRC problems are removed. New layers are added to the model in the following order: AvgPool, FC (1024 features), Dropout, and Softmax (2 classes), as shown in Figure 3.2.

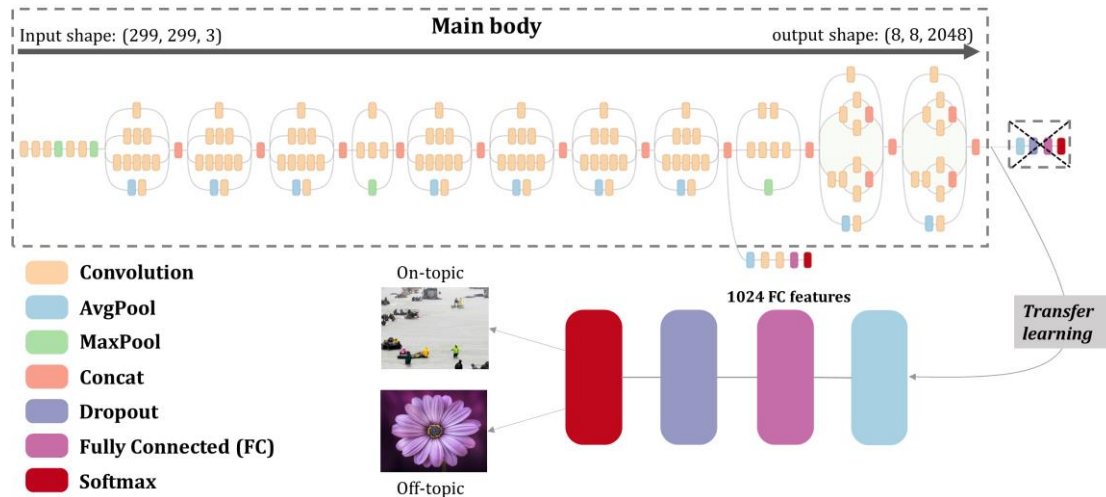


Figure 3.2 Transfer learned model from Inception-v3.

To retrain the newly composed model, a two-stage transfer learning strategy is applied:

Stage 1: freeze all but the penultimate layer and re-train the last FC layer;

Stage 2: unfreeze lower convolutional layers and fine-tune their weights.

In stage 1, the main body of the model is selected to be non-trainable (weights are not updating themselves), and only the newly added FC layer is trainable. The rationale is that the main body of Inception-v3 is capable of providing rich and generic feature representations of the data provided, and the newly added FC layers (associated with the following Dropout and Softmax layer) are only treated as a classifier trained on the on-topic and off-topic visual training set (described in Section 3.4.2).

After the completion of stage 1, lower convolutional layers are further released to be trainable on the same training dataset in stage 1 through the backpropagation process. This stage is motivated by the idea that the earlier features in a CNN model contain more generic features that can be generalized to other tasks (no need to be fine-tuned), but the later features in the model become more specific to previous designated classes (need to be fine-tuned). In this stage, the top 2 inception blocks in the main body inception-v3 are

further released to be trainable while other low-level layers are still kept frozen to prevent the model from being overfitted.

The functionality of various layers in Figure 3.2 is summarized in Table 3.1.

Table 3.1 Layer functionality summary

Layer type	Functionality
Convolution	<p>Learning features by applying a convolution operation to the input:</p> $x_{ij}^l = \sum_{a=0}^{m-1} \sum_{b=0}^{m-1} w_{ab} x_{(i+a)(j+b)}^{l-1}$ <p>where a $m \times m$ filter w is applied to a previous layer x^{l-1}, convoluting it down to the current layer x^l.</p>
AvePool	<p>An extreme type of dimensionality reduction where a $h \times \omega \times d$ feature map is further reduced to $1 \times 1 \times d$ by averaging values in $R^{h \times \omega}$.</p>
MaxPool	<p>Reducing the spatial size of the representation by selecting the max value as representative:</p> $x_{ij}^l = \text{Max}_{(i+e),(j+f) \in R^p} x_{(i+e)(j+f)}^{l-1}$ <p>where R^p denotes the pooling filter domain.</p>
Concat	<p>A concatenating function that merge shorter vectors to form a single long vector:</p> $X = x_1 \oplus x_1 \oplus x_2 \oplus \dots \oplus x_n$ <p>where X denotes concatenated vector and x_i denotes short vectors.</p>
Dropout	<p>A regulation function that prevents the co-adaption of hidden units by randomly setting a proportion to 0 in forward propagation, thus significantly reducing the chance of network being overfitted (Srivastava et al. 2014). I.e., replace $y = W \cdot z + b$ with $y = W \cdot (z \circ r) + b$ where “\circ” represents element-wise multiplication and W, z, b, and r to be weight matrix, feature vector, bias term and ‘masking’ vector, respectively (Kim 2014)</p>
FC	<p>Flattening high dimensional features by connecting every neuron in the prior layer to the next layer.</p>
Softmax	<p>A function that classifies mutually exclusive labels and makes predicted probabilities to each label add up to 1. A binary Softmax function, in this case, can be simplified to a logistic function:</p> $y = \frac{1}{1 + e^{-(W \cdot (z \circ r) + b)}}$

3.3.2 Word embedded CNN architecture (Textual CNN)

The construction of a word embedded CNN consists of two steps:

- High-dimensional word representation (word vector) acquisition;
- Application of CNN in sentence matrix formed by word vectors.

Given the fact that textual patterns differ a lot in short-text posts in social media compared to formal sources, including news and formal articles, it is necessary to train word vectors specifically for social media posts. To acquire word vectors, the technique used in this chapter is Word2Vec, a shallow neural network with a single hidden layer, but proved to be powerful in providing 300-dimension vectors representing the word characteristics (Mikolov et al., 2013). A word vector database is then built to enable the formation of a sentence matrix, which is the input for a CNN architecture designed based on the work by Kim (2014) (Figure 3.3).

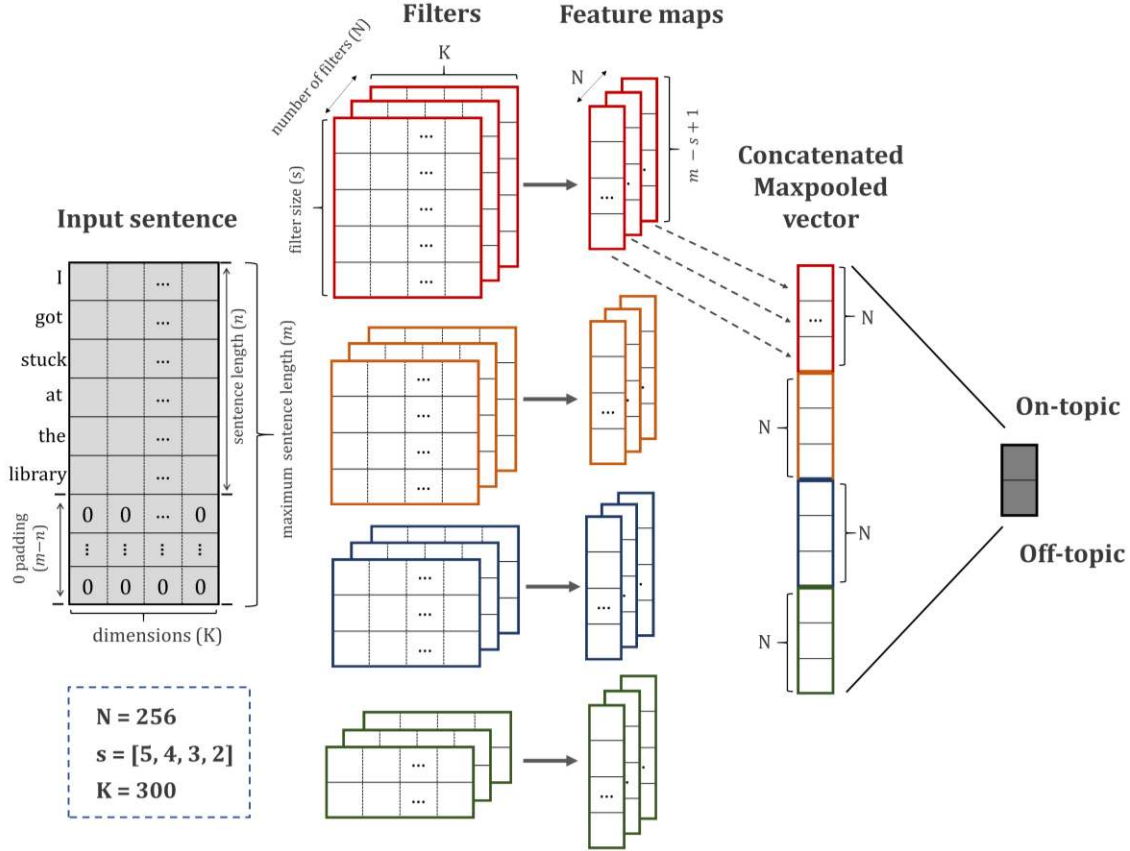


Figure 3.3 Word embedded CNN architecture.

The input sentence is described by multiple 300-dimension vectors, which form an image-like matrix that can be processed by convolutional algorithms. Suppose that the maximum word length in a sentence is m and the dimension of a word vector is K , the sentence matrix that serves as the input to the CNN model can be represented by $X \in R^{m \times K}$. Let $x_i \in R^K$ be the K -dimensional word vector to the i -th word in the input sentence. Each sentence can be represented as:

$$X = x_1 \oplus x_2 \oplus x_3 \oplus \dots \oplus x_m \quad (3.1)$$

where \oplus is the concatenation operator.

Given that not every sentence reaches the maximum length (m), 0 padding strategy is applied when necessary. Suppose that a sentence has a length of n ($n < m$), the input sentence can be rewritten as:

$$X = \underbrace{x_1 \oplus x_2 \oplus \dots \oplus x_n}_n \oplus \overbrace{x_{n+1}(0) \oplus \dots \oplus x_m(0)}^m \quad (3.2)$$

where $x_i(0)$ denotes a vector padded with 0.

Let $x_{i,j}$ refer to the subset of concatenation words from word x_i to word x_j . Let $w \in R^{sK}$ to be the domain of a certain filter with a vertical size of h words. When this 2D filter is applied to a window of word from $x_{i:i+s-1}$, a new feature o_i is generated:

$$o_i = f(w \cdot x_{i:i+s-1} + b) \quad (3.3)$$

where b is the bias term, f is an activation function (following the work of Kim (2014), a hyperbolic tangent function is applied) and " \cdot " is the dot product from the filter and the word matrix from x_i to x_{i+s-1} . When this filter is moving in a stride of 1, it generates a feature map $C \in R^{m-s+1}$ as:

$$C = [c_1, c_2, c_3, \dots, c_{m-s+1}] \quad (3.4)$$

After the generation of feature map C for a certain filter w , a pooling function is applied to induce a fixed-length vector (Lin et al., 2016). A commonly used max pooling strategy (Collobert et al., 2011) is applied, taking the maximum value from each feature map C :

$$\hat{C} = \max(C) \quad (3.5)$$

where \hat{C} represents the maximum value in its elements.

The application of this max pooling strategy provides a single feature (\hat{C}) corresponding with its filter (w). In this study, given a certain filter size s , a total number of N filters are used to obtain a comprehensive understanding of the input sentence, resulting in a dense N -dimensional vector z :

$$z = [\hat{C}_1, \hat{C}_2, \dots, \hat{C}_N] \quad (3.6)$$

Those z vectors are further concatenated to a long dense vector. Let t be the total number of filter size. The final concatenated vector $Z_{textual} \in R^{TN}$ can be represented as:

$$Z_{textual} = [z_1, z_1, \dots, z_T] \quad (3.7)$$

The concatenated textual vector $Z_{textual}$ is further processed by Softmax regression to generate two neurons with binary labels.

3.3.3 Fusing visual and textual information

The fusion of visual and textual information in this section utilizes the penultimate layer in word embedded CNN architecture and a transfer-learned and fine-tuned Inception-V3 architecture. Both CNN models are well trained with on-topic and off-topic disaster social media (Figure 3.4).

When a social media post is fed to the fused architecture, its textual and visual information is simultaneously and respectively passed through a well-trained word embedded CNN for generating textual features and a transfer-learned Inception-V3 for generating visual features. Each model returns a 1024-dimension vector characterizing the visual and textual information of a social media post separately. The concatenated vector with 2048 dimensions, therefore, represents a fused feature describing visual-textual information integrally:

$$Z_{fused} = Z_{textual} \oplus Z_{visual} \quad (3.8)$$

where $Z_{textual}$ and Z_{visual} denote textual vector and visual vector, respectively, both with 1024 dimensions. Z_{fused} denotes the concatenated vector with 2048 dimensions, describing a fused characteristic from both text and picture of a social media post. Noted that the proposed approach doesn't require the coexistence of visual and textual input. The corresponding feature in the fused 2048-dimension vector is automatically padded with 0

if the input lacks an information source, either visual or textual. In this study, almost all social media posts contain textual information, but only a proportion of them contain visual information. Therefore, I targeted on the influence of Z_{visual} , the additional visual information input, on the classification merely based on $Z_{textual}$.

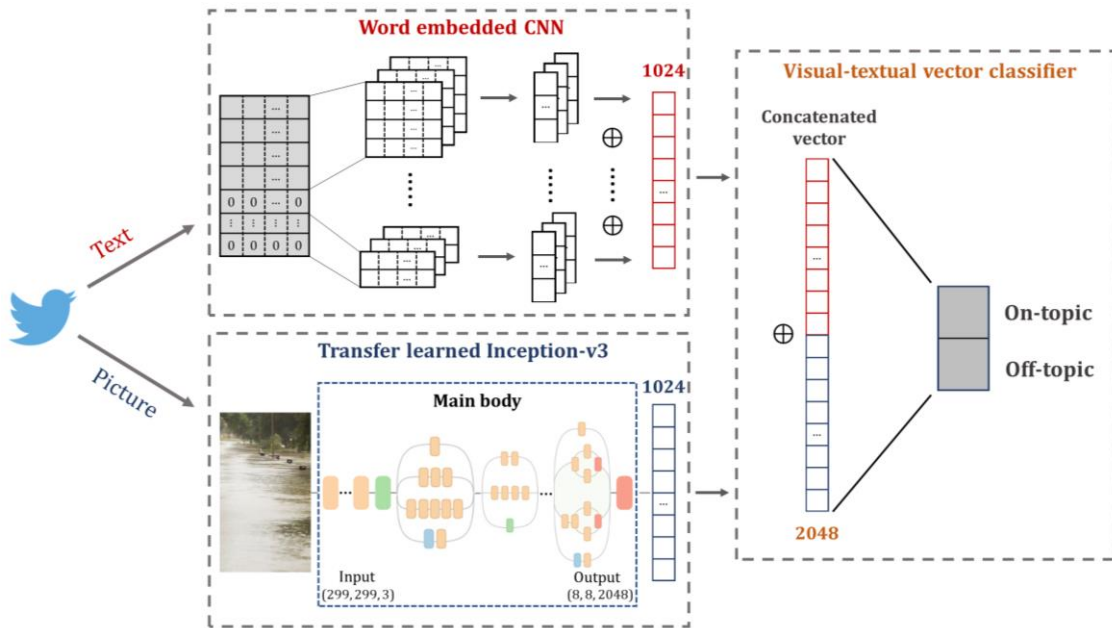


Figure 3.4 Fusion of visual and textual information.

The fused vector is further trained using popular machine learning algorithms to derive binary labels: on-topic and off-topic. Those machine learning algorithms used in this study include Logistic Regression (LogR), Linear Discriminant Analysis (LDA), Decision Tree (DT), Support Vector Machine (SVM), Random Forest (RF) and Naïve Bayes (NB). To train the algorithms above, a training set is developed, containing labeled social media posts with text only and with both text and pictures. This training phrase enables the algorithms to handle a variety of inputs and make classification decisions accordingly.

3.4 DATASETS

Two specific floods, 2015 SC flood and 2017 Houston flood (Figure 3.5), are selected as study cases. Geotagged tweets containing verified texts derived from the 2015 SC flood (Figure 3.5b) and flood pictures from various sources (Table 3.2) are applied to train the textual CNN and visual CNN, respectively. Their concatenated feature extracted from well-trained CNNs is further evaluated using geotagged tweets derived from the 2017 Houston flood (Figure 3.5c).

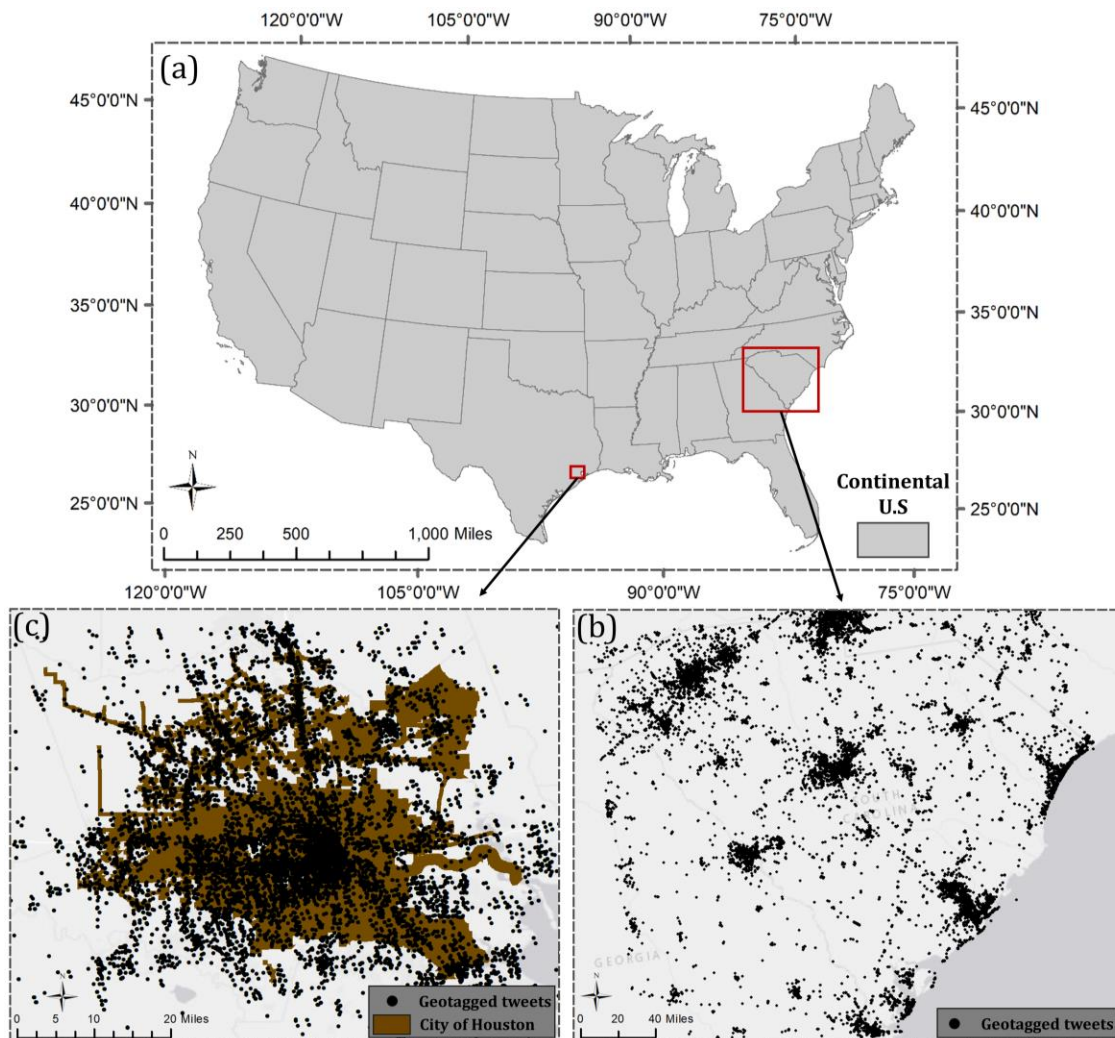


Figure 3.5 Research area for two flooding cases with their geotagged tweets; (a) Continental U.S.; (b) South Carolina flood in 2015 with 934,896 geotagged tweets from

Oct 2nd to Oct 9th; (c) Houston flood in 2017 with 501,516 geotagged tweets from Aug 25th to Sep 1st.

3.4.1 Visual training set

To transfer-learn and fine-tune the CNN architecture, a balanced visual training set from popular searching engines and social media platforms is first developed. The multi-source characteristic of the training set allows better generalization that reduces model overfitting. The dataset contains 5500 flood pictures (positive samples) and 5500 non-flood pictures (negative samples), as summarized in Table 3.2. A stratified k-fold ($k = 5$) cross-validation rule is followed to split the training set. It is a commonly used estimation approach that partitions the dataset randomly into k equal-size subsamples, where one single subsample is retained for validation and the remaining $k-1$ subsamples are used for training.

Table 3.2 Visual training set.

Sources	Method	number of pictures
<i>Flood pictures (positive)</i>		
Google	Pictures with keyword “flooding”	500
Baidu	Pictures with keyword “flooding” and “Hongshui” (“flooding” translated to Chinese Pinyin)	500
Flickr	Pictures tagged by “flooding”	500
Twitter & Instagram	Pictures from tweets with keyword “flood*” or hashtag “flood*” from Dec 1 st 2015 to Dec 1 st 2016 in U.S and manually verified.	4000
<i>Positive total</i>		5500
<i>Non-flood pictures (negative)</i>		
Twitter & Instagram	Pictures extracted from tweets in U.S from Dec 1 st 2015 to Dec 1 st 2016 and manually verified.	5500
<i>Negative total</i>		5500

3.4.2 Textual training set

The textual training set in this study contains two subsets: 1) word embedding training set, aiming train the embedding model, Word2Vec (Mikolov et al., 2013), to learn high-dimensional word representation (word vector); 2) Textual feature training, aiming to train the textual CNN to provide textual feature (1024-dimension vector) that characterizes the textual information (Table 3.3).

Table 3.3 Textual training set.

Subsets	Sample size	Duration	Purpose
Word embedding training set (embedding model)	13,830,023	Jan 1 st , 2017 to Dec 31 st , 2017	To train the embedding model, Word2Vec, to learn high-dimensional word representations, providing 300-dimension vector for each word before feeding sentences to the neural network.
Textual feature training set	5706	Oct 2 nd , 2015 to Oct 9 th , 2015 (SC Flood)	To train the textual CNN to learn the meaning of textual information of a post, providing textual features (1024-dimension vector) that well characterize the given textual information

The word embedding training set contains a total of 13,830,023 selected sample tweets in 2017. They were downloaded using the Twitter Stream API and are stored in a Hadoop computer cluster. The usage of a large corpus of tweets to train the word embedding model contributes to well-summarized word vectors that are specifically for short-text social media posts.

After training the word embedding model, the textual CNN architecture was further trained (described in Section 3.3.2) to provide textual features (1024-dimension vector) that characterize the textual information posts. In this textual feature training set, a total of

5,706 tweets were manually labeled during the 2015 SC flood (Oct 2nd to Oct 9th) based on their textual content only. This balanced dataset contains 2852 positive samples (flood-related) and 2852 negative samples (non-flood related).

3.4.3 Fused feature training set

The fused feature training set aims to train the visual-textual feature (2048-dimension vector) classifier (described in Section 3.3.3) to generate on-topic or off-topic labels. The dataset used in this training phase was developed during the 2017 Houston Flood period (Aug 25th to Sep 1st). 2,092 positive tweets were manually verified based on the content of their texts, pictures, or both, among which 825 are picture included tweets. The same amount of negative tweets (2,092) during the event were randomly selected and verified as non-flood related, among which 1,042 were picture included tweets. The fused feature training set enables the visual-textual classifier to produce binary labels given both sufficient inputs (a tweet contains both text and picture) and insufficient inputs (a tweet contains text but lacks picture).

Tweeted texts are noisy and messy, and therefore, a textual pre-processing is necessary to trim and formalize the inputs before feeding to the Word2Vec and word embedded CNN. During the pre-processing, punctuation marks, emoticons and numbers were removed from the text. Stemming and lemmatization techniques were also applied in the process. Stemming identifies the common root form of a word by removing or replacing word suffixes (e.g., “flooding” is stemmed as “flood”), while lemmatization identifies the inflected forms of a word and returns its base form (e.g., “better” is lemmatized as “good”). For tweets that contain URLs, a regular expression is used to match and remove URLs in their texts. Stopwords represent the most common words in a language, hardly contributing

to the meaning of a sentence. In this pre-processing step, a list of stopwords was retrieved from Natural Language Toolkit (NLTK) library (<http://www.nltk.org/>) and words in the list are further removed. I also applied some basic transformations, for example, “ve” to “have”, “ll” to “will”, “n’t” to “not”, “re” to “are” and etc, to enhance the comprehension of the algorithm.

All pictures are resampled to 299×299 via bilinear interpolation algorithm before feeding to the visual CNN.

3.5 RESULTS AND DISCUSSION

3.5.1 Visual CNN

The visual CNN architecture was trained on the visual training set described in Section 3.4.2 using a 5-fold cross-validation strategy. The training phase (2 stages) took 24 mins 41 seconds for a single fold using NVIDIA GeForce GTX 1080Ti GPU for acceleration.

Table 3.4 Visual CNN performance.

	Fold 1	Fold 2	Fold 3	Fold 4	Fold 5	Average	SD
Accuracy	93.32%	92.98%	94.50%	91.96%	91.95%	92.94%	0.95%
AUC	0.983	0.987	0.989	0.978	0.971	0.982	0.006

The model reached a stable performance for all folds with an average accuracy of 92.94% and a standard deviation (SD) of 0.95% (Table 3.4). The AUCs (Area Under the Curve) for all ROC (Receiver Operating Characteristic) curves in Figure 3.6a were summarized in Table 3.4. The average AUC for all five folds is 0.982 out of 1 (perfect classifier), also indicating the high performance and high stability of the visual CNN.

The accuracy curves for fold three are demonstrated in Figure 3.6b. After 200 epochs, it reached an accuracy higher than 90% in both training and validation sets. The gradual convergence of the training accuracy curve and validation accuracy curve indicates

that the two-stage learning strategy successfully prevents overfitting. The significant validation improvement at the beginning of Stage 2 is due to the fine-tuning of the newly released inception-v3 blocks. Given the unique characteristics of flood pictures and the popularity of pictures with similar patterns (Feng and Sester, 2018), an accuracy over 90% with AUC curve over 0.95 is considered acceptable compared with other flood picture classification results (Avgerinakis et al., 2017; Bischke et al., 2017).

The good performance of visual CNN in classifying flood and non-flood pictures guarantees that the intermediate penultimate layer (1024-dimension vector) effectively summarizes the characteristics of flood pictures. The vector thus can be used to represent a visual feature of a social media post.

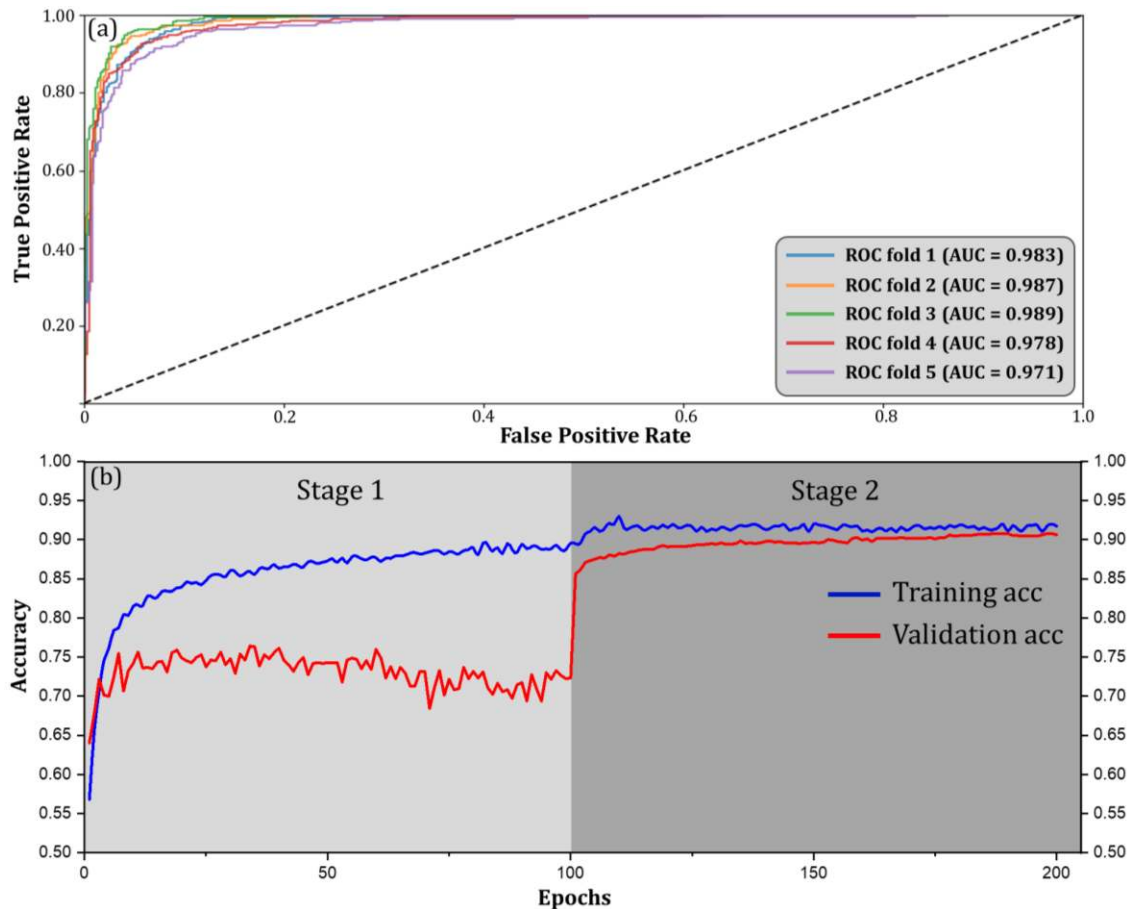


Figure 3.6 Model performance of the visual CNN.

3.5.2 Textual CNN

Given the fact that well-trained word vectors are the prerequisite for a robust textual CNN, I first evaluated the 300-dimension word vectors generated by Word2Vec, specifically trained on a developed social media pool. The cosine-similarity distance was applied to examine the similarity of word vectors to a target vector in hyper-dimensional space. A cosine distance ranges from -1 meaning exactly opposite, to 1 meaning exactly the same, with 0 meaning unrelated.

Table 3.5 demonstrates some common words and the Word2Vec-generated top 5 words with similar meanings ranked in the cosine-similarity distance. For example, the closest word vector to “bad” is the word vector of “terrible” with a cosine distance of 0.635, followed by “horrible” (0.610), “shitty” (0.553), “awful” (0.524) and “crappy” (0.469). A similar pattern is also found for “good”, whose close word vectors include “great”, “decent”, etc., all with the same sentimental preference. For disaster-related keywords like “flood” and “hurricane”, word vectors with high similarity tend to have either high sentence structure relevance (“hurricane” and “Harvey”), high synonymousness (“hurricane” and “storm”) or strong causal relationship (“flood” and “damage”, “hurricane” and “flood”).

The linear relationship between different vectors was maintained throughout the training phase. For example, the vector “flood” minus vector “water” (flood-induced) was similar to that of “thunderstorm”, “storm” and “tornado” minus “wind” (storm-induced). Similarly, the vector pattern of “earthquake – quake” is most similar to “flood – water”, and that of “father – son” is most similar to “mother – daughter” (Table 3.5). Trained from

a massive social media training pool, the Word2Vec model not only extracted meaningful vector representations but preserved linear relations among different word vectors.

Table 3.5 Word2Vec training results (top 5 neighboring words with their cosine-similarity distances).

Example words	Top 1	Top 2	Top 3	Top 4	Top 5
bad	terrible (0.635)	horrible (0.610)	shitty (0.553)	awful (0.524)	crappy (0.469)
good	great (0.639)	decent (0.563)	nice (0.489)	amazing (0.469)	interestin g (0.461)
flood	hurricane (0.596)	damage (0.581)	evacuate (0.560)	storm (0.534)	underwat er (0.496)
hurricane	storm (0.702)	Harvey (0.642)	flood (0.596)	tornado (0.477)	disaster (0.463)
father – son + daughter	mother (0.561)	grandmoth er (0.533)	wife (0.531)	woman (0.404)	beloved (0.403)
earthquake – quake + water	flood (0.523)	pouring (0.492)	underwater (0.444)	rain (0.418)	evacuate d (0.413)
flood – water + wind	thunderstor m (0.512)	storm (0.498)	tornado (0.484)	rainfall (0.464)	gust (0.447)

Note. Cosine-similarity distance is calculated as $\sum_{i=1}^n A_i B_i / (\sqrt{\sum_{i=1}^n A_i^2} \sqrt{\sum_{i=1}^n B_i^2})$ where A_i and B_i represent components of vector A and B. The idea of a word vector δ similar to a vector resulting from a linear function: $\alpha - \beta + \gamma$ can be interpreted as word vector $\delta - \gamma$ similar to vector $\alpha - \beta$.

The classification performance of textual CNN using the sentence matrix build from these word vectors was then evaluated.

Table 3.6 Textual CNN performance.

	Fold 1	Fold 2	Fold 3	Fold 4	Fold 5	Average	SD
Accuracy	94.17%	93.13%	92.54%	93.64%	93.79%	93.45%	0.63%
AUC	0.970	0.963	0.960	0.967	0.966	0.965	0.004

Accelerated by GPU and CUDA architecture, the designed CNN finished the training in 21 seconds through 200 epochs for a single fold. The results indicate a high performance with stability. The average accuracy for all five folds reaches 93.45% with a SD of 0.63% and the average AUC reaches 0.965 with a SD of 0.004 (Table 3.6). Detailed ROC curves for all five folds and training curve for fold 1 (best performance) are presented in Figure 7. After the 75th epoch, both of the training accuracy curve and the validation accuracy curve started to level and stabled above 90%, indicating no significant overfitting problem (Figure 3.7b). Consecutive and stable training loss was also observed throughout the training phase (Figure 3.7c).

In general, the designed textual CNN performs remarkably well in classifying flood-related and non-flood related tweets based on their textual information. It is partly due to the uniqueness of word patterns in social media during a flood event. For instance, we found that the majority of texts in flood-related tweets in the training pool contain high flood-relevant keywords like “flood”, “rain”, “underwater”, etc. This pattern can be easily recognized and adopted as a classification strategy by the designed textual CNN architecture, thus resulting in high classification accuracy. That being said, with the same keyword distribution patterns noticed in other disasters like hurricanes (Bakillah et al., 2015), earthquakes (Gao et al., 2013), and wildfires (Slavkovikj et al., 2014), this method could be easily generalized to other disaster cases given a proper training set.

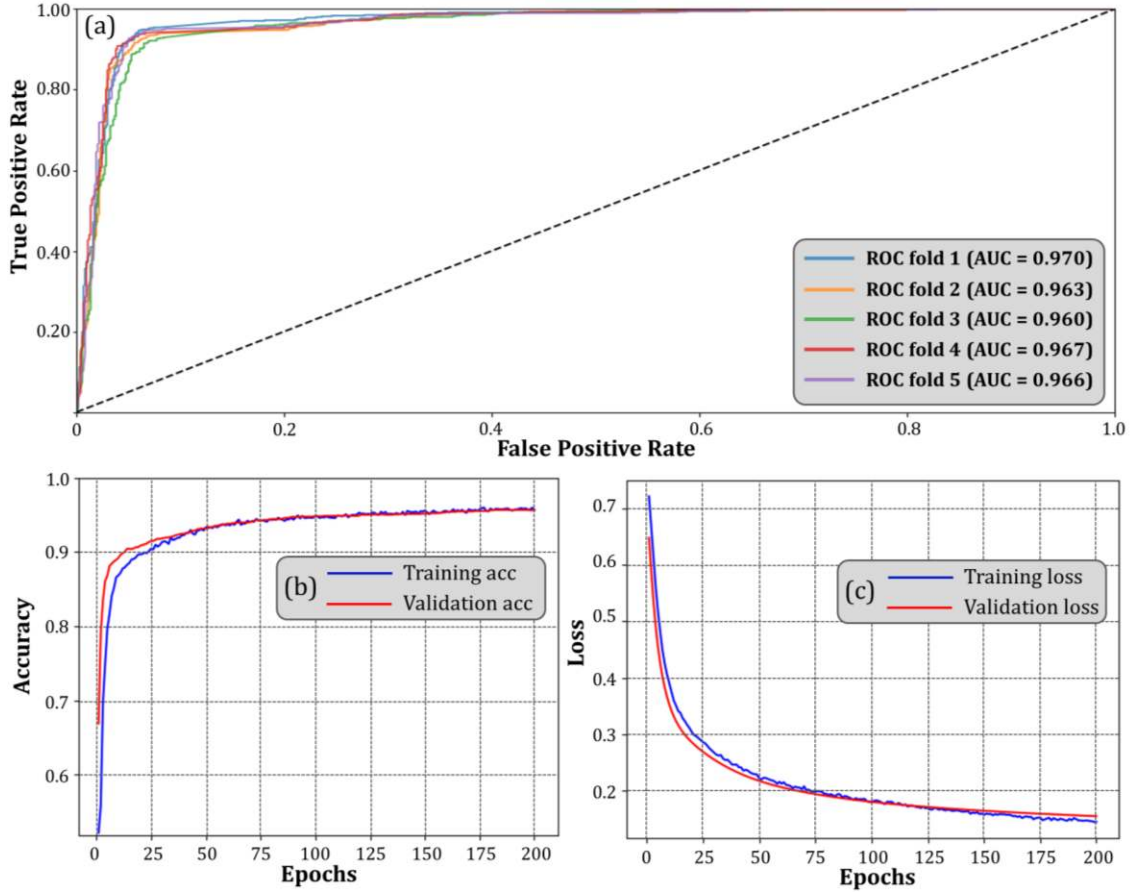


Figure 3.7 (a) Textual CNN ROC curve for all five folds; (b) Training accuracy curve for fold one; (c) Training loss curve for fold one.

3.5.3 Visual-textual fused classification

The high performance of the designed visual CNN and textual CNN proves the functionality of their extracted feature vectors. In this section, I evaluated the performance of various machine learning algorithms in giving binary labels based on Z_{fused} , the concatenated fused vector with 2048 dimensions. Similar to training the visual and textual CNN, the 5-fold cross-validation was applied to test LogR, DT, RF, NB (Gaussian), NB (Multinomial), NB (Bernoulli), DA (LDA), DA (QDA), SVM (Linear), SVM (Polynomial), SVM (RBF) and SVM (Sigmoid). As shown in Table 3.7, LogR achieved the best performance with an average accuracy of 96.5%, followed by SVM (Linear) with

96.3%, SVM (RBF) with 94.4%, and SVM (Sigmoid) with 94.1%. RF and DT also performed well with average accuracy reaching over 90%. Significant overfitting was observed in SVM (Polynomial) as it has a low average accuracy (69.7%) and the highest SD (4.87%).

Table 3.7 Visual-textual fused classification accuracy.

Method	Fold 1	Fold 2	Fold 3	Fold 4	Fold 5	Average	SD
LogR	96.3%	95.5%	97.1%	97.6%	96.2%	96.5%	0.73%
DT	91.5%	89.9%	92.5%	91.0%	90.6%	91.1%	0.87%
RF	93.1%	93.2%	93.7%	94.7%	92.9%	93.5%	0.64%
<i>NB:</i>							
Gaussian	88.1%	87.0%	88.5%	90.3%	89.1%	88.6%	1.09%
Multinomial	76.4%	75.3%	77.6%	79.2%	76.7%	77.0%	1.31%
Bernoulli	67.8%	68.1%	70.7%	69.6%	68.3%	68.9%	1.09%
<i>DA:</i>							
LDA	86.3%	87.2%	86.6%	88.5%	88.3%	87.4%	0.88%
QDA	72.2%	73.6%	75.2%	73.9%	73.7%	73.7%	0.95%
<i>SVM:</i>							
Linear	96.2%	95.6%	96.2%	96.9%	96.4%	96.3%	0.42%
Polynomial	74.1%	62.2%	75.4%	66.5%	70.2%	69.7%	4.87%
RBF	94.7%	93.7%	95.0%	94.9%	93.9%	94.4%	0.54%
Sigmoid	94.5%	93.4%	94.3%	94.4%	93.7%	94.1%	0.43%

Note. LogR, DT, RF, NB, and DA denote Logistic Regression, Decision Tree, Random Forest, Naïve Bayes, and Discriminant Analysis, respectively. LDA and QDA denote Linear Discriminant Analysis and Quadratic discriminant analysis, respectively. Linear, Polynomial, RBF (Radial Basis Function) and Sigmoid are kernel functions utilized in the SVM classifier. Classification method with an average accuracy over 90% for all five folds is highlighted in bold.

To examine whether classification using visual-textual fused vector (Z_{fused}) is better than using textual vector alone ($Z_{textual}$), I tested the algorithms with average accuracy over 90% in Table 3.7 using Z_{fused} and $Z_{textual}$ as input, respectively. Those algorithms include LogR, DT, RF, SVM (Linear), SVM(RBF), and SVM (Sigmoid). The whole dataset was randomly divided into a training set (70%) and a testing set (30%). The

results suggest that all the algorithms benefited from the additional input of visual information (Table 3.8). For instance, LogR achieved a classification accuracy of 95.2% using Z_{fused} , a 12.6% increase from using $Z_{textual}$. Similar improvements were found for DT with a 12.1% increase, RF with a 11.6% increase, and SVM (Sigmoid) with a 14.4% increase (Table 3.8).

Table 3.8 Visual-textual fused classification compared with textual only.

Method	Accuracy	
	Textual only	Visual-textual fused
LogR	82.6%	95.2%
DT	77.6%	89.7%
RF	80.5%	92.1%
SVM (Linear)	82.9%	92.7%
SVM (RBF)	79.5%	90.2%
SVM (Sigmoid)	79.2%	93.6%

Adding visual inputs from social media, better classification performance for those algorithms above was also reflected in their ROC curves (Figure 3.8). AUC improvements were observed, especially for LogR (AUC improved from 0.887 to 0.945), DT (AUC improved from 0.808 to 0.881), and SVM (Linear) (AUC improved from 0.861 to 0.931). The AUC improvement for all six algorithms suggests that the visual-textual fused feature exhibits more robustness in extracting on-topic posts.

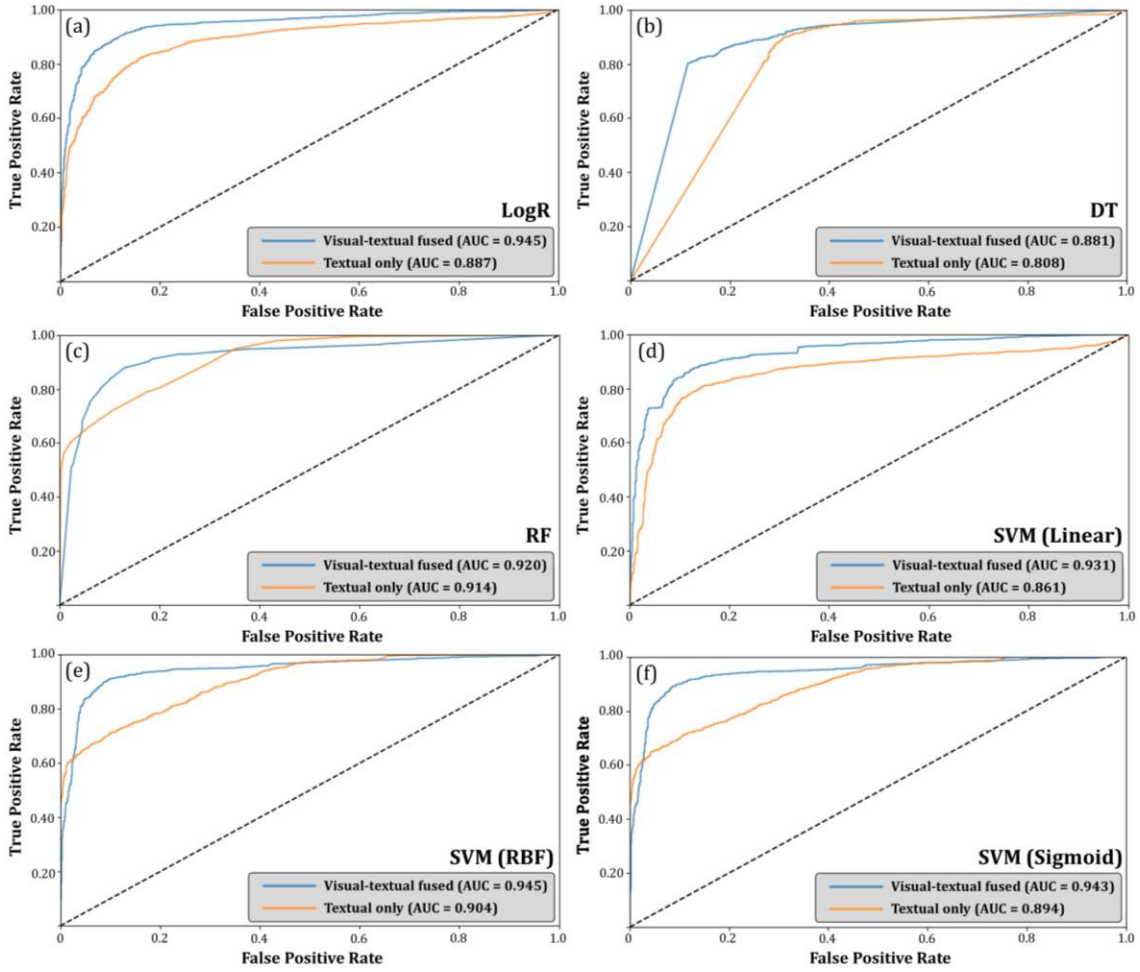


Figure 3.8 ROC curves of the six algorithms using visual-textual fused vector (Z_{fused}) and using textual vector ($Z_{textual}$) alone.

3.5.4 Uncertainties

After the evaluation of general performance, individual cases were investigated to understand the uncertainties that the fusion mechanism might cause. Figure 3.9 presents some comparisons of classification results when textual features are used and when visual-textual fused features are used. In general, when textual information and visual information of a certain post were both flood relevant, the fused feature tended to boost the probability (Figure 3.9b, Figure 3.9c, Figure 3.9e, and figure 3.9f). When textual information and visual information were contradictory, however, the probability that a fused feature

indicated tended to favor the opposite direction of that a textual feature indicated (Figure 3.9a, Figure 3.9d, Figure 3.9f, and Figure 3.9g).

In some cases, a visual-textual feature leads to the correction of wrongly classified textual information. For instance, the textual information in Figure 9a was classified as non-flood relevant (P_{flood} for textual = 0.35) due to the lack of flood relevant word vectors in its texts. When coupled with the visual information, however, its visual-textual fused feature was successfully classified as flood relevant (P_{flood} for fused = 0.82). Another example is Figure 9g, where its textual information was classified as flood relevant (P_{flood} for textual = 0.93) and its visual-textual fused feature indicated otherwise (P_{flood} for fused = 0.38). A similar example can also be found in Figure 3.9f.

During the case study, the biggest challenge in visual-textual fusion is the association between text and image a post contains. As observed in Vadicamo et al. (2017), the linkage between text content and image content is uncertain and sometimes rather weak. Moreover, it is still unclear how this linkage might change during a disaster event. Although this chapter proves that visual-textual fused feature is more robust in classifying flood tweets, the foundation of the proposed fusion mechanism still relies on the strong linkage between them, meaning that a weak linkage between texts and images could potentially cause unmeasurable uncertainties to the model. To better utilize both visual and textual information from social media, more studies are needed to understand the linkage, especially how this linkage will change during different disaster events.

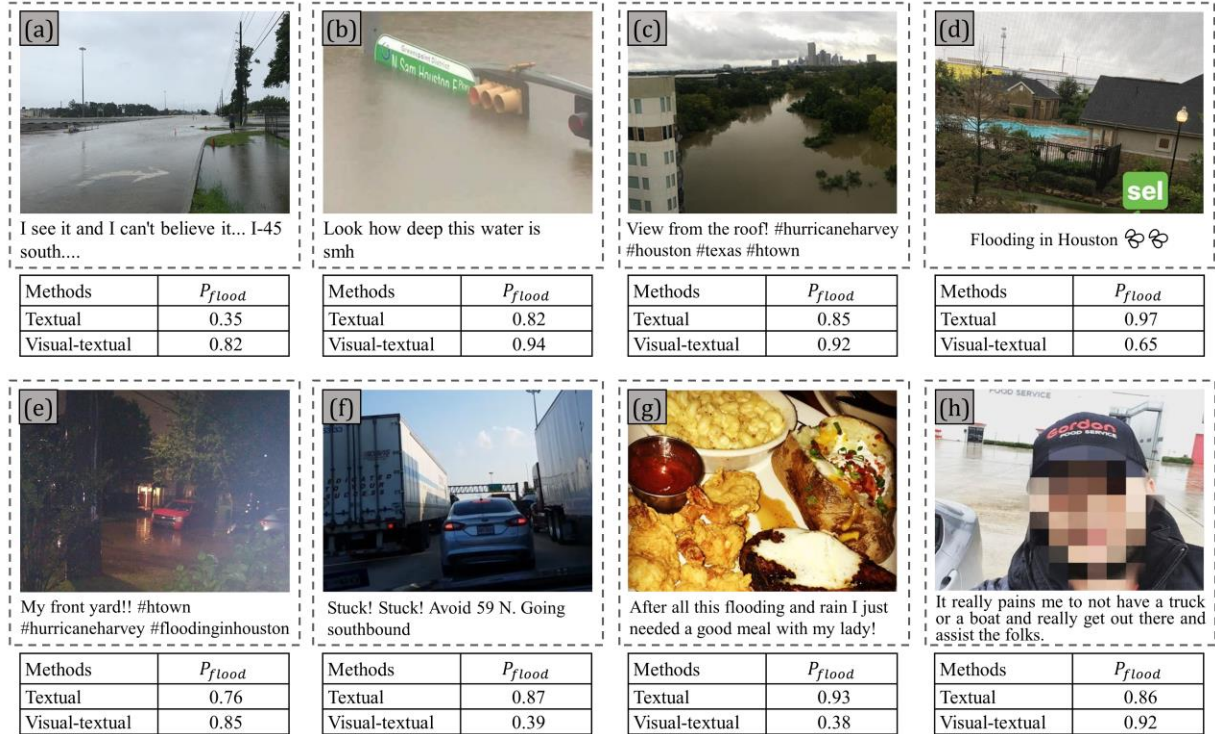


Figure 3.9 Eight Examples of classification results.

This study provides direct evidence that coupling visual and textual information aids in better classification accuracy. The fact that visual-textual representation outperforms textual representation alone demonstrates the importance of incorporating visual information into social media post labeling.

Derived in an automatic manner, the robustness of visual-textual fused classification guarantees a flood-related VGI pool with high quality. The water height information from those geotagged social media distributed in a large region could provide valuable local flooding awareness in a timely manner, significantly assisting rapid flood response by local authorities and first responders. In addition, the proposed visual-textual labeling approach can be applied to other disasters such as fire and earthquake given proper textual and visual training samples. The on-topic posts classified by their texts and pictures represent timely individual-level disaster documentation, coupling with rich spatial

contexts when geotagged. Those posts extracted in an automatic manner can be utilized to aid in a variety of disaster mitigation approaches including urban system recovery, public sentimental analysis, damage assessment, evacuation investigation, first responder dispatch, recovery management, etc.

3.6 LIMITATIONS AND FUTURE DIRECTIONS

3.6.1 Limitations

One limitation of the proposed approach is that the performance of on-topic social media retrieval is highly reliant on the quantity and quality of training samples. This being said, any deficiency in numbers or defect in quality will potentially undermine the classification result. This limitation, the necessity of large training samples with high quality, widely exists in most of the deep learning algorithms. Besides, developing such high-quality training samples in a large quantity is time- and labor-consuming. It might not be feasible to provide real-time retrieval unless all the training samples are pre-prepared.

Another limitation is the fundamental assumption of the fusion algorithm. The better performance of visual-textual features compared to textual features alone relies on a rather strong association of textual and visual content in a social media post. The study in this chapter only examined one specific social media platform (Twitter) during one specific event (flood). The strength of this linkage, however, may not hold the same for other social media platforms or for other events. Caution is advised when the proposed fusion algorithm is applied in a cross-media or cross-event manner.

Thirdly, the integration is based on a vector fusion mechanism where visual vector and textual vector are concatenated to form a visual-textual vector, participating in the final classification task. This fusion method implies equal weights on both visual and textual

information a social media post contains. In some cases, however, this assumption might not be true.

Fourthly, the study in this chapter only considers the textual content and visual content, while the spatiotemporal dimension is neglected. Study by Li et al. (2018) has proved that people who are close to the disaster location spatially tend to produce more disaster-related information on social media. More disaster-related social media are usually found when a disaster reaches its peak (Sakaki et al., 2010). The prior probability derived from the spatiotemporal information of social media could contribute to better on-topic classification accuracy.

Finally, only tweets that have been geotagged serve as training samples in this study, which inevitably cause certain biases as many studies have proved that geotagged tweets only consist of a small proportion. Sloan and Morgan (2015) reported that 96.9% of their tweeters have no geotagged tweets in the study site of the UK. Globally, Sloan et al. (2013) concluded that only 0.85% of tweets were geotagged with longitude and latitude information. The small training datasets derived from only geotagged tweets in this study potentially undermine the robustness of the proposed classification model.

3.6.2 Future directions

This study has proved that, during a flood event, the proposed visual-textual fused approach contributes to an improved on-topic retrieval accuracy by taking advantage of both textual content and visual content a tweet contains. More studies, however, are needed to test the validity of visual-textual features during other disaster events as the association between texts and pictures may not hold the same. A weak association can potentially undermine the fundamental assumption. More explorations are necessary to investigate how this

association changes in different events so that useful guidance can be given on which source is more reliable, single, or fused.

From a technical perspective, this study can be modified and improved in many ways. Firstly, this study combines the visual feature and textual feature extracted respectively from two specific architectures: Inception-V3 and word embedded CNN. With the rapid development of deep learning, however, more advanced networks have been proposed. Resnet (He et al., 2016) and Inception-V4 (Szegedy et al., 2017), for instance, have demonstrated their better image labeling capability and are widely used in many image recognition applications. Recurrent Neural Network (RNN), a neural network architecture that exhibits temporal dynamic behavior, has been proved rather efficient in handling sequential textual data (Hochreiter et al., 1997; Mikolov et al., 2010; Tai et al., 2015). The integration of the aforementioned networks potentially leads to more robust visual-textual features, consequently resulting in better disaster-related social media retrieval. In terms of the embedding method, this study used Word2Vec embedding trained from a self-designed social media corpus. Other embedding methods, including ELMo (Peters et al., 2018), FastText (Bojanowski et al., 2017), and GloVe (Pennington et al., 2014) are becoming more popular recently. Whether the word vectors derived from those embedding methods improve the proposed fusion algorithm deserves further exploration.

In addition, the spatiotemporal dimension of social media should be considered in future studies as previous studies have concluded the strong linkage between the content and spatiotemporal characteristics of social media posts. By analyzing the spatiotemporal distribution of extracted disaster-related posts, a better understanding of the relationship

between their spatiotemporal characteristics and their content can be achieved, which in turn contributes to better utilization of those characteristics in retrieving on-topic posts.

Finally, the training dataset can be expanded by using geoparsing, a process of converting text description of places to unambiguous geographic identifiers (Cheng et al., 2010; Avvenuti et al., 2018). The additional training samples rendered by geoparsing techniques contribute to the better generalization of proposal CNN architecture and largely facilitate follow-up analyses that require geo-information within social media data.

3.7 CONCLUDING REMARKS

Social media platforms have played a critical role in situation awareness and mitigation for a wide range of disasters. Bearing the enormous volume of social media posts during a disaster event, disaster-related social media posts only consist of a small proportion. An automatic approach to on-topic social media retrieval is, therefore, developed in this chapter for rapid flood awareness. Texts and pictures are two major components of a social media post that are both essential in retrieving on-topic posts. This chapter presents a visual-textual fused CNN architecture for labeling on-topic social media posts in an automatic manner. Two CNNs specifically for visual and textual information labeling, transfer-learned Inception-V3 and word embedded CNN, are adopted. A fused feature vector is then formed by concatenating the extracted visual and textual vectors, which is further utilized to retrieve the final binary labels (on-topic vs. off-topic) of the post. Taking flood as a disaster case and Twitter as the targeted social media platform, the experimental results suggest that the visual CNN and textual CNN perform remarkably well with classification accuracies of 92.92% and 93.45%, respectively. During the fused classification phrase, all selected machine learning algorithms (including LogR, DT, RF,

SVM-Linear, SVM-RBF, and SVM-Sigmoid) have confirmed the positive effect of additional visual information in classifying on-topic tweets, which are justified by the improvement of their classification accuracy and corresponding ROC curves. The visual-textual fused feature proves that an additional visual vector leads to more robustness in on-topic social media retrieval, presumably due to the self-correction of uncertainties from single-source information. Incorporating both texts and pictures in social media posts, the proposed visual-textual CNN architecture significantly automates the on-topic social media retrieval, largely expanding searching scope, ensuring more robustness of classification, and seeding a wide range of social media based disaster studies. The direct evidence in this chapter that visual-textual representation outperforms textual representation alone urges future research regarding social media labeling towards a visual-textual fusion direction.

The automated social media retrieval algorithm proposed in this chapter, together with the data fusion flood model designed in Chapter 2, greatly benefits the acquisition of improved flood awareness, thus largely facilitating rapid flood mapping. Besides improved inundation mapping of a specific flood event in a local area, flood exposure and awareness of flood risk in hurricane-prone zones also provide important information for sustainable development at a large geographic scale. Across the CONUS region, the U.S. east coast is exposed to the most frequent storms that are predominantly originated from the North Atlantic Basin (much stronger than the west coast with storms from the Eastern Pacific Basin). The following chapter (Chapter 4) explores the long-term spatiotemporal dynamics of human settlement on the U.S Atlantic/Gulf Coast that has been suffered from frequent hurricane hits.

CHAPTER 4

HURRICANE-INDUCED DISASTER EXPOSURE IN THE U.S.

ATLANTIC/GULF COASTS³

4.1 INTRODUCTION

Hurricanes threatening the conterminous United States have two primary originating sources: the North Atlantic Basin that includes the North Atlantic Ocean, the Caribbean Sea and the Gulf of Mexico; and Eastern Pacific Basin that covers Northeastern Pacific (east of 140°W and north of the equator) (Goldenberg et al., 2001). Historically, more hurricanes from the North Atlantic Basin made landfalls on the U.S territories, dramatically affecting people living in the Gulf coasts and Atlantic coasts. While the Eastern Pacific Basin originated storms occasionally visited the southwestern conterminous U.S, by the time they landed, they usually degraded to tropical cyclones due to the long travel distance and cold water in coastal California (Chenoweth and Landsea, 2004).

Atlantic hurricane season usually runs from June 1st to November 30th, during which the North Atlantic Basin exhibits significantly intensified tropical cyclone activity and gives rise to many devastating hurricanes landing the coasts. In 2016, Hurricane

³ Huang, X., Wang, C., & Lu, J. (2019c). Understanding the spatiotemporal development of human settlement in hurricane-prone areas on the US Atlantic and Gulf coasts using nighttime remote sensing. *Natural Hazards and Earth System Sciences*, 19(10), 2141-2155. Reprinted with permission from the publisher.

Mathew, a Category 5 (the highest category) hurricane, claimed a total of 34 direct deaths in the U.S. In 2017, Hurricane Harvey in the Gulf coast caused a total of 125 billion dollars of damage, ranking the second-costliest hurricanes in the U.S. In the same year, Hurricane Irma in the Atlantic coast caused a total of 50 billion dollars of damage, ranking the fifth costliest hurricanes in the U.S. In 2018, the third year in a consecutive series (2016-2018) of above-average damaging Atlantic hurricanes, there were 15 named tropical storms, eight of which became hurricanes, including two major hurricanes. Hurricane Florence, for example, as a major hurricane in 2018, caused a severe economic loss of \$22 billion to North Carolina, \$5.5 billion to South Carolina) and \$1 billion to Virginia (Krupa, 2018). The widespread storm surge and extensive floods from extreme rainfall largely crippled public infrastructures and impacted all segments of society. A noticeable increase in the number of hurricanes from the North Atlantic Basin since the late 1980s has been observed (Vecchi and Knutson, 2018). Even though it is partly due to improved monitoring (Villarini et al., 2011), the increased intensity and duration of these hazards have posed great threats to people residing in the U.S. Atlantic and Gulf Coasts (Landsea et al., 2010).

Despite these threats, the U.S. southeastern region has experienced significant population growth in recent decades. The population in Florida, North Carolina, and South Carolina, for instance, has increased by 61.2%, 43.6%, and 54.3%, respectively, since 1990 (U.S Census Bureau, 2018). The densely populated coastal areas are receiving higher threats than ever (Crosset, 2004). In these hurricane-prone areas, a better understanding of the temporal and spatial dynamics of human settlement is needed to assist damage assessment and sustainable urban planning.

Satellite observations have been widely applied in investigating urban dynamics as remote sensing provides spatially explicit information of the urbanization process. Extensive application has been made utilizing multispectral sensors that record the reflectance of ground features to categorize different land covers, thus allowing the delineation of urban extent (Xu, 2008; Zha, 2003). This type of remotely sensed imagery, however, relies on the reflective characteristics of all land objects on the ground, thus lacking the perspective on human activities. In comparison, satellite-derived nighttime light (NTL) data provides a unique and direct observation of human settlement via night lights (Ceola et al., 2014; Ceola et al., 2015). Natural land covers are distinctively dark in NTL imagery. Nighttime remote sensing has been increasingly used for analyzing socioeconomic dynamics and urbanization process at national and regional levels (Elvidge et al., 1997; Ghosh et al., 2010), thanks to their light-only sensitivity, large spatial coverage (Imhoff et al., 1997; Huang et al., 2019d), easiness to acquire (Lu et al., 2008) and consistency over a long term (Elvidge et al., 1999).

Among all the satellite-derived NTL products, the NTL data obtained by Operational Linescan System (OLS) via the U.S. Air Force Defense Meteorological Satellite Program (DMSP), hereafter referred to as DMSP/OLS NTL, is the most commonly used due to its long-time span (more details in next section). Extensive attempts have been made to harvest the NTL observations from DMSP/OLS in applications including urban expansion and decay (Lu et al., 2018), settlement dynamics (Elvidge et al., 1999; Yu et al., 2014), socioeconomic development (Doll et al., 2000) and energy consumption (Chand et al., 2009). Recent studies enhanced the NTL products by fusing DMSP/OLS NTL data with natural land cover characteristics such as the Normalized

Difference Vegetation Index (NDVI) to reduce the light saturation problem. This fusion greatly increased the potential of DMSP/OLS in discriminating against the human settlement structures (Lin et al., 2014; Liu et al., 2015). The improved DMSP/OLS NTL product serves as a valuable resource for monitoring large-coverage and long-term urbanization dynamics.

The goal of this chapter is to illustrate the usage of DMSP/OLS NTL data to monitor the urbanization process and hurricane impacts on the U.S. Atlantic and Gulf coasts using nighttime artificial lights as a proxy. Hurricane-prone areas were first derived by calculating the track density from historical storm tracks in the North Atlantic Basin. An intercalibrated DMSP/OLS NTL time series was built in a yearly interval. Assisted with the NDVI data, the Vegetation Adjusted NTL Urban Index (VANUI) was used to characterize human settlement intensity in the study area. After that, a trend analysis was conducted to identify areas with a significant increase in human settlement intensity in different zones, in which the potential hurricane impacts were statistically evaluated. The spatiotemporal changes of human settlement revealed from nighttime remote sensing in hurricane-prone zones provide valuable information to evaluate the damage and to support the decision making of urban development.

4.2 INTERCALIBRATION AND DESATURATION OF DMSP/OLS NTL SERIES

Due to the absence of on-board calibration and intercalibration, the annual DMSP/OLS NTL composites derived from multiple satellites in a span of 22 years were not comparable directly (Li and Zhou, 2017; Liu et al., 2012). This lack of continuity and comparability has posed great challenges in DMSP/OLS NTL based trend analysis (Tan, 2016). Elvidge et al. (2009) designed a three-step framework to intercalibrate the DMSP/OLS NTL

composites. Those three steps are: 1) selecting a reference region; 2) selecting a reference satellite year; 3) performing a 2nd-order polynomial regression against the NTL reference data. This simple framework has been proven efficient in reducing discrepancies in digital number (DN) values of the DMSP/OLS NTL time series (Pandey et al., 2013) and has been adopted in many studies (Liu and Leung, 2015; Huang et al., 2016).

Another notable limitation of DMSP/OLS NTL is the saturation of luminosity in the 6-bit (DN in a range of 0-63) imagery (Letu et al., 2010). To retrieve the heterogeneity in areas with high intensity of human settlement, numerous attempts have been made to mitigate the saturation effect. A commonly used vegetation index, NDVI, is a useful indicator to reduce the saturation effect in DMSP/OLS data. Its practicality has been confirmed by many studies (Zhou et al., 2014; Liu et al., 2015). Lu et al. (2008) proposed a human settlement index (HSI) by merging normalized DMSP/OLS NTL data with the maximum NDVI in growing season derived from Moderate Resolution Imaging Spectroradiometer (MODIS). HSI has been proved rather efficient for settlement mapping in several testing sites in southeastern China. Zhang et al. (2013) develop a vegetation-adjusted NTL urban index (VANUI), which captures the inverse correlation between vegetation and luminosity. This simple index efficiently reveals the heterogeneity in regions with saturated DN values, which has been recognized by Shao and Liu (2014). Following the original design of NDVI that characterizes the inverse relationship between the near-infrared band and red band in vegetation, Zhang et al. (2015) designed a normalized difference urban index (NDUI) that characterizes the inverse relationship between vegetation and luminosity in a similar way. NDUI was evaluated in five testing sites in the U.S and proved to be effective in desaturating DN values in DMSP/OLS.

In this chapter, the intercalibration of DMSP/OLS data follows the method proposed by Elvidge et al. (2009), and the desaturation of DMSP/OLS data is achieved by using VANUI (Zhang et al., 2013).

4.3 DATASETS

4.3.1 Historical storm tracks

The historical storm tracks were retrieved from International Best Track Archive for Climate Stewardship (IBTrACS) hosted by NOAA (<https://www.ncdc.noaa.gov/ibtracs/>). The IBTrACS provides a globally best track dataset by merging storm information from multiple centers into one product. As the majority of the storms around on the conterminous U.S are formed in the North Atlantic Basin (Figure 4.1), we only examined the storms from the North Atlantic Basin along the U.S. Atlantic and Gulf Coasts. A total of 655 storm tracks containing 18,929 line segments (with an attribute of wind speed) were used in this study.

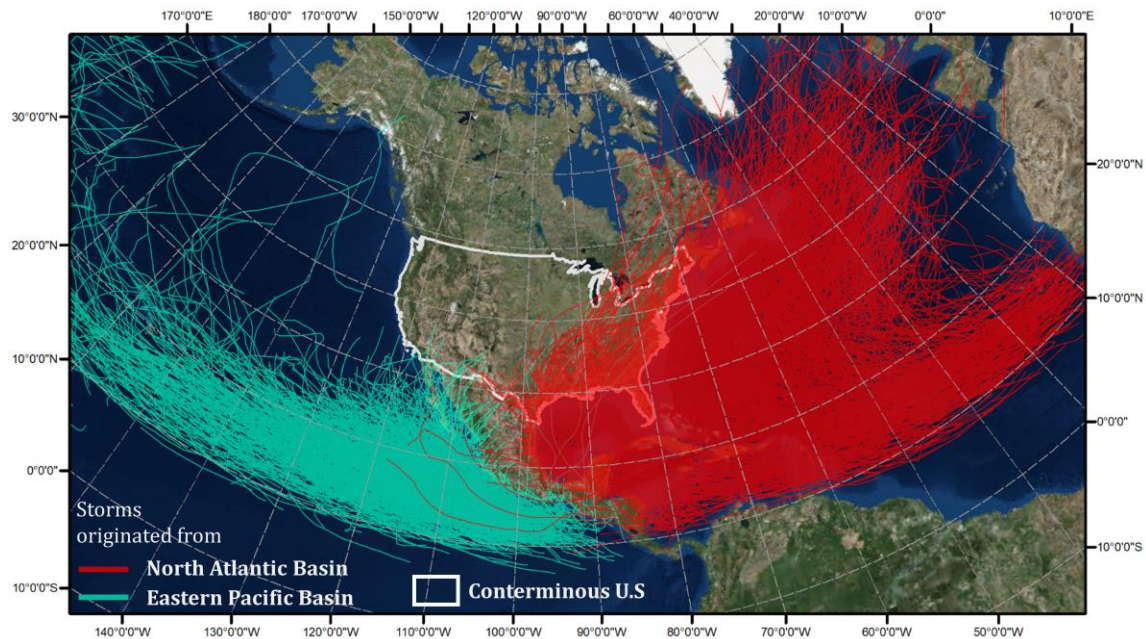


Figure 4.1 Historical storm tracks from the North Atlantic Basin (in red) and from the Eastern Pacific Basin (in green).

4.3.2 DMSP/OLS NTL series and NDVI series

The DMSP/OLS satellites are operated by U.S Air Force (USAF) and are composed of six satellites (F10, F12, F14, F15, F16, and F18) in the period of 1992-2013. With a 3,000 km orbit swath, they acquired the OLS imagery from -65° to 65° in latitude at a nominal resolution of 30 arc-second (around 1 km at the Equator) (NOAA Earth Observation Group, 2018). The temporal coverages of the six satellites are summarized in Table 4.1.

Table 4.1 DMSP/OLS Satellites and overlays in corresponding years.

Year	Satellites					
	F10	F12	F14	F15	F16	F18
1992	F101992					
1993	F101993					
1994	F101994	F121994				
1995		F121995				
1996		F121996				
1997		F121997	F141997			
1998		F121998	F141998			
1999		F121999	F141999			
2000			F142000	F152000		
2001			F142001	F152001		
2002			F142002	F152002		
2003			F142003	F152003		
2004				F152004	F162004	
2005				F152005	F162005	
2006				F152006	F162006	
2007				F152007	F162007	
2008					F162008	
2009					F162009	
2010						F182010
2011						F182011
2012						F182012
2013						F182013

Note. Bold terms indicate the years with two satellites available in a given year.

The DMSP/OLS NTL products used in this study are the version 4 Stable Lights series in a 22-year span (1992-2013). The DMSP/OLS NTL data were obtained from the National Centers for Environmental Information website (<https://ngdc.noaa.gov/eog/dmsp/>)

downloadV4composites.html). The version 4 DMSP/OLS Stable Lights product has already excluded sunlit, glare, moonlit, cloud coverage, and lighting. Ephemeral events such as wildfires also have been discarded. In this study, one composite each year in the conterminous U.S was produced from each satellite. When two satellites were available in certain years, a combined composite in this year was derived using the method described in Section 4.4.2. All DMSP/OLS NTL images were resampled to the 1 km pixel size.

In the same period of 1992-2013, the NDVI products in the conterminous U.S from two satellite sensors were used in this study: Advanced Very High Resolution Radiometer (AVHRR) and Moderate Resolution Imaging Spectroradiometer (MODIS). NDVI series from AVHRR and MODIS span from 1992-2005 and 2003-2013, respectively. These two products were further calibrated in three overlaying years: 2003, 2004, and 2005 to increase data comparability. AVHRR NDVI series is the annual maximum value composite (MVC) with 1 km pixel size, provided by United States Geological Survey Earth Resources Observation and Science (USGS/EROS) (https://phenology.cr.usgs.gov/get_data_1km.php). A number of preprocessing steps have been performed in this product to remove noises, which includes removal of spurious spikes, temporal smoothing, and interpolation. MODIS NDVI series was derived from Oak Ridge National Laboratory Distributed Active Archive Center (ORNL DAAC) (<https://daac.ornl.gov/>). The data were generated from Terra MOD13Q1 and Aqua MYD13Q1 products and have been smoothed and gap-filled with 250 m spatial resolution (Spruce et al., 2016). To be comparable with AVHRR NDVI, the annual MVC product a from the MODIS NDVI series by selecting the maximum NDVI value in each year. It was also resampled to 1 km pixel size. Water bodies contained in both datasets were masked out using MODIS MOD44W product.

4.4 METHODS

4.4.1 Delineation of hurricane-prone zones

The delineation of hurricane-prone zones is based on the retrieved 655 storms from the North Atlantic Basin landed on the conterminous U.S. An area with higher hits of historical storms is expected to be more hurricane-prone. We also assume a generally positive relationship between wind intensity of a storm and its impact. At a given location (i,j) , a circular neighborhood (R) , centered at this location was assigned. For all line segments of storm tracks falling in this neighborhood, the storm track density was calculated as a line density of all segments weighted by their wind speeds:

$$\rho_{i,j} = \sum_{r \in R} L_{i,j}^r \times W_{i,j}^r, \quad (4.1)$$

where $\rho_{i,j}$ denotes the weighted line density at the location (i,j) . $L_{i,j}^r$ and $W_{i,j}^r$ denote the length of a line segment r and corresponding wind speed, respectively. The radius of R is set as 100 km in this study.

The storm track density was then normalized to a range of $[0,1]$, with a higher value indicating higher hurricane proneness. To simplify the process for zonal analysis, we categorized the normalized storm track density into four zones from low to high hurricane proneness: Zone 4 (0-0.2), Zone 3 (0.2-0.5), Zone 2 (0.5-0.7) and Zone 1 (0.7-1.0).

4.4.2 Intercalibration (DMSP/OLS NTL series; NDVI series) and VANUI calculation

The procedure from Elvidge et al. (2009) was adopted to intercalibrate the DMSP/OLS NTL time series. Serving as the reference site (Figure 4.3a), the geographic area of metropolitan Los Angeles and City of San Diego, CA maintains high conformity of NTL values throughout the 22-year period (Kyba et al., 2017; Hsu et al., 2015), which satisfies

the “pseudo-invariant” rule for calibration site selection (Elvidge et al., 2009). The year 2007 (satellite F16) has been commonly selected as the reference year in many studies (Yi et al., 2014; Ma et al., 2014). Therefore, we extracted the DMSP/OLS NTL data this year at the same site as the reference. With all lit pixels ($DN > 0$) in the reference site, a second-order regression model was performed to calibrate the NTL data in each year:

$$DN_{n,cal} = c + b \times DN_n + a \times DN_n^2, \quad (4.2)$$

where $DN_{n,cal}$ is the calibrated DN value in year n , DN_n is the original DN value in year n and a, b and c are the coefficients. The non-lit pixels ($DN=0$) are not calibrated.

As shown in Table 4.1, two DMSP/OLS NTL data layers are available in overlapping years. For lit pixels ($DN > 0$ in both years), the calibrated DN values in this year are calculated as the average of two calibrated data sets. The value of a pixel remains 0 if its original DN value in any year is 0. Finally, the calibrated DMSP/OLS NTL images were normalized (DN_{nor}) to $[0,1]$.

Similarly, the annual maximal NDVI ($NDVI^{MVC}$) products from AVHRR ($NDVI_{AVHRR}^{MVC}$ from 1992 to 2005) and MODIS ($NDVI_{MODIS}^{MVC}$ from 2003 to 2013) were intercalibrated to maintain the continuity and comparability in $NDVI^{MVC}$ annual series. Stratified sampling was applied to pixels with NDVI value above 0.1 to ensure that land covers in different NDVI ranges were equally sampled. Thirty thousand samples were collected within four hurricane-prone zones in the years 2003, 2004, and 2005, respectively. It has been reported that MODIS maintains higher spectral sensitivity than AVHRR (Tucker et al., 2005).

Here, a linear regression was applied to correct AVHRR $NDVI^{MVC}$ to MODIS $NDVI^{MVC}$:

$$NDVI_{MODIS}^{MVC} = \alpha \times NDVI_{AVHRR}^{MVC} + \beta, \quad (4.3)$$

where α and β are regression coefficients.

The calibrated $NDVI_{AVHRR}^{MVC}$ series from 1992-2002 was merged with $NDVI_{MODIS}^{MVC}$ from 2003-2013 to form a 22-year NDVI MVC series ($NDVI_{cal}^{MVC}$). Negative NDVI values are usually associated with non-living environments such as water bodies and NDVI values above 1 are not meaningful. Therefore, we limited all NDVI values in the $NDVI_{cal}^{MVC}$ series to a range of 0 to 1.

Finally, with the normalized DMSP/OLS NTL and the calibrated NDVI data series, the VANUI series was extracted (Zhang et al. 2013):

$$VANUI = (1 - NDVI_{cal}^{MVC}) \times DN_{nor}, \quad (4.4)$$

where DN_{nor} denotes the normalized DMSP/OLS NTL value and $NDVI_{cal}^{MVC}$ denotes the calibrated $NDVI^{MVC}$ value. The VANUI has a range of [0,1]. In general, a higher proportion of human settlements in a pixel leads to higher NTL and lower NDVI, both contributing to a higher VANUI. Therefore, the VANUI serves as a proxy of the intensity of human settlement.

4.4.3 Trend analysis of human settlement

The VANUI series in a 22-year span shed light on the spatiotemporal development of the human settlement. We performed the trend analysis by applying the Mann-Kendall test (Mann, 1945) coupled with the Theil-Sen slope estimator (Sen, 1968). The Mann-Kendall test statistically assesses if there is a significant monotonic upward or downward trend in the time series. Given the 22-year VANUI series, the Mann-Kendall test first computes S statistics (Mann, 1945):

$$S = \sum_{k=1}^{n-1} \sum_{j=k+1}^n \text{sgn}(x_j - x_k) \quad (4.5)$$

where n denotes the total number of observations (22 in this study) in a series, x_j and x_k are the data values at different points, i.e., the VANUI in different years in this study. $\text{sgn}(x_j - x_k)$ denotes an indicator that takes on the values 1, 0, or -1 respectively according to the signs of $(x_j - x_k)$. The variance of S (Var_S) is further computed as:

$$Var_S = \frac{1}{18} \left[n(n-1)(2n+5) - \sum_{p=1}^g t_p(t_p-1)(2t_p+5) \right] \quad (4.6)$$

where g denotes the number of tied groups and t_p denotes the number of observations in the p th group. Finally, a Z value is calculated as:

$$Z = \begin{cases} \frac{S-1}{\sqrt{Var_S}}, & S > 0 \\ 0, & S = 0 \\ \frac{S+1}{\sqrt{Var_S}}, & S < 0 \end{cases} \quad (4.7)$$

The Z value in Equation 4.7 represents the monotonic tendency of a time series. A positive Z indicates an increasing trend, while a negative Z indicates a decreasing one. A stable trend exists when the value of Z equals 0. The absolute value of Z indicates the intensity of the trend.

The significance of Z was further examined through a two-tail test with a significance level $\alpha = 0.05$. If a significant trend exists, the Theil-Sen slope estimator was further applied to estimate its slope. As a non-parametric indicator, it has low sensitiveness to outliers and high robustness in short-term series and has been widely applied in remote

sensing fields (de Jong et al., 2011; Fernandes and Leblanc, 2005). Given a VANUI time series, the slope at any point i (Q_i) can be calculated as:

$$Q_i = \frac{x_j - x_k}{j - k}, i = 1, 2, 3, \dots, N, j > k \quad (4.8)$$

The Theil-Sen slope (Q_{med}) is the median of all Q_i values in the time series. It indicates the steepness (change rate) of a certain trend. Therefore, pixels with high Q_{med} values represent a rapid increase in human settlement intensity during the investigated time period.

With the 22-year VANUI image series, clusters of geographic areas in the study region with a significant increase of human settlement were extracted. The summed slope per unit in a cluster represented the rapidness of human settlement growth in the 22 years. The spatiotemporal patterns of this growth in different hurricane-prone zones were finally analyzed.

4.5 RESULTS AND DISCUSSION

4.5.1 Hurricane-prone zones

The 655 storms from the North Atlantic Basin landed on the conterminous U.S (mostly along Atlantic and Gulf coasts) are presented in Figure 4.2a. The derived wind speed-weighted track density in the study area is presented in Figure 4.2b. Based on the density levels, we divided the track density map into four hurricane-prone zones that represent different levels of hurricane impacts: the highest impacts in Zone 1 and lowest in Zone4. The study area contains all U.S. states covered in the hurricane-prone zones (Figure 4.2c): Maine, Massachusetts, New Jersey, New York, North Carolina, New Hampshire, Pennsylvania, Rhode Island, Tennessee, Texas, Maryland, Alabama, Arkansas, Connecticut, Delaware, DC, Florida, Georgia, Kentucky, Louisiana, Mississippi, South

Carolina, Vermont, Virginia, and West Virginia. Some of these states, such as Florida, Texas, and North Carolina are well recognized as fast-growing in both population and economy in recent years (Milesi et al., 2003; Klotzbach et al., 2018), leading to higher threats and recovery costs from hurricanes.

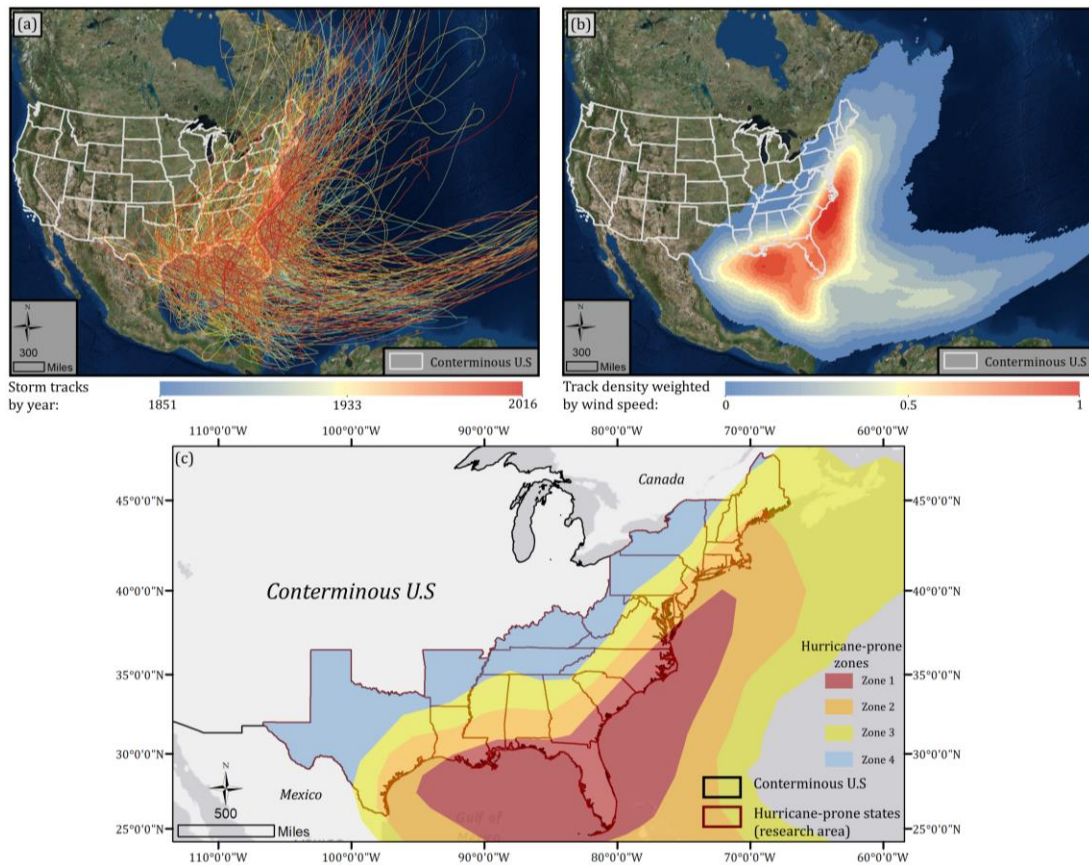


Figure 4.2 (a) Historical storm tracks from the North Atlantic Basin; (b) Normalized storm track density weighted by wind speed; (c) Hurricane-prone zones.

4.5.2 Intercalibration results of DMSP/OLS NTL series and NDVI series

The reference site for intercalibration is composed of an urban stripe from Los Angeles to San Diego, CA, in the southwest end of the United States (Figure 4.3a). Agreeing with Elvidge et al. (2009), the histograms of all NTL images in this area exhibit a sharp, bimodal distribution (urban vs. non-urban) with limited temporal variations. This confirms that it is a valid reference site for the intercalibration of NTL images. Among the three example

scatterplots between the NTL data in three years and the F162007 reference, the F162006 data show the highest agreement with the reference as they were acquired by the same satellite (Figure 4.3 (b1)). The F101992 data (Figure 4.3 (b2)) exhibit less agreement due to its different satellite origin and a long time interval from 2007. However, an R^2 of 0.949 still warrants a decent agreement for calibration. Figure 4.3 (b3) demonstrates the necessity of a second-order regression instead of a linear one. The regression equations and intercalibration coefficients for all years are listed in Table 4.2.

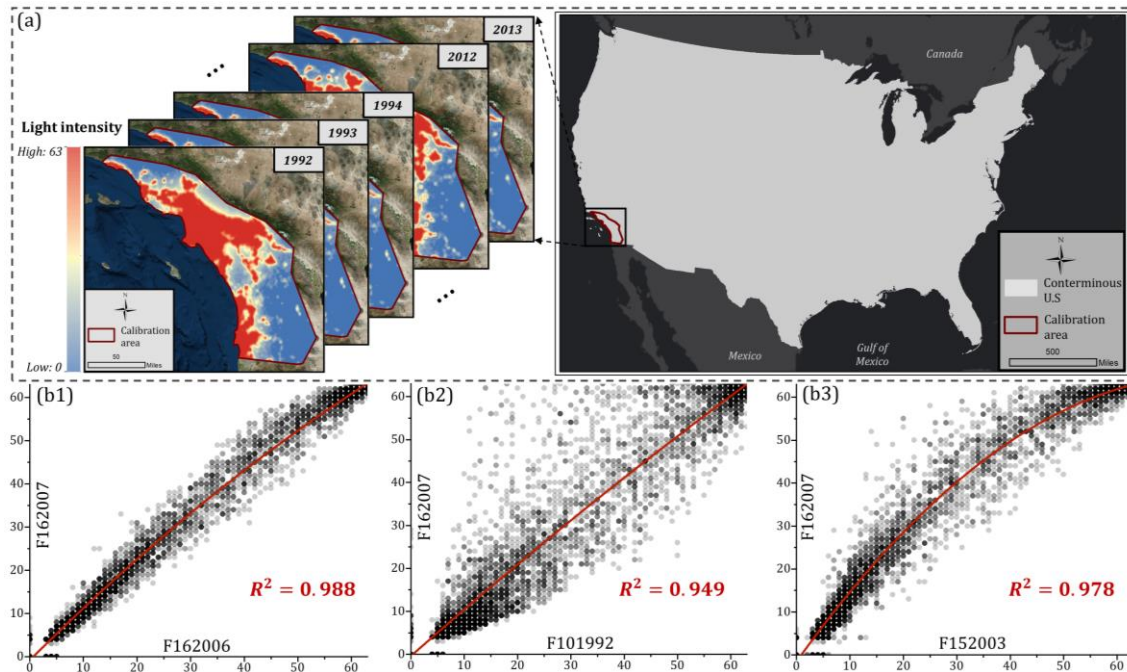


Figure 4.3 (a) DMSP/OLS NTL intercalibration in L.A. metropolitan and City of San Diego; (b1) Correlation between F162006 and reference year F162007; (b2) Correlation between F101992 and reference year F162007; (b3) Correlation between F152003 and reference year F162007.

Table 4.2 DMSP/OLS NTL intercalibration coefficients.

Satellite	Year	c	b	a	R^2
F10	1992	-0.3712	1.0953	-0.0015	0.949
F10	1993	-1.4938	1.4753	-0.0072	0.955
F10	1994	-0.9394	1.4923	-0.0077	0.951
F12	1994	-0.0430	1.2057	-0.0033	0.954
F12	1995	-0.6145	1.2354	-0.0037	0.955
F12	1996	-0.3298	1.2840	-0.0045	0.945

F12	1997	0.0253	1.1669	-0.0029	0.934
F12	1998	0.2550	1.0688	-0.0013	0.949
F12	1999	-0.3859	0.9984	-0.0001	0.967
F14	1997	0.1852	1.5516	-0.0090	0.936
F14	1998	-0.1074	1.4379	-0.0071	0.959
F14	1999	-0.5429	1.4508	-0.0070	0.967
F14	2000	-0.4461	1.3396	-0.0053	0.969
F14	2001	-0.2633	1.4454	-0.0071	0.974
F14	2002	0.3598	1.3926	-0.0065	0.961
F14	2003	-0.0390	1.3677	-0.0059	0.979
F15	2000	-1.0303	1.1837	-0.0027	0.967
F15	2001	-0.8264	1.1821	-0.0027	0.977
F15	2002	-0.6087	1.1485	-0.0022	0.981
F15	2003	-1.2553	1.6417	-0.0099	0.978
F15	2004	-0.6269	1.6067	-0.0095	0.981
F15	2005	-0.8131	1.5621	-0.0086	0.980
F15	2006	-0.4824	1.3515	-0.0054	0.989
F15	2007	-0.4583	1.4299	-0.0066	0.983
F16	2004	-0.0440	1.3285	-0.0053	0.968
F16	2005	-1.0392	1.5749	-0.0088	0.986
F16	2006	-0.6923	1.2201	-0.0033	0.988
F16	2007	0.0000	1.0000	0.0000	1.000
F16	2008	-0.0982	0.9931	0.0002	0.989
F16	2009	-0.1023	1.1478	-0.0024	0.979
F18	2010	0.1369	0.7924	0.0030	0.972
F18	2011	0.0081	1.0310	-0.0006	0.980
F18	2012	0.5943	0.8498	0.0021	0.988
F18	2013	0.5167	0.8549	0.0021	0.991

Note. Bold indicates the reference satellite in 2007.

The inter-calibration of $NDVI^{MVC}$ in the three overlaying years is shown in Figure 4.4a (AVHRR) and Figure 4.4b (MODIS). Via visual interpretation, the MODIS product has higher peak NDVI than AVHRR. The regression shows a linear relationship between the two $NDVI^{MVC}$ products ($R^2 = 0.934$) with $\alpha = 1.1835$ and $\beta = -0.1037$ (Figure 4.4c). The histograms (Figure 4.4d) demonstrate that the calibration process has shifted the AVHRR histogram to the right, making it more comparable with MODIS.

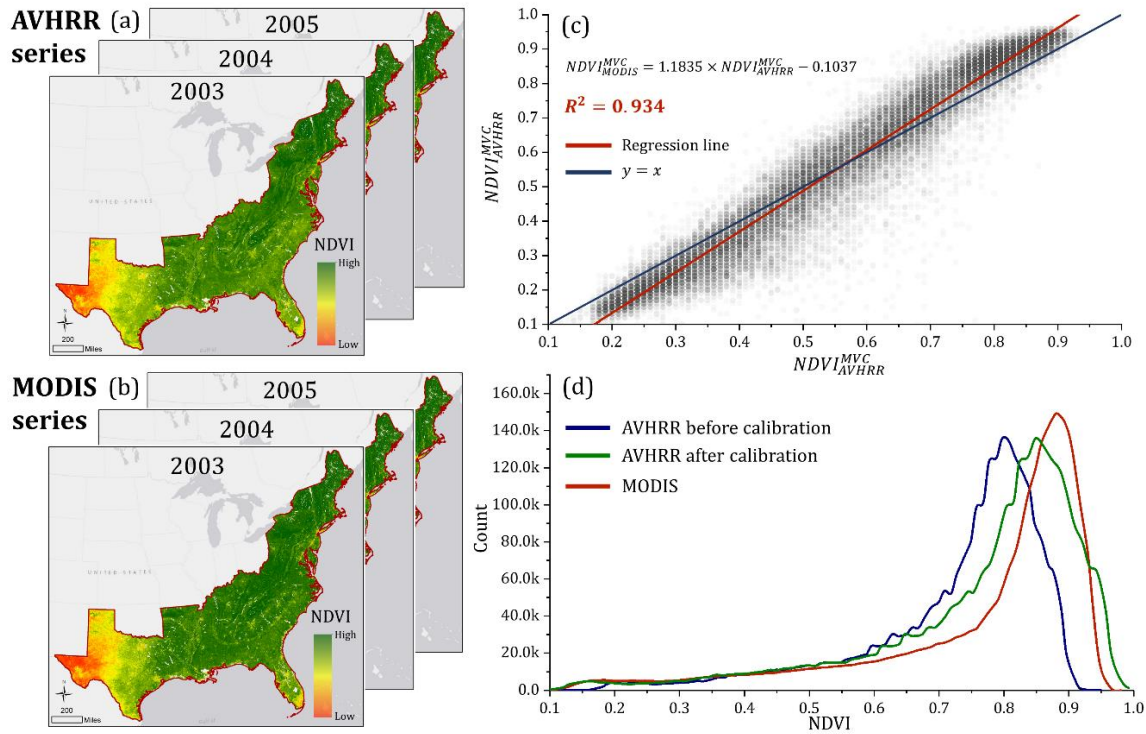


Figure 4.4 (a) $NDVI^{MVC}$ series from AVHRR in the overlaying years; (b) $NDVI^{MVC}$ series from MODIS in the overlaying years; (c) linear regression between AVHRR and MODIS using stratified sampling; (d) comparison of histograms between MODIS and AVHRR.

4.5.3 The VANUI time series

An example VANUI map (1992) for the entire study area is shown in Figure 4.5a, in which red color represents high VANUI value (high human settlement intensity), while blue color means the opposite. Several subsets of the VANUI maps in years 1992, 2002, and 2013 are displayed to demonstrate more details in densely populated urban clusters: Philadelphia (Figure 4.5b), Charlotte (Figure 4.5c), Atlanta (Figure 4.5d), Houston (Figure 4.5e) and Orlando (Figure 4.5f). Interestingly, the city of Philadelphia (Figure 4.5b) experienced a slightly decreased human settlement intensity, especially in the 1992-2002 period. This observation agrees with the population dynamics of Philadelphia in the past decades: 1990-2000 (-4.3%), 2000-2010 (+0.6%). Similar trends of population decrease have been

observed in other big northeastern cities such as Pittsburgh, in which its population dramatically decrease by -9.5% during 1990-2000 and -8.6% during 2000-2010 (U.S Census Bureau, 2018). The population loss is also recorded in a large number of small cities in the northeast region, including Johnstown and Rochester in NY, Weirton in WV, and Harrisburg in PA (U.S Census Bureau, 2018).

Oppositely, the southern and southeastern cities have experienced intensified human settlements characterized by expanded city perimeters and intensified urban cores. Houston (Figure 4.5e), for instance, has dramatically increased its human settlement. Again, this observation is well supported by the population boost per the census records, with an increasing rate of 19.8% in 1990-2000 and 7.5% in 2000-2010. Other cities, including Charlotte (Figure 4.5c), Atlanta (Figure 4.5d), and Orlando (Figure 4.5f), also have seen significantly intensified human settlement supported by their increasing population records. In general, the opposite trends of human settlement between north and south of the study area match well with the “Snow Belt-to-Sun Belt” population shift trend documented in past studies in the last decades (Hogan, 1987; Iceland et al., 2013).

It could be noted that the VANUI maps in 2013 provide much finer details than those in 1992 and 2002. Given the unaltered spatial resolution of DMSP/OLS sensors, it can be explained by the different resolutions of the raw NDVI products from AVHRR (1km) and MODIS (250m). Although images have been resampled to the same pixel size (1km) and carefully calibrated in their time series, the intrinsic sensitivity of those two sensors still affects the VANUI outputs.

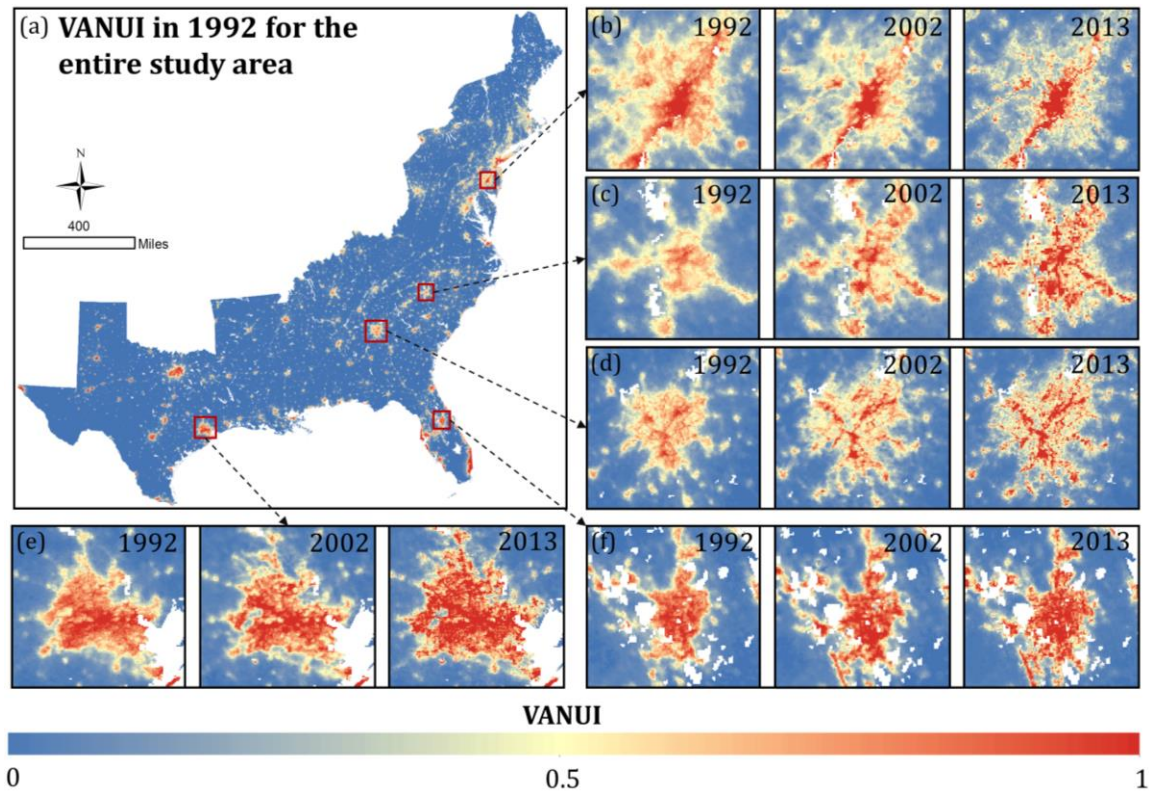


Figure 4.5 The VANUI distribution in the study area in 1992 (a); The subfigures demonstrate the VANUI variations in 1992, 2002, and 2013 in five selected urban cities: Philadelphia (b), Charlotte (c), Atlanta (d), Houston (e), and Orlando (f).

4.5.4 Spatiotemporal patterns of human settlement and hurricane impacts

In each hurricane-prone zone, the yearly percentage lit pixels ($VANUI > 0$) sheds light on land development yearly, leading to a better understanding of the process of human settlement facing different degrees of hurricane impacts. The inter-annual fluctuation of total lit-pixel numbers exists in all zones, presumably due to the uncertainties introduced from the calibration of the DMSP/OLS NTL series and NDVI series. Bearing these noises, Figure 4.6 presents the general trends of the lit pixel percentage in each zone. The lit pixel percentage varies in different zones, revealing a rank of Zone 1 (48.5%) followed by Zone 2 (45.4%), Zone 3 (41.6%), and Zone 4 (31.6%). Urban development was favored and prioritized in coastal regions, which were also the zones facing higher hurricane impacts.

As Figure 4.6a (Zone 1) and Figure 4.6b (Zone 2) suggest, the extent of human settlement in both zones increased significantly from 1992 to 2013, indicating consecutive land development in these highly hurricane-prone zones. The trends in both zones follow a logarithmic relationship that increased sharply in earlier years then slowed down. Located on the frontmost land-sea border, Zone 1 receives the most frequent and intense hurricane hits, yet its degree of fitness (coefficient of determination $R^2 = 0.898$) was higher than that of Zone 2 ($R^2 = 0.791$) in logarithmic regressions. With increased land development, we can conclude that the hurricane impacts on human settlement in these two zones are becoming more severe due to their higher hurricane-exposure. Zone 3 and Zone 4 are located further away from the coastal front. Although a slight increase in pixel percentage could be visually observed for Zone 3 (Figure 4.6c) and Zone 4 (Figure 4.6d), their logarithmic trends are not statistically significant at confidence level $\alpha = 0.05$, therefore, the regression lines are not marked in these figures. Fig.6 reveals a more significant increase in human settlement in areas closer to the coast front than inland during the 22-year period. The finding coincides with current literature in which studies reported the ever-growing population in coastal counties since the 1990s (Crosset, 2004; Stewart et al., 2003).

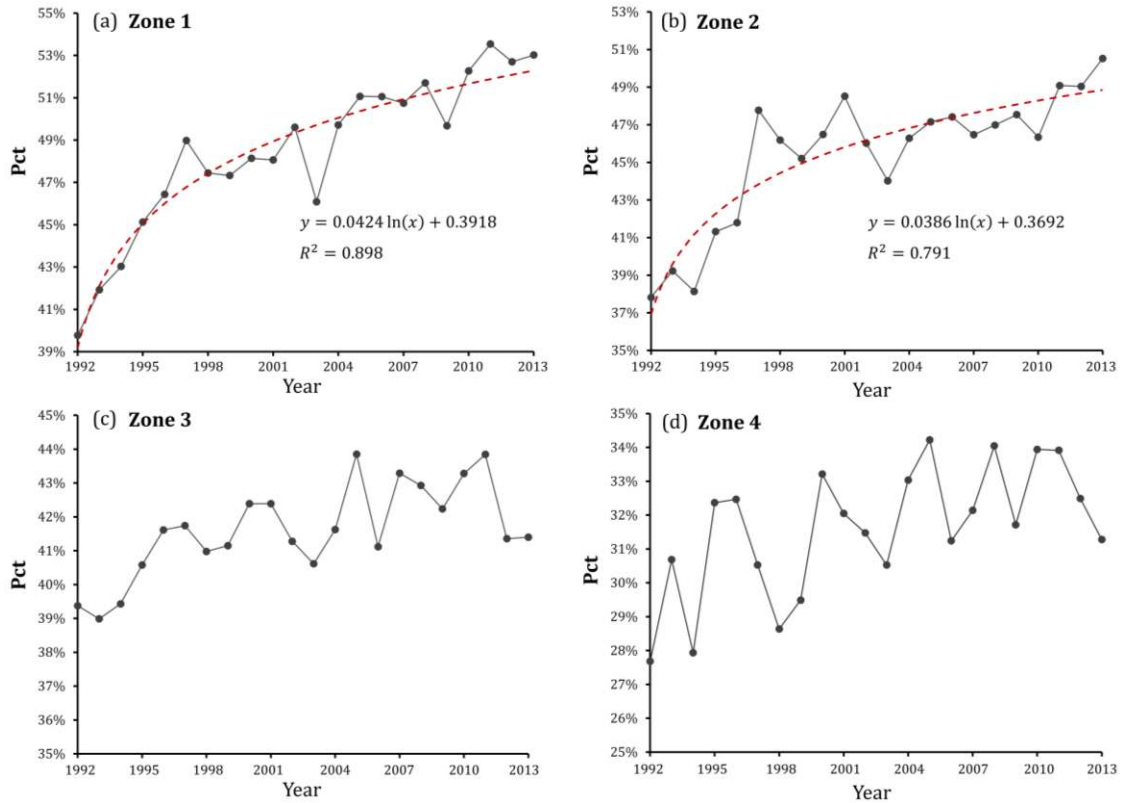


Figure 4.6 Yearly statistics of percent area with VANUI larger than 0 in Zone 1 (a), Zone 2 (b), Zone 3 (c), and Zone 4 (d).

The Mann-Kendall trend test, coupled with Theil-Sen slope estimator, extracted the areas with significant change (increase or decrease) of human settlement in the 22-year period (Figure 4.7). Zonal statistics were also summarized for the four hurricane-prone zones (Table 4.3). The net increase area is defined as the area difference between pixels with a significant increasing and decreasing trend. The net increase zonal percentage represents the percentage of net increase area in each predefined hurricane-prone zone. As Table 4.3 suggests, 4.22% of the area in Zone 1 experienced a significant increase in human settlement, followed by 2.34% in Zone 2, 2.08% in Zone 3, and 1.65% in Zone 4. The statistics above suggest a noticeably positive relationship between the hurricane proneness of each zone and the percent area with a significant increase in settlement. The sum of Theil-Sen slope, on the other hand, established the relationship between hurricane

proneness and the increase rate of settlement in each zone. Zone 1 receives the most hurricane hits but has the strongest increase of settlement intensity, followed by Zone 2, Zone 3, and Zone 4.

Table 4.3 Hurricane-prone zonal summary of Mann-Kendall and Theil-Sen test.

Hurricane-prone zones	Zone size (km^2)	Net increase area (km^2) ^a	Net increase zonal percentage (%)	Sum of Theil-Sen slope (per 100,000 km^2)
Zone 1	312,453	13,178	4.22	9.02
Zone 2	507,285	11,889	2.34	6.11
Zone 3	620,108	12,907	2.08	5.42
Zone 4	1,047,424	17,255	1.65	4.16
study area	2,487,270	55,229	2.22	5.48

^aNet increase area in each hurricane-prone zone denotes the area difference in this zone between pixels with significant increasing trend and pixels with a significant decreasing trend in their VANUI series.

Figure 4.7a demonstrates the Mann-Kendall trend map in the study area where red, blue, and yellow in the figure represent pixel with a significant increasing trend, a significant decreasing trend, and an insignificant trend, respectively. Urban expansion of major cities in the south (the U.S. Southeast region), for example, Atlanta, Houston, and Dallas, can be clearly observed as their city cores are surrounded by extensive areas with a significant increasing trend. A decrease in human settlement intensity was observed mostly in the north (the U.S. Northeast region; blue ellipse in Figure 4.7a), where several cities in the state of New York stand out, including Albany, Troy, and Johnstown.

Two city clusters were selected to demonstrate the spatial distributions of the Mann-Kendall trend and Theil-Sen slope: Metro Atlanta, Georgia (Figure 4.7 (b1) – (b2)), and Metro Dallas, Texas (Figure 4.7 (c1) – (c2)). For both cities, urban areas in 1992 were extracted from the Enhanced National Land Cover Data 1992 (NLCDe 92) released by

U.S. Geological Survey (USGS) (<https://water.usgs.gov/GIS/metadata/usgswrd/XML/nlcde92.xml>), in which all classes including low intensity residential; high intensity residential; commercial/industrial/transportation and forest residential were counted as urban areas. Significant urban expansion can be observed for both cities but with different spatial patterns. Metro Atlanta expanded in a ring form while Metro Dallas expanded in all directions except the southwest. The growth of human settlement was also observed for small towns surrounding urban clusters.

For areas with a significant Mann-Kendall trend, the Theil-Sen slope indicates the change rate of human settlement (either upwards or downwards). In Figure 4.7 (b2) and Figure 4.7 (c2), the development of Metro Atlanta and Metro Dallas followed obvious radial patterns: areas close to the urban core showing a high increase rate of settlement (higher Theil-Sen slope) while areas away from urban core showing low increase rate. Since the VANUI has been normalized to [0,1] and the temporal period covers 22 years (1992-2013), a pixel would have a Theil-Sen slope of 0.045 (1/22), under the assumption that its settlement intensity had steadily increased from 0 in 1992 to 1 in 2013. The maximum Theil-Sen slope reached 0.037 in both cities, indicating a significant boost of human settlement intensity during the investigated period.

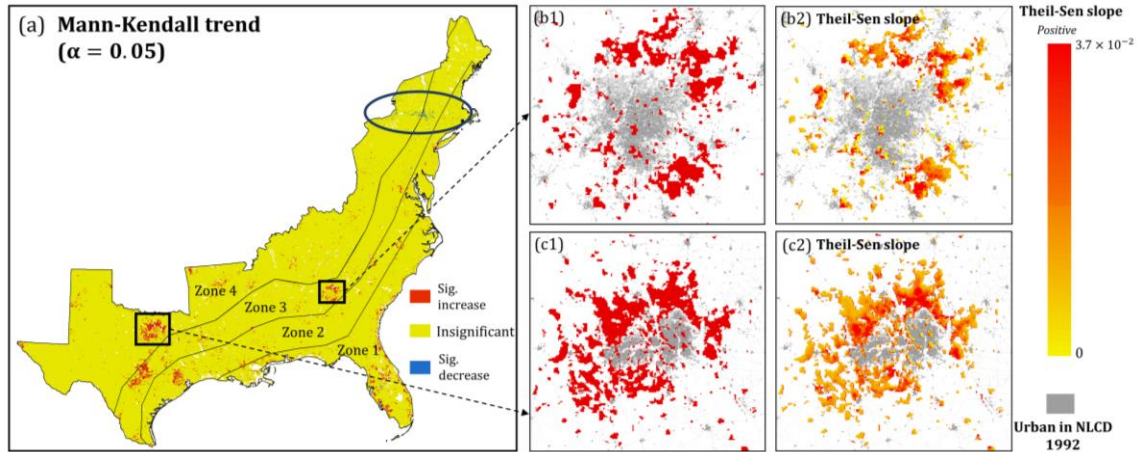


Figure 4.7 Maps of the 22-year Mann-Kendall trend and Theil-Sen slope in the study area.

Metropolitan Statistical Areas (MSA) in the study area were selected for further analysis. Defined by the U.S Office of Management and Budget (OMB), MSA represents a contiguous area of relatively high population density. From a total of 383 predefined MSAs in the study area, the top 5 most populated MSAs in each part were selected. The lit pixel counts within the administrative boundary of each MSA in 1992, 2002, and 2013 were extracted. As Table 4.4 suggests, all selected MSAs in the north have decreased settlement intensities in two temporal periods (1992-2002 and 2002-2013). The only exception is the Washington-Arlington-Alexandria MSA in 2002-2013, during which its settlement intensity slightly increased by 2.5%. On the contrary, all of the top 5 most populated MSAs in the south witnessed a significant increase in settlement intensity. MSA of Dallas-Fort Worth-Arlington, for instance, has experienced a 23.8% increase of settlement intensity in 1992-2002 and the increase rate has slowed down to 4.6% in the next period (2002-2013). MSA of Miami-Fort Lauderdale-West Palm Beach, however, is believed to have a continuous boost of human settlement as its sum of VANUI has increased 12.6% in 1992-2002 and 11.3% in 2002-2013. Although four out of the five

biggest MSAs in the south saw reduced growth rate in 2002 -2013 period (Table 4.4), Frey (2016) pointed that southern metropolitans have picked up their population increasing rate since 2015 and this could be a sign that southern metropolitans are heading back to the growth levels they experienced prior to the U.S recession in 2007 to 2009.

Table 4.4 Sum of VANUI value and change percentage in the top 5 most populated MSAs in the north and south of the study area.

MSAs ^a	Sum of VANUI in 1992	Sum of VANUI in 2002	Sum of VANUI in 2013	% change (1992-2002)	% of change (2002-2013)
<i>North</i>					
New York-Newark-Jersey City	3744.0	3307.2	3217.2	-11.67%	-2.7%
Washington-Arlington-Alexandria	1673.5	1611.4	1651.6	-3.7%	+2.5%
Philadelphia-Camden-Wilmington	2279.2	2068.1	1928.5	-9.3%	-6.8%
Boston-Cambridge-Newton	1498.9	1289.4	1182.3	-14.0%	-8.3%
Baltimore-Columbia-Towson	1035.5	961.2	831.2	-7.2%	-13.5%
<i>South</i>					
Dallas-Fort Worth-Arlington	3115.4	3857.1	4034.12	+23.8%	+4.6%
Houston-The Woodlands-Sugar Land	2687.0	3028.8	3143.9	+12.7%	+3.8%
Miami-Fort Lauderdale-West Palm Beach	1985.4	2262.7	2518.9	+12.6%	+11.3%
Atlanta-Sandy Spring-Roswell	2085.8	2398.8	2546.2	+14.0%	+6.1%
Tampa-St. Petersburg-Clearwater	1387.7	1511.9	1598.8	+9.0%	+5.7%

^aAll administrative boundaries of selected MSAs were derived from U.S Census Bureau: https://www.census.gov/geo/maps/data/data/cbf/cbf_msa.html. MSAs in the south were selected from Southeast and Gulf South of the U.S and therefore,

Washington-Arlington-Alexandria and Baltimore-Columbia-Towson were regarded as north MSAs in this study.

The ongoing intensification on human settlement in high hurricane-exposure areas, especially in the U.S. southeastern region, potentially leads to the escalation in flood-induced losses. Despite the fact that the driving factors are complex and unclear, they reflect the micro to macro levels of socioeconomic development that has been prioritized in high hurricane-exposure areas in the last decades. Additionally, intensification of human settlement always couples with anthropogenic environmental changes (deforestation, wetland destruction, etc.), potentially resulting in more severe impacts during hurricanes and floods (Viero et al., 2019). Although the investigated period of this study stops at the year 2013 due to the termination of DMSP/OLS satellites, intensification of human settlement in areas with high hurricane-exposure (like Zone 1) is expected to continue and might even accelerate. In alignment with economic recovery, studies have shown escalated population shift towards the Atlantic and Gulf coast, after the stalling during the recession (Neumann et al., 2015).

Coastal resilience becomes more complicated when the increasing pressure of human settlement in coastal zones is coupled with the more frequent and costly hurricanes. The last three years (2016-2018) have seen consecutive above-average damaging Atlantic hurricane seasons. The economic damage in the conterminous U.S in 2017 was among the costliest ever recorded on a nominal, inflation-adjusted, and normalized basis (Klotzbach, 2018). What's worse, 2018 was the most recent hurricane season to feature four simultaneously named storms (Florence, Isaac, Helene, and Joyce) after 2008. Although the future trend of hurricane seasons cannot be easily predicted, the implication of greater

losses stands as the sizable growth of human settlement continues along the Atlantic and Gulf coasts.

With the launch of the Suomi National Polar-orbiting Partnership (NPP) Satellite in October 2011, NTL data from the Visible Infrared Imaging Radiometer Suite onboard have become available. Its on-board calibration capacity and saturation-free merit have made NPP-VIIRS a new generation system of nighttime light observations (Elvidge et al., 2013). This new NTL data source will provide improved monitoring of human settlement and land development in hurricane-prone regions for advanced disaster assessment.

4.6 CONCLUDING REMARKS

Floods resulted from hurricanes (mostly originated from the North Atlantic Basin) have posed significant threats to people residing in the U.S Atlantic and Gulf Coasts. A better understanding of the temporal and spatial dynamics of human settlement in these hurricane-prone areas is needed for improved damage assessment and sustainable urban planning.

This chapter examined the spatiotemporal dynamics of nighttime satellite-derived human settlement in 1992-2013 in four zones at different levels of hurricane proneness on the U.S. Atlantic and Gulf Coasts. The hurricane-prone zones were delineated based on historical storm tracks from the North Atlantic Basin during 1851-2016 via a wind speed weighted track density function. A three-step intercalibration framework was applied to intercalibrate the multi-satellite DMSP/OLS NTL series, and the NDVI-desaturated NTL products were extracted to derive VANUI, a popular index representing human settlement intensity. Mann-Kendall trend and Theil-Sen slope were further applied to identify the existing trend in the 22-year period.

Zonal statistics indicate that in the frontmost zones along the coast, i.e., Zone 1 and Zone 2 receiving the most frequent hurricane hits, human settlement intensity has dramatically increased although the change rate has slowed down since the early 2000s. The increase was not significant in areas farther away from the coasts (Zone 3 and Zone 4). Via trend analysis, 4.22% of the area in Zone 1 experienced a significant increase in settlement intensity, followed by 2.34% in Zone 2, 2.08% in Zone 3 and 1.65% in Zone 4, revealing higher pressure of human settlement and thus impacts from hurricanes in the frontmost coastal areas. Different from the zonal partitions, opposite trends of human settlement were observed from the north (decreasing) to the south (increasing) of the study region, which are supported by decadal census records. These opposite trends agree with the “Snow Belt-to-Sun Belt” U.S population shift reported in other studies. Along the Atlantic and Gulf coasts, the ongoing intensification of anthropogenic environmental changes coupled with more frequent and severe hurricanes is likely to cast more severe pressure on coastal resilience.

Beyond the flood exposure and awareness on the U.S. coast, flood risk perception in the entire CONUS also needs to be properly benchmarked, allowing a comprehensive evaluation of the impact on those likely to bear the eventual coast of flooding. Taking advantage of the recently released Microsoft building footprints and the ACS 5-year estimates, the following chapter (Chapter 5) describes a fine-scale comparative assessment of the exposed population within the 100-year floodplains in the CONUS.

CHAPTER 5

BENCHMARKING THE POPULATION EXPOSURE TO FLOOD RISKS IN THE CONTERMINOUS U.S⁴

5.1 INTRODUCTION

The 100-year floodplain (1% of annual exceedance probability), produced by the Federal Emergency Management Agency (FEMA) in 1968, has been the longstanding marker for deciding federal flood insurance, housing protective actions, and local mitigation policies (Blessing et al., 2017). Numerous estimations have been conducted based on the boundary of FEMA 100-year floodplain to estimate the population exposure and how this exposure is distributed nationwide (Crowell et al., 2010; Qiang et al., 2017; Yager et al., 2018). Those estimations, however, greatly differ from each other and are intrinsically limited because they failed to capture the great heterogeneity of population distribution at the micro-level.

Population data in the United States is repetitively surveyed by the Census Bureau in different geographical units. The commonly used population data in the U.S include U.S Decennial Census (block as the smallest unit) and American Community Survey (ACS) (block group as the smallest unit). However, the aggregated population data within the

⁴ Huang, X., Wang, C. Estimates of exposure to the 100-year floods in the Conterminous United States using national building footprints. Submitted to the *International Journal of Disaster Risk Reduction*.

census unit, especially within large polygons in rural areas, only represent the total population and do not necessarily suggest real population distribution of the unit (Wardrop et al., 2018; Huang et al., 2019e). Crowell et al. (2010) estimated the population exposure of coastal floods in the U.S by assuming a uniform distribution of population within block groups. Yager et al. (2017) assigned the population in the U.S census tract based on the percentage of its census blocks covered by FEMA floodplain. Wing et al. (2018) improved the population distribution for estimating population exposure by disaggregating the population in the census block based on land use types and slope in the unit. Another study applied the modeled km-level population grids by overlaying grid centroids with flood hazard maps (Fang et al., 2018). Despite their efforts in deriving the population within flood hazard zones, these studies failed to find a proxy that can better characterize the micro-level population in the floodplain. Given the small, zigzagging, and rather narrow floodplain polygons, great uncertainty might be introduced if heterogeneity of population distribution is not well considered.

Spatial heterogeneity can be efficiently outlined from high-resolution satellite imagery. For example, Bing Maps from Microsoft released more than 125 million of building footprints covering the entire U.S in June 2018 (open-sourced in <https://github.com/Microsoft/USBuildingFootprints>), which is believed to be the most comprehensive inventory of national building footprint at the time of writing. People live in buildings. The direct linkage between the distribution of buildings and that of the population largely facilitates characterizing population distribution and greatly aids in summarizing population residing in a certain boundary.

In addition, a comparative study is needed to estimate the exposed population to floods, given the numerous limitations of FEMA boundaries. FEMA floodplains have been criticized by many as they are only partially complete nationwide. Only 55.0% of the counties in the conterminous U.S (CONUS) have the complete flood map coverage, whereas 22.7% have no flood map available (Qiang et al., 2017). In addition, Birkland et al. (2003) found that approximately 33% of the FEMA maps were more than 15 years old, and another 30% were 10-15 years old. Despite that this problem is being addressed by the Modernization Management Support (MMS) program of FEMA, the updating process takes time, and the varying age issue can not be fully resolved. In light of the limitations of FEMA floodplains, the availability of floodplains from other sources provides additional valuable insights on how the exposed population is distributed in those floodplains. Therefore, comparing the estimation from FEMA with the estimations from other available floodplain products allows us to gain a comprehensive understanding of the exposed population in the U.S.

This chapter explores an improved flood exposure assessment by utilizing the Microsoft building footprints to disaggregate the block group population from the latest ACS 5-year estimates (2013-2017). The outputs of flood exposure are statistically compared between the 100-year FEMA floodplains and three popular open-source floodplain products in the CONUS. The findings from this national assessment provide valuable benchmark information regarding current flood exposure (100-year flood) in the CONUS by answering the following questions: 1) how many people are exposed? 2) who are they? 3) how are they distributed? And 4) how do the estimations from other floodplains differ from the estimations from FEMA floodplain?

5.2 DATASETS

The primary datasets used in this chapter include 1) Microsoft computer-generated national building footprints: to capture population heterogeneity within the geographic boundary of census unit; 2) Census data: to serve as aggregated ground-truth population from which building footprints can disaggregate; 3) Land use datasets including NLUD 2010 and OpenStreetMap land use polygons: to trim raw building footprints by removing residential-irrelevant buildings before the disaggregation process; 4) FEMA floodplain: to serve as a baseline flood boundary within which population statistics are summarized; 5) Open access floodplain products: to compare with the estimates from the official FEMA floodplain boundary.

5.2.1 Microsoft building footprints

The building footprint dataset used in this chapter was released by the Bing Maps team in June 2018, relying on Open Source Microsoft Cognitive Toolkit (CNTK) and 5 million labeled Bing imagery. It is reported that the extracted building footprint dataset reaches a commission error of 0.7% and an omission error of 6.5% nationwide (Microsoft USBuildingFootprints, 2018). The original dataset consists of a total of 125,192,184 building footprint polygon geometries in all 50 U.S states in GeoJSON format. After confining with the CONUS boundary (48 states, D.C. included), 124,828,547 footprints are remained and projected to U.S Albers equal-area conic projection for to preserve the size information. Note that the dates of extracted buildings are undetermined due to the fact that Bing imagery consists of varying sources. Information regarding building height and building type is not recorded in the dataset.

5.2.2 Census data

The Census data used in this chapter is derived from American Community Survey (ACS) by the U.S Census Bureau, an ongoing survey that regularly gathers vital information about population statistics previously contained only in the long form of the U.S Decennial Census. Given that U.S Decennial Census is issued every ten years, the ACS is regarded superior to U.S Decennial Census in its better temporal interval (Mather et al., 2005) and, therefore, is more suitable for an updated estimation of the population exposed to flood. With a 60-month sampling period from Jan 1st, 2013 to Dec 31st, 2017, the latest (at the time of writing) ACS 5-year estimate (2013-2017) is selected. Its long sampling period increases the statistical reliability when examining small geographical areas and is believed to be more reliable compared with ACS 1-year and ACS 5-year estimates (Gaquin and Ryan, 2018). Due to the fact that the smallest geographical unit in ACS 5-year estimates is block group, the U.S block group boundary (2017 version) is obtained from Topologically Integrated Geographic Encoding and Referencing (TIGER) in shapefile format. A total of 266,330 block groups are derived within the CONUS boundary.

5.2.3 Land use datasets

Buildings in the Microsoft national building footprint dataset are with different functionality. To establish a better linkage between the distributions of buildings and population, trimmed the raw building dataset were further trimmed by removing footprints that are not likely residential. Two land use datasets were applied to fulfill this goal: National Land Use Dataset 2010 (NLUD 2010) and OpenStreetMap (OSM) land use polygons.

NLUD 2010

Developed by Theobald (2014), NLUD 2010 aims to provide comprehensive, detailed and high-resolution (30 m) land use classification for the CONUS. It was constructed through spatial analysis of nearly two-dozen publicly available national spatial datasets covering housing, employment, infrastructure, and satellite-based land cover (Theobald, 2014). It includes 79 land use classes that fit within five main land use groups: water, built-up, production, recreation, and conservation (Table A.1). Specifically, the built-up category is further subdivided into residential, commercial, industrial, institutional, transportation, and miscellaneous. Comparing with USGS National Land Cover Dataset (NLCD) classified from remote sensing imagery, NLUD 2010 better distinguishes the populated buildings and unpopulated buildings as well as other impervious surfaces (Dmowska and Stepinski, 2017).

OSM land use polygons

OSM is a collaborative open-source and open-access project to collect geographic information from the public. As one of the most successful Volunteered Geographic Information (VGI) platforms, its large userbase (5.5 million users in the year 2019) provides rich and detailed land use information with decent coverage in the CONUS (OSM, 2019a). The massive land use polygons annotated by millions of volunteers transcend widely used land cover information that often fails to distinguish types of building usage at the individual level.

The OSM land use polygons used in this chapter were retrieved from GEOFABRIK (<https://www.geofabrik.de/geofabrik/>), a company that updates OSM data on a daily basis. OSM land use data was downloaded on March 1st, 2019. In the CONUS, there are a total

of 1,714,072 user-annotated land use polygons with 19 unique land use classes (Table A.2). Specifically, land use type “Residential” (Code 7203) represents an area of land dedicated to predominantly residential buildings such as houses or apartment buildings (OSM, 2019b). It greatly contributes to the extraction of residential buildings from the raw building footprint dataset in this study.

5.2.4 FEMA 100-year floodplain

As the primary metric for predicting and acting on the possibility of a specific area being inundated during a rainfall or wave-based event, FEMA floodplains provide essential guidance for local planning, insurance purchases and regional development in the U.S. This study utilizes the FEMA 100-year floodplain boundary because it is the basis for floodplain management and the minimum requirement for participation of local governments in the National Flood Insurance Program (NFIP) (Burby et al., 1988; Blessing et al., 2017). In this chapter, FEMA 100-year floodplain was obtained from the National Flood Hazard Layer (NFHL) at FEMA Flood Map Service Center. The NFHL was downloaded on April 1st, 2019 in ESRI shapefile format.

In the NFHL data, high flood risk areas represent areas that are inundated by a 1-percent chance of being equaled or exceeded in any given year (FEMA, 2019). Flood risk zones in NFHL are classified into three categories (FEMA, 2019): 1) Moderate to Low Risk Areas (zones B, C, and X); 2) High Risk Areas (zones A, AE, AH, AO, AR and A99, V and VE); and 3) Undetermined Risk Areas (Zone D). In the remainder of this chapter, Zone V and Zone VE (flood risks due to wave action) are denoted as 100-year coastal floodplain and other zones in NFHL High Risk Areas are denoted as 100-year fluvial/pluvial (F/P) floodplain.

The NFHL has not completely covered the CONUS, as floodplain maps for a total of 513 counties (16.51%) in CONUS are not available (Figure 5.1). Counties with no floodplain maps are mostly located in the Mountain States, including Colorado, Wyoming, Utah, New Mexico, Nevada, Idaho, Arizona, and Montana.

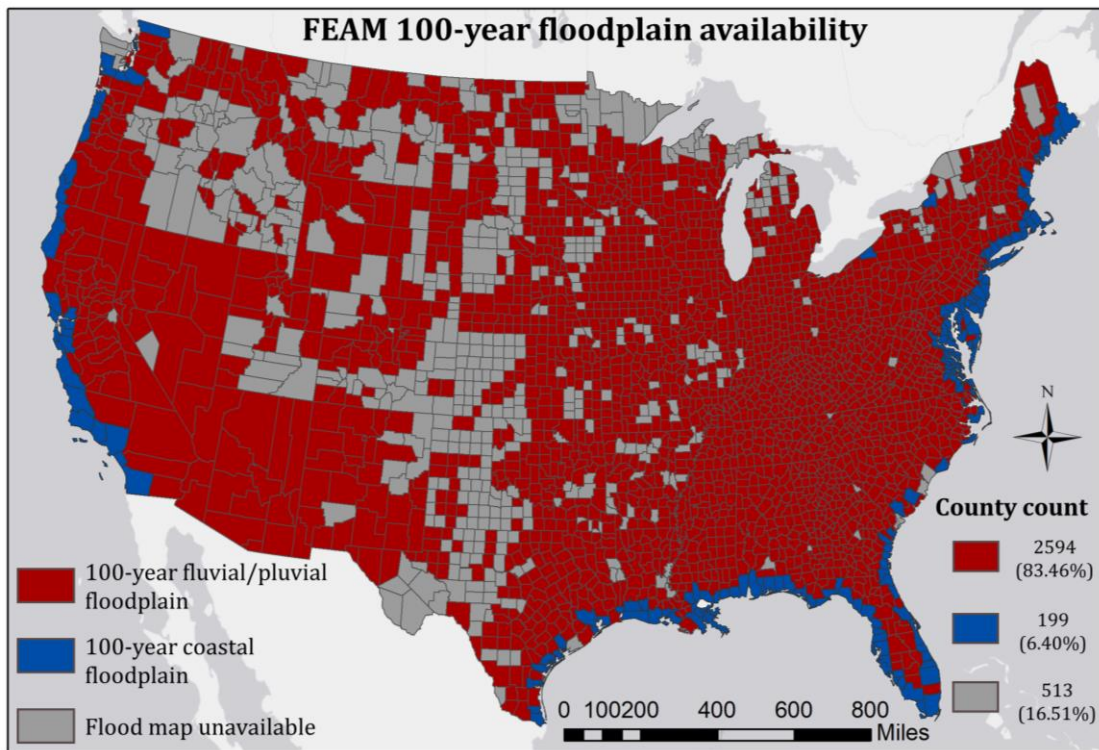


Figure 5.1 FEMA 100-year floodplain availability in CONUS at county level (FEMA floodplain retrieved on April 1st, 2019).

5.2.5 Open-access 100-year floodplain products

Three open-access 100-year floodplain products were selected for comparative analysis against the FEMA boundary for a comprehensive estimation of the population exposed to a 100-year flood in the CONUS. Those 100-year floodplain products were respectively termed as RFCON (Woznicki et al., 2019), GAR (Rudari et al., 2015), and JRC (Dottori et al., 2016).

RFCON floodplain was derived via a random forest classifier using soil characteristics and DEM-derivatives. With the classifier trained by FEMA floodplain, RFCON presents a spatially complete 100-year floodplain (both fluvial/pluvial and coastal) for the entire CONUS, greatly compensating the coverage limitation of FEMA floodplain (Woznicki et al., 2019).

GAR floodplain was developed by the Global Assessment Report (GAR) on Disaster Risk Reduction 2015 from the United Nations Office for the Disaster Risk Reduction (UNISDR). As an official floodplain issued by the United Nations, GAR captures fluvial/pluvial 100-year flood extent on a global scale.

JRC floodplain was released in 2016 by the European Commission Joint Research Center (EC-JRC). Same as GAR, JRC mainly considers the extent of fluvial/fluvial floods globally. Other details of the three floodplain products can be found in Table 5.1.

Table 5.1 Summary of open access 100-year floodplain products used in this chapter.

	GAR (Rudari et al., 2015)	JRC (Dottori et al.,2016)	RFCON (Woznicki et al., 2019)
Resolution	30 arc-seconds (1km)	30 arc-seconds (1km)	1 arc-second (30m)
Year issued	2015	2016	2019
Floodplain type	Fluvial/pluvial	Fluvial/pluvial	Fluvial/pluvial and coastal
Coverage	Global	Global	CONUS

Methods ^a	Simulated floodplain using regional flood frequency approach to estimate flood flows from pooled river gauged data. The floodplain was simulated via a flood volume redistribution model, GLOFRIS.	Simulated floodplain using cascade of precipitation time series from global climate reanalysis data driving a land surface model to produce flows at locations along a river. The floodplain was simulated via a 2D hydrodynamic model.	Trained floodplain via a random forest classifier using DEM-derivatives and flood-based soil characteristics. The random forest model was trained on FEMA floodplain.
Sources	Global Assessment Report on Disaster Risk Reduction 2015 from the United Nations Office for Disaster Risk Reduction (UNISDR) (https://www.preventionweb.net/english/hyogo/gar/2015/en/home/data.php)	European Commission Joint Research Center (EC-JRC) (https://data.jrc.ec.europa.eu/collection/id-0054)	Research data available from the United States Environmental Protection Agency (EPA) EnviroAtlas (https://www.epa.gov/enviroatlas/enviroatlas-interactive-map).

^aMethods in GAR and JRC are summarized in Trigg et al. (2016) and Bernhofen et al. (2018).

5.3 METHODS

The methodology in this chapter follows a general workflow described in Figure 5.2. The raw Microsoft national building footprint dataset was first trimmed based on two land use datasets, NLUD 2010, and OSM land use polygons, to remove buildings that are not likely residential (Section 5.3.1). After trimming, buildings were used to disaggregate population statistics from ACS 2013-2017 at the block group level into building level (Section 5.3.2). Finally, building-level statistics were summarized and spatially compared among different floodplain products (Section 5.3.3).

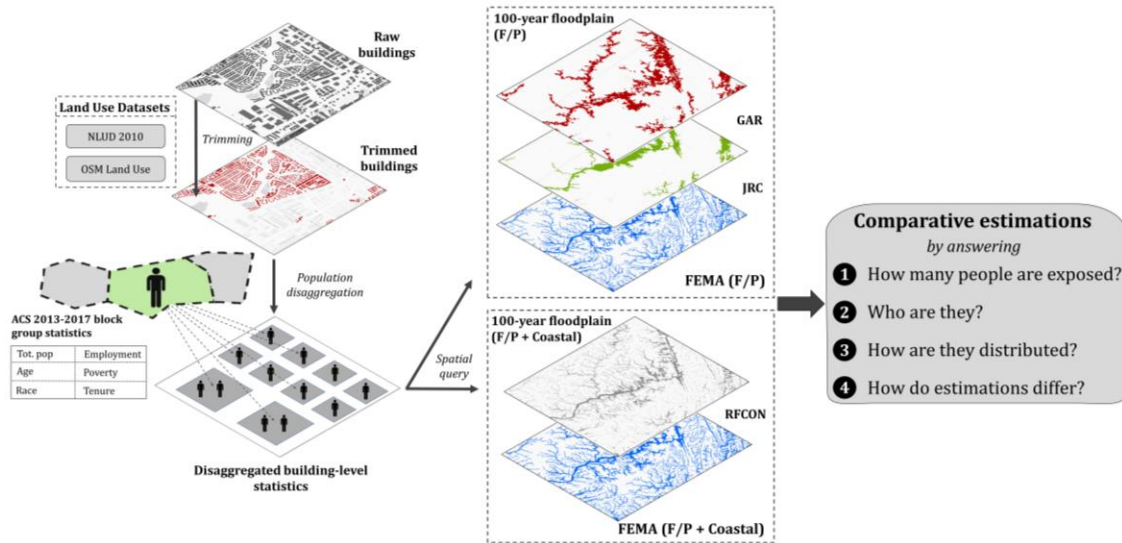


Figure 5.2 General workflow of estimating the population exposed to 100-year floods in the CONUS using national building footprints.

5.3.1 Building footprint trimming

The building footprint trimming process confines population distribution to residential-relevant buildings, thus greatly capturing the heterogeneity of population distribution at the micro-level. In the NLUD 2010 dataset, residential (subcategory) was selected (from built-up category), which includes: dense urban residential (Code 211), urban residential (Code 212), suburban residential (Code 213), exurban residential (Code 214) and rural residential (Code 215). In addition, highway/railway (Code 252) was included as some residential buildings are very close to transportation, meaning that those residential buildings are likely to fall within highway/railway cells. The detailed coding scheme of the NLUD 2010 dataset can be found in Theobald (2014). In the OSM land use dataset, land use type “Residential” (Code 7203) was selected as it indicates an area of land having predominantly residential buildings. The building trimming process kept building footprints that are within either the aforementioned land use type in those two datasets.

In addition, the raw Microsoft national building footprint dataset contains many small footprints that are not likely habitable (e.g., garages and temporary awnings). To remove those small polygons, the size of the minimum footprint was empirically set to be $50 m^2$. Extra-large footprints that are unlikely residential were also removed by a maximum threshold of $5,000 m^2$. The analyses in the remainder of the chapter used the trimmed building footprints.

5.3.2 Population disaggregation

As the smallest unit of ACS product, each block group represents a geographical area with homogeneity of aggregated statistics. However, they are spatially distributed with great heterogeneity. It is reasonable to assume that 1) the statistics of a block group are only confined to the building footprints within this block group, and 2) are distributed proportionally to the size of the building footprint that characterizes the horizontal holding capacity of a building. Here, the proportion (S) of a building footprint shared within its block group can be calculated as:

$$S_R^i = \frac{BF_{size}^i}{\sum_i BF_{size}^i} \quad (i \in R) \quad (5.1)$$

where S_R^i denotes the areal percentage of building i within block group R and BF_{size}^i denotes the building footprint size of building i . Note that the disaggregation process redistributes population statistics to individual building within a block group while preserves the sum of statistics reported at the block group level, i.e., the sum of S within block group R equals 1 ($\sum_{i \in R} S_R^i = 1$). The statistics of block group R (P_R) are further distributed to building i according to its share (S_R^i):

$$P_R^i = S_R^i \times P_R \quad (5.2)$$

where P_R^i denotes the statistics of building i within block group R . The statistics aggregated at ACS block group level are also preserved as $P_R = \sum_{i \in R} P_R^i$.

In this study, P_R includes total population and six socioeconomic variables: age, employment, race, ethnicity, tenure, and poverty. Details for the six socioeconomic variables are presented in Table 5.2.

Table 5.2 Statistics of block group R (P_R) included in this chapter.

Category	Subcategory
Age ^a	Under 5
	5 to 14
	14 to 25
	25 to 34
	35 to 44
	45 to 54
	55 to 64
	65 to 74
	75 to 84
Above 85	
Race	White
	Black or African American
	American Indian and Alaska native
	Asian alone
	Native Hawaiian and Pacific Islander
	Some other races
	Two or more races
Ethnicity	Hispanic or Latino
	Not Hispanic or Latino
Employment ^b	Employed
	Unemployed
Tenure ^c	Owner Occupied
	Renter Occupied
Poverty ^d	Under 1.0 (Doing poorly)
	1.00 to 1.99 (Struggling)
	Above 2 (Doing Ok)

^aAge category is modified from ACS 5-year estimates (2013-2017) from the U.S Census Bureau.

^bEmployment denotes the employment status of the civilian population in the labor force 16 years and over.

^cTenure is counted by households.

^dPoverty denotes the ratio of income to the poverty line.

5.3.3 Spatial query and comparative exposure estimation

After the disaggregation of statistics of ACS block groups to the statistics of the individual building, a spatial query was performed to extract buildings that fall within the FEMA floodplain boundary as well as the other three floodplain boundaries. To facilitate the query, building footprint polygons were converted to point features, and the FEMA floodplain boundary was converted to a binary raster. Statistics of buildings within floodplain boundaries were further summarized in the CONUS as a whole, as well as at the county level, to shed light on the distribution pattern of current flood exposure across the CONUS. Counties were selected as the unit of spatial analysis because they maintain the well-established administrative functions (Qiang et al., 2017). Therefore the flood exposure derived in this study can be easily linked to available county-level socioeconomic records to assist local decision-makers.

In addition to the spatial differences in flood exposure among counties, statistics are likely to vary within the same county because of the disparity among the different floodplain products. As the official floodplain in the U.S, FEMA floodplain serves as the baseline estimation with which estimations from other floodplains products were compared. Due to the fact that GAR and JRC mainly estimated fluvial/pluvial floods and RFCON estimated both fluvial/pluvial and coastal floods, two groups of comparison were consequently designed. Estimations from GAR and JRC were compared with estimations from FEMA fluvial/pluvial floodplain (denoted as FEMA (F/P)), and RFCON was compared with FEMA fluvial/pluvial floodplain together with FEMA coastal floodplain

(denoted as FEMA (F/P + Coastal)). The county-level differences in estimations from different floodplain products were standardized by the county population.

Getis-Ord G_i^* was further used to find potential hot spots among floodplain different products. Getis-Ord G_i^* is a spatial clustering statistic that summarizes statistically significant spatial patterns by looking at each feature within the context of neighboring features (Ord and Getis, 1995; Getis and Ord, 2010):

$$G_i^* = \frac{\sum_{j=1}^n w_{i,j} x_j - \bar{x} \sum_{j=1}^n w_{i,j}}{S \sqrt{\frac{n \sum_{j=1}^n w_{i,j}^2 - (\sum_{j=1}^n w_{i,j})^2}{n-1}}} \quad (5.3)$$

where x_j denotes the differences in estimated population exposure in proportion to the total population in county j , n denotes the total number of counties, $w_{i,j}$ denotes the spatial weight between county i and county j (counties within a fixed Euclidean distance that ensures every county has at least one neighbor are computed equally), \bar{x} denotes the mean ($\frac{\sum_{j=1}^n x_j}{n}$), and S is calculated as:

$$S = \sqrt{\frac{\sum_{j=1}^n x_j^2}{n} - (\bar{x})^2} \quad (5.4)$$

Three significant levels were summarized: $\alpha = 0.01$, $\alpha = 0.05$, and $\alpha = 0.1$. They respectively correspond to the identification of hot spots (or cold spots) with 99% significance, 95% significance, and 90% significance.

5.4 RESULTS

5.4.1 How many people are exposed?

In term of fluvial/pluvial floodplain (F/P), FEMA (F/P) estimates a total of 10.992 million exposed population in the CONUS (Figure 5.3). In comparison, JRC and GAR respectively estimate 12.091 million and 14.161 million, which are 1.099 million and 3.169 million

more than the FEMA estimation (Figure 5.3). It suggests that the estimation of flood exposure from FEMA is less than the ones from other official sources like JRC floodplain and GAR floodplain. When considering coastal floods, FEMA (F/P + Coastal) estimates that a total of 11.119 million people in the CONUS are currently facing the danger of floods. This estimation is 890 thousand shy of the estimation from RFCON (12.080 million), a spatially complete 100-year floodplain for the entire CONUS. The incomplete coverage of FEMA floodplain (as shown in Figure 5.1 above) potentially limits its capability of providing a comprehensive flood exposure analysis in the CONUS.

5.4.2 Who are they?

Age

Figure 5.3 presents the age compositions of the exposed population in the CONUS for two groups of comparisons. Similar age compositions can be found from estimations using different floodplain products. The age compositions exposed to flood are generally in accordance with the age compositions of the entire U.S, indicating that there is no significant age bias towards different age groups in terms of flood proneness. When flooding occurs, children and the elderly may face a particular set of challenges because extremes of the age spectrum affect the movement out of harm's way. FEMA (F/P) estimates that around 1.957 million children (under age 14) are exposed to a 100-year F/P flood, whereas two other official sources like JRC and GAR, estimate 2.342 million and 2.620 million respectively. Taking coastal floods into consideration, FEMA (F/P + Coastal) estimates a total of 1.971 million children, and in comparison, RFCON estimates 2.182 million. As RFCON is spatially complete and trained using FEMA floodplain, it means that the gap of 211 thousand underestimated children by FEMA is primarily due to the

incompleteness of FEMA floodplain. As for the elderly (above 65), estimations from FEMA (F/P) and JRC are similar as they respectively estimate 1.878 million and 1.769 million, while GAR estimates a significantly higher number, 2.517 million. Considering coastal floods, FEMA (F/P + Coastal) underestimates 132 thousand seniors compared with RFCON.

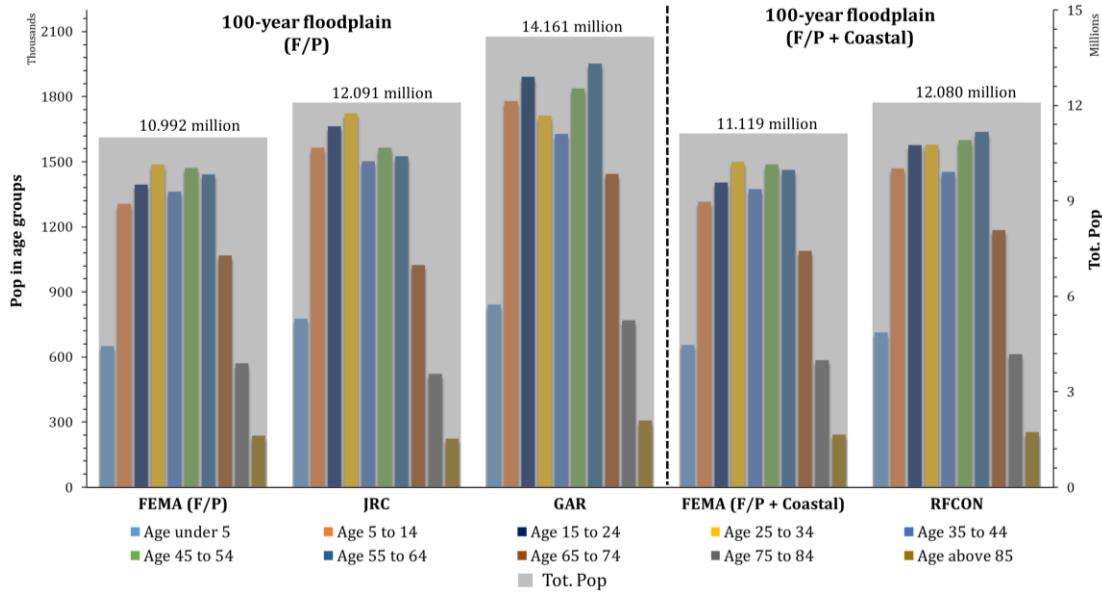


Figure 5.3 Age composition exposed to 100-year floodplains in the CONUS.

Race and Ethnicity

Figure 5.4 shows the race composition of the population exposed to the 100-year flood in the CONUS in two groups of comparisons. Comparing three F/P floodplain products, the estimation of GAR differs greatly from the other two. In its total exposed population (14.161 million), GAR estimates that the White group and the African American group respectively consist of 82.9% (11.74 million) and 9.6% (1.36 million). In comparison, however, the White group percentages in FEMA (F/P) and JRC are considerably lower, 75.5% and 71.7% respectively, and the African American group percentages are considerably higher, 12.6% and 14.3% respectively. In addition, GAR estimates the

exposed Asian group to be 150 thousand, significantly lower than estimation from FEMA (F/P) (430 thousand) and estimation from JRC (610 thousand) (Figure 5.4). Considering coastal floods, RFCON overestimates 1.19 million of the white group and underestimate 280 thousand of the African American group, compared with FEMA (F/P + Coastal). It is worth mentioning that Race compositions in the entire U.S and in FEMA floodplains (both FEMA (F/P) and FEMA (F/P + Coastal)) are highly similar in all race groups (Figure 4), indicating that FEMA estimations suggest no racial bias towards flood exposure. Other floodplains, however, tend to overestimate the white group and underestimate the African American group.

As for ethnicity, the percentage of the Hispanic or Latino group in the U.S is 17.6%. This number reaches 24.7% and 24.5% in FEMA (F/P) and FEMA (F/P + Coastal), respectively (Figure 5.5), suggesting that the Hispanic or Latino group tends to live in FEMA floodplains according to FEMA. However, the percentage of the Hispanic or Latino group in the GAR floodplain is 10.3%, suggesting otherwise. No bias is found against the Hispanic or Latino group in RFCON as it estimates a percentage of 17.7%, quite close to the national percentage of Hispanic or Latino group.

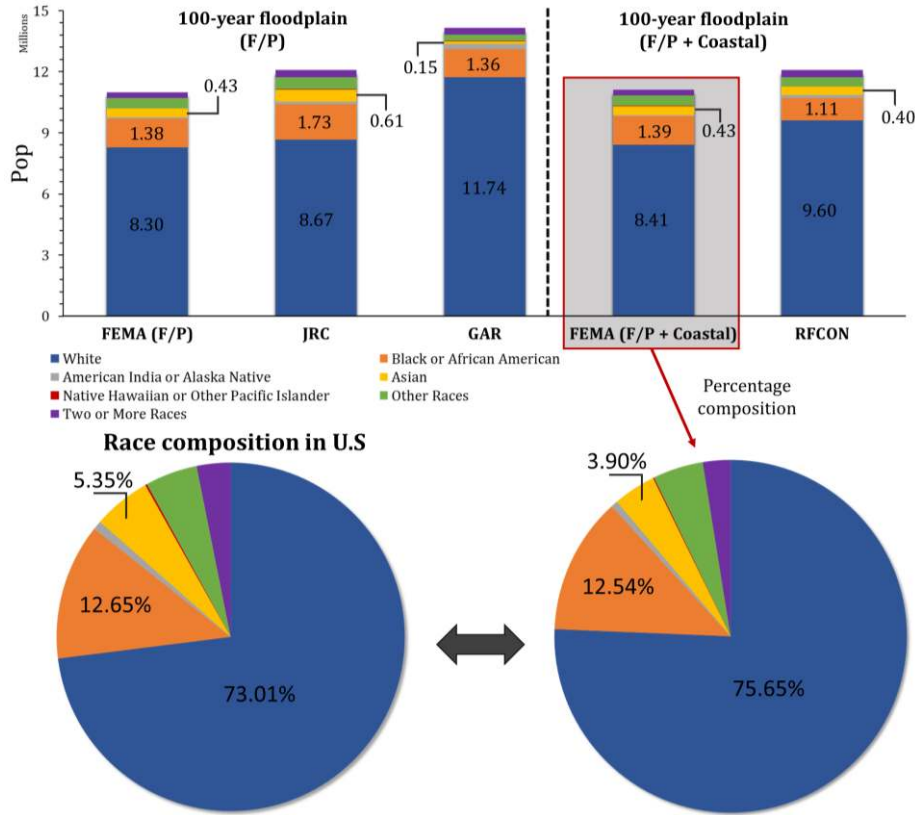


Figure 5.4 Race composition exposed to 100-year floodplains in the CONUS.

Tenure

As shown in Figure 5.5, 36.2% of all housing units are occupied by renters and 63.8% by owners in the U.S. A slightly higher share of units occupied by renters is found in floodplains of FEMA (F/P) (38.6%), FEMA (F/P + Coastal) (38.4%) and JRC (40.2%). In comparison, a lower share of units by renters is found in GAR with only 31.7%. RFCON doesn't show any bias against tenure status as its 35.5% of renters is very similar to the national statistic of 36.2%.

Employment and Poverty

The employment in this study represents the employment status of the civilian population in the labor force 16 years and over. Following this definition, the national unemployment rate from ACS estimates (2013-2017) is 6.5% (Figure 5.5). In terms of the unemployed

who are exposed to flood danger, the percentages from all selected floodplains are similar and close to national statistic, with FEMA (F/P + Coastal) 7.0%, FEMA (F/P) 7.0%, JRC 7.4%, GAR 7.0% and RFCON 6.8%. The result suggests that employment status is not biased against flood exposure in all selected floodplains.

The poverty defined in this study represents the relative poverty status where the income is divided by the poverty line. Breaking into three categories, a ratio above 2 denotes the wealthy group, a ratio between 1.00 and 1.99 denotes the struggling group, and a ratio under 1 denotes the poor group. In the U.S, these three groups respectively consist of 67.3% (the wealthy group), 18.2% (the struggling group), and 14.6% (the poor group) (Figure 5.5). Considering the flood exposure, however, a lower percentage of the wealthy group and a higher percentage of the poor group are found within all five selected flood plains. For example, within FEMA (F/P +Coastal) floodplain, the wealthy group consists of 4.4% less, and the poor group consists of 2.2% more, compared with the national statistic. Estimations from other floodplain products also suggest less percentage of the wealthy group facing flood risks. The unanimous agreement of all five floodplains, despite the small variance, reveals that the poor group tends to live within the floodplain and therefore, face higher risk and rescue challenge during flood events. Detailed statistics regarding these six socioeconomic variables within floodplains can be found in Table A.3.

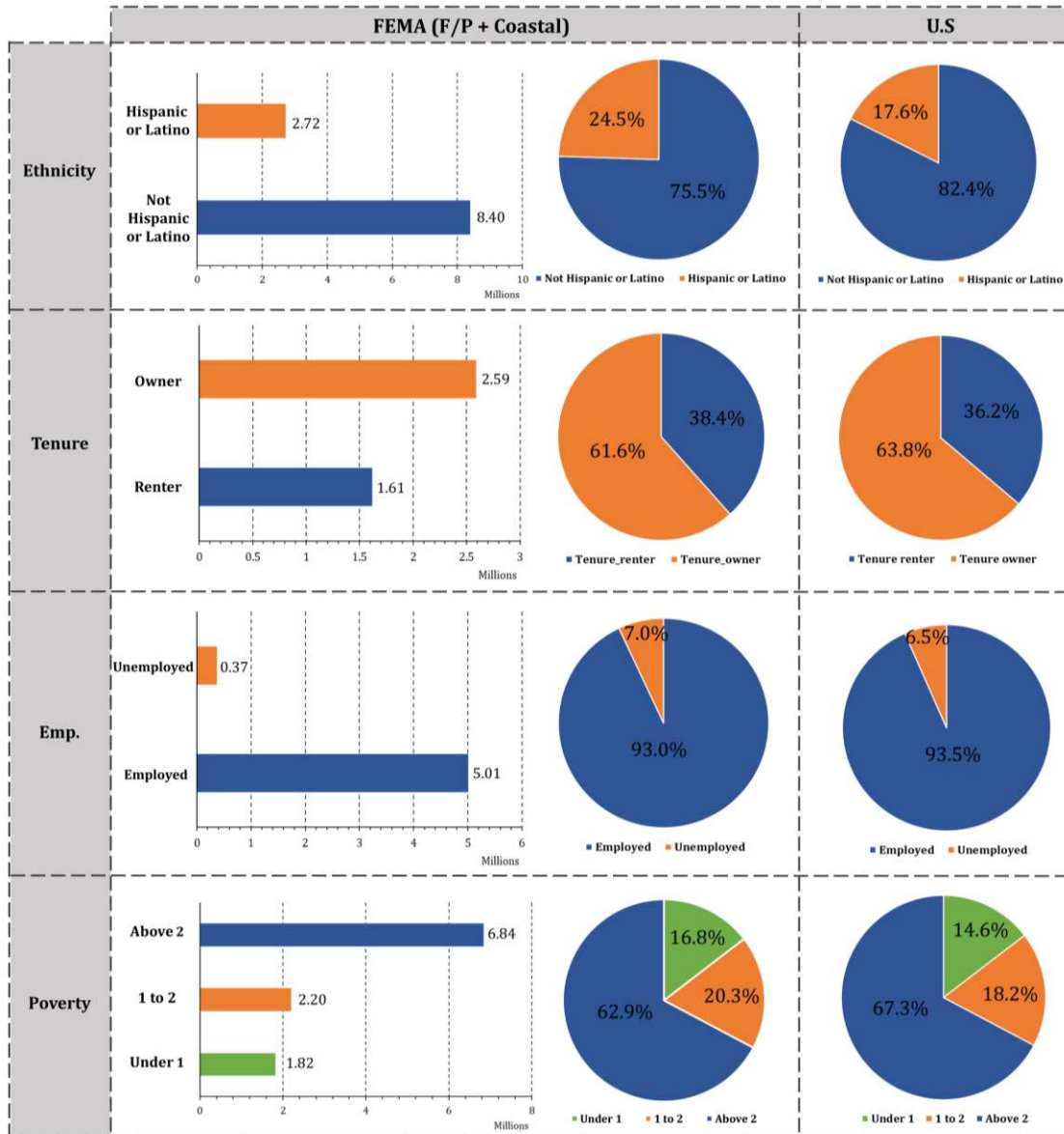


Figure 5.5 Composition of ethnicity, tenure, employment, and poverty in FEMA (F/P + Coastal) with the composition from the entire U.S.

5.4.3 How are they distributed?

Fluvial/Pluvial (F/P) flood

In the first group of comparison, the spatial distribution of population exposure at the county level was compared in floodplains that only consider F/P flood: FEMA (F/P), JRC, and GAR (Figure 5.6). To reveal the spatial patterns, the county-level exposed population

of the aforementioned three floodplains is categorized in ten quantiles at a 10% interval. As expected, counties near major river channels are more likely located in 100-year floodplains and, therefore, tend to have more people exposed to flood danger, especially the case for JRC (Figure 5.6a). For example, a high concentration of exposed population can be easily found along the Mississippi River, Missouri River and Arkansas River, which coincides with the fact that floods from those three rivers usually inflict severe damage on the public. In contrast, less population exposure can be found in counties in the western mountainous region and the eastern inland region.

Despite those agreements, the spatial distribution of the exposed population estimated from the selected three floodplains varies greatly. In contrast with JRC that mainly captures high exposure in counties along major rivers (Figure 5.6a), FEMA (F/P) also highlights the high exposure in counties on Gulf Coast, West Coast, and Atlantic Coast (Figure 5.6c). GAR floodplain obviously captures more population exposure in the central U.S, despite the fact that most of those counties are in the lowest quantile (dark blue) (Figure 5.6b).

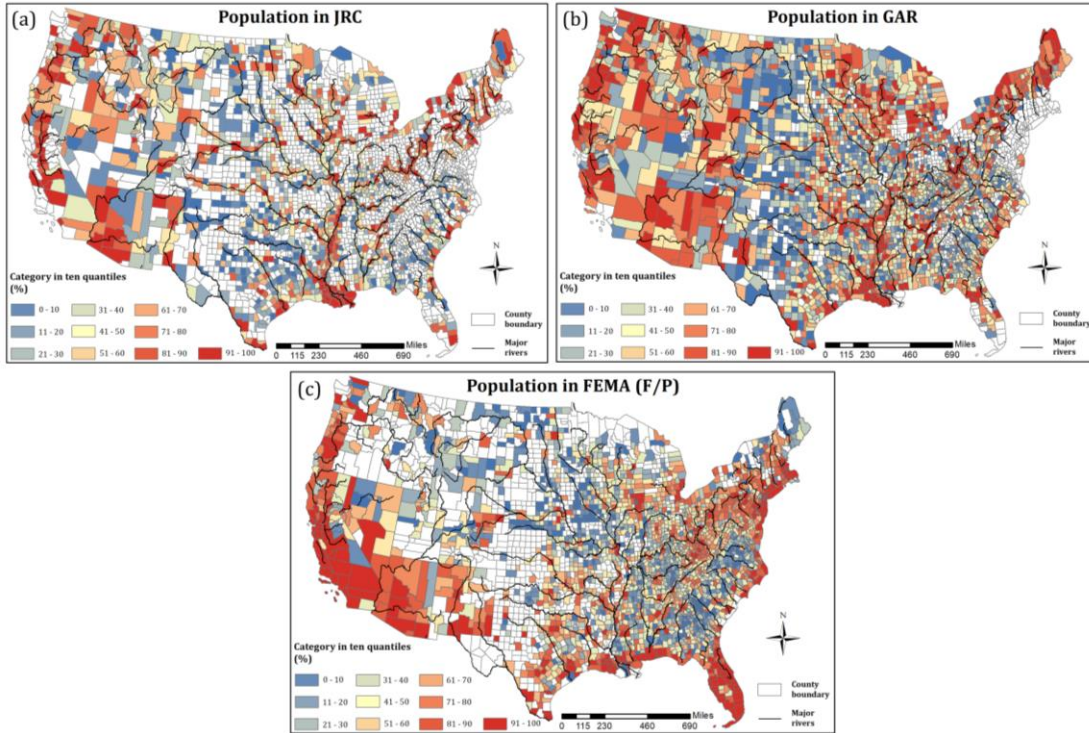


Figure 5.6 Population distributed in the JRC (a), GAR (b), and FEMA (F/P) (c) floodplains.

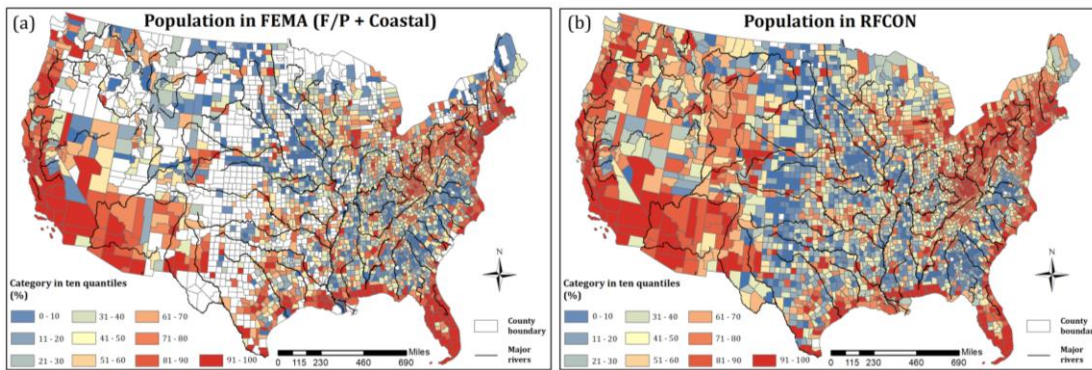


Figure 5.7 Total population distributed in RFCON and FEMA (F/P + Coastal).

Fluvial/Pluvial and Coastal flood combined (F/P + Coastal)

The second group of comparison focuses on comparing floodplains that consider both F/P floods and coastal floods: FEMA (F/P + Coastal) (Figure 5.7a) and RFCON (Figure 5.7b). Given that RFCON is trained by FEMA floodplain in available locations and then extends its coverage to the entire CONUS, RFCON provides a scenario in which population

exposure is theoretically captured using a spatially complete FEMA floodplain. In general, a high similarity is found in places where FEMA floodplain is available, with high exposure in counties along the major rivers and U.S coasts (Figure 5.7). However, in counties where FEMA floodplain is unavailable (mostly in central U.S and Mountain States), RFCON reveals that majority of counties are within low quantiles (blue) but some of them, e.g., Sweetwater County in Wyoming and Malheur County in Oregon, are with high flood exposure (red). Those counties, lying outside the coverage of FEMA floodplains but with high exposure, are potentially responsible for the flooding losses that failed to be captured in the U.S (Blessing et al., 2017).

A further comparison was conducted between FEMA (F/P + Coastal) and RFCON by ranking the top ten counties with the total population exposed and with the proportion of the population exposed. In terms of the total population exposed (Table 5.3), Miami-Dade County, FL ranks the first in both floodplains. However, the number of people exposed to a 100-year flood varies greatly from 1.2 million in FEMA floodplain to 260k in RFCON. Four counties are both mentioned in the top ten ranks: Sacramento County, CA, and Miami-Dade County, Pinellas County, and Hillsborough County, FL. In terms of the proportion of the population exposed (Table 5.4), four counties appear in both lists, with Hyde County in NC and Monroe County in FL ranking the first and the second, respectively. Statistics for these two counties in two floodplains are nearly identical, with 90.1% from FEMA in contrast with 90.5% from RFCON in Hyde County, and 86.4% from FEMA in contrast with 84.6% from RFCON in Monroe County.

Table 5.3 The top 10 ranked counties by the total population exposed to 100-year fluvial/pluvial and coastal floods (F/P + Coastal).

Rank	FEMA (F/P + Coastal)			RFCON		
	County	Pop	% of pop	County	Pop	% of pop
1	Miami-Dade (FL)	1,195,511	44.2	Miami-Dade (FL)	260,550	9.6
2	Harris (TX)	457,778	10.1	Sacramento (CA)	200,939	13.4
3	Broward (FL)	296,433	15.7	Pinellas (FL)	166,309	17.5
4	Pinellas (FL)	249,200	26.2	Maricopa (AZ)	134,321	3.2
5	Lee (FL)	237,214	33.9	Bernalillo (NM)	124,289	18.4
6	Collier (FL)	194,874	54.6	Cameron (TX)	119,719	28.5
7	Hillsborough (FL)	171,395	12.7	Orange (CA)	117,415	3.7
8	Jefferson (VA)	150,532	34.4	Hillsborough (FL)	113,758	8.4
9	Santa Clara (CA)	125,711	6.6	El Paso (TX)	113,049	13.5
10	Sacramento (CA)	122,807	8.2	Los Angeles (CA)	98,112	1.0

Note. Counties in bold indicate counties identified by both floodplains.

Table 5.4 The top 10 ranked counties by the proportion of the population exposed to 100-year fluvial/pluvial and coastal floods (F/P + Coastal).

Rank	FEMA (F/P + Coastal)			RFCON		
	County	Pop	% of pop	County	Pop	% of pop
1	Hyde (NC)	4,963	90.1	Hyde (NC)	4,981	90.5
2	Monroe (FL)	64,912	84.6	Monroe (FL)	65,160	84.9
3	Tyrrell (NC)	3,431	83.9	Saline (KS)	40,591	73.3
4	Cameron (LA)	5,304	77.9	Custer (MT)	8,038	67.6
5	Poquoson (VA)	8,462	70.4	Cameron (PA)	3,132	65.9
6	Dare (NC)	22,680	64.0	Logan (CO)	13,347	61.0
7	Custer (MT)	6,553	55.1	Mingo (WV)	15,187	60.4
8	Collier (FL)	194,874	54.6	Bent (CO)	3,493	60.2
9	Brooks (TX)	3,884	53.6	Osborne (KS)	2,097	56.9
10	Willacy (TX)	11,013	50.4	Tyrrell (NC)	2,325	56.9

Note. Counties in bold indicate counties identified by both floodplains.

5.4.4 How do estimations vary compared with FEMA floodplain?

To investigate the spatial biases of exposure estimations from other floodplains against FEMA floodplain, the FEMA estimation was set as a baseline and the county-level differences (standardized by county population) from estimations of other floodplains were calculated. Here, three comparisons are respectively conducted: GAR and FEMA (F/P) (Figure 5.8), JRC and FEMA (F/P) (Figure 5.9), and RFCON and FEMA (F/P + Coastal) (Figure 5.10).

Compared with FEMA (F/P), GAR generally overestimates 11% of the exposed population at the county level (Figure 5.8 (a1)). The distribution of G_i^* Z score, derived from Figure 5.8 (a2), identifies several hot spots and cold spots at three confidence levels with relatively high confidence (Figure 5.8 (b2)). A hot spot can be found along the Mississippi River (highlighted in a purple ellipse), suggesting that FEMA potentially underestimates the exposed population in this flood-prone region. Other hot spots can be found in the state of Idaho and Montana, where FEMA floodplain has incomplete coverage, revealing the existence of a large amount of exposed population that failed to be captured by FEMA. Three major cold spots (highlighted in green ellipses), Miami, Southeastern inlands, and Northeastern Atlantic coast suggest FEMA's overrepresentation of population exposure in these regions.

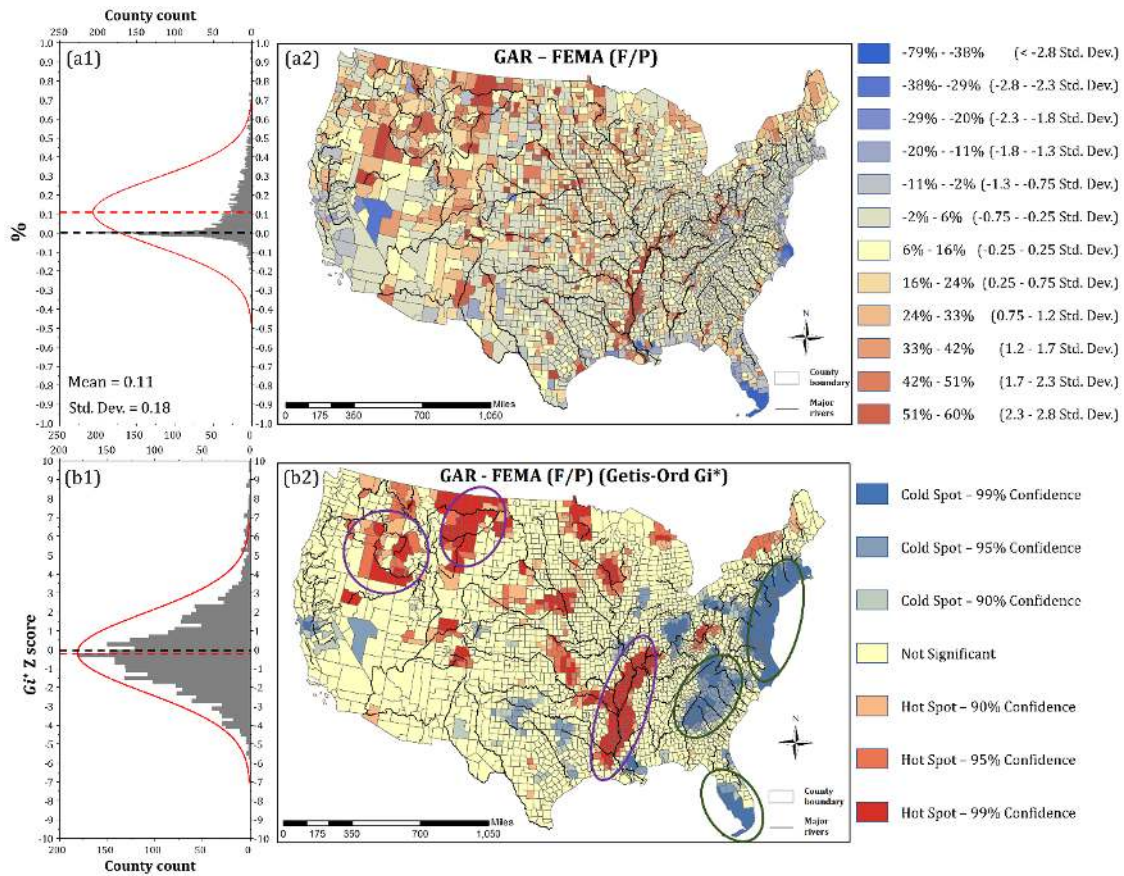


Figure 5.8 County-level differences between exposed population from GAR and FEMA (F/P) in proportion to the county population (a2) associated with county count histogram (a1); County-level G_i^* Z score distribution (b2) associated with county count histogram (b1).

Figure 5.9 presents a comparison between JRC and FEMA (F/P). The mean difference of county-level exposed population in proportion to county population is 0.01 (1%) (Figure 5.9 (a1)), suggesting that JRC has no tendency of either overestimating or underestimating county-level population exposure compared with FEMA estimation in CONUS generally. Spatially, however, population exposure from JRC exhibits a strong disparity against estimation from FEMA (Figure 5.9 (a2)). The distribution of G_i^* Z score reveals similar patterns as it does in the previous comparison (GAR and FEMA (F/P)). Hot spots are also found in the Mississippi River region and Idaho, and cold spots in Miami and on the Northeastern Atlantic coast (Figure 5.9 (b2)). Differently, JRC reveals a new

hot spot and a new cold spot with high confidence, lying respectively in Nebraska and Kentucky/West Virginia (Figure 5.9 (b2)).

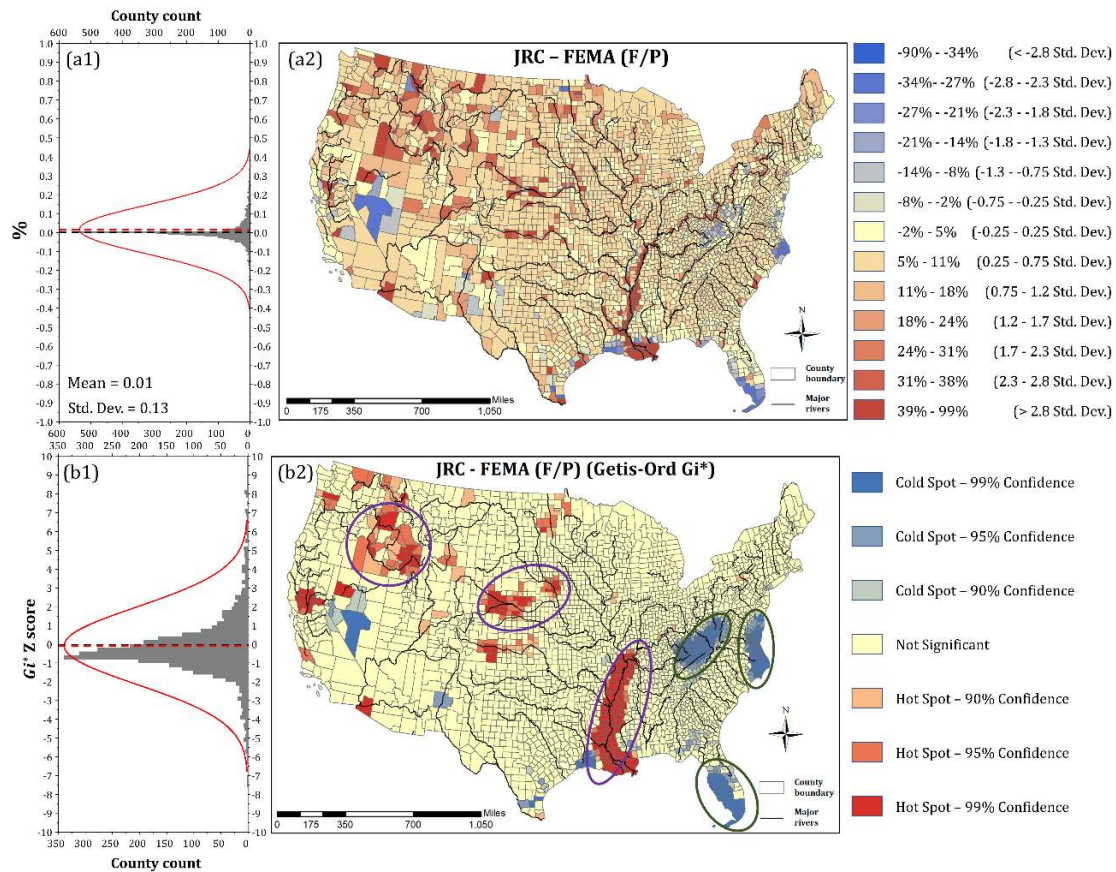


Figure 5.9 County-level differences between exposed population from JRC and FEMA (F/P) in proportion to the county population (a2) associated with county count histogram (a1); County-level G_i^* Z score distribution (b2) associated with county count histogram (b1).

The comparison between RFCON and FEMA (F/P + Coastal) reveals some similar patterns but also opposite ones (Figure 5.10). Generally, RFCON has no tendency of over- or underestimating county-level exposed population (Figure 5.10 (a1)). The distribution of G_i^* Z score shows the same hot spots in Idaho and Montana, and cold spot on the Northeastern Atlantic coast (Figure 5.10 (b2)), in accordance with the findings from two previous comparisons. A cold spot is found covering nearly the entire Florida, different from the ones that only cover the Miami region in two previous comparisons. In the lower

Mississippi River, the comparison between RFCON and FEMA draws an opposite conclusion as it reveals that FEMA potentially underrepresents the exposed population along the Mississippi River. In addition, a hot spot is found in Kentucky/West Virginia, opposing to the cold spot in the same location in the comparison between JRC and FEMA.

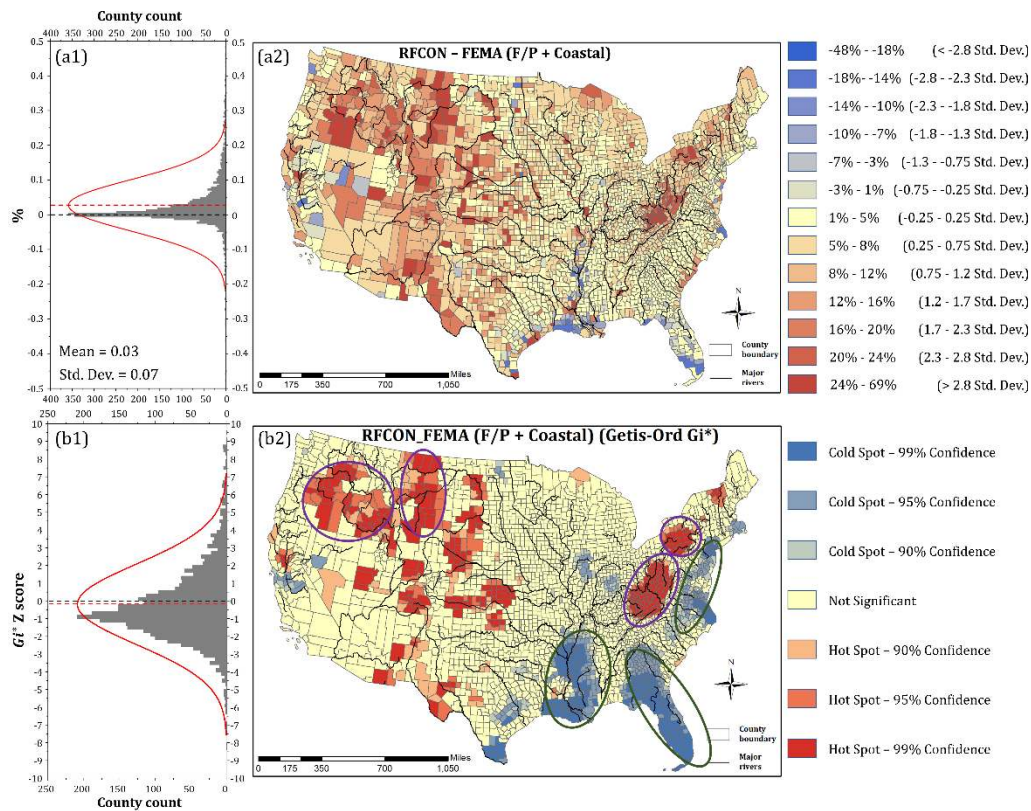


Figure 5.10 County-level differences between exposed population from RFCON and FEMA (F/P + Coastal) in proportion to the county population (a2) associated with county population count histogram (a1); County-level G_i^* Z score distribution (b2) associated with county population count histogram (b1).

5.5 DISCUSSION

This chapter aims to provide the benchmark information regarding the current flood exposure (100-year flood) in the CONUS utilizing a recently released national building footprint dataset and the 2013-2017 ACS estimates. A comparative study is further conducted to examine the flood exposure within FEMA 100-year floodplain boundary and other three publicly available 100-year floodplains.

This study transcends other flood exposure studies in two folds. Firstly, the application of national building footprints provides a spatially explicit population distribution that captures the heterogeneity of population distribution at the micro-level. Previous attempts that estimate regional flood exposure solely rely on the ground-truth population from different levels of geographic units (e.g., census tract, block group, block, etc.). The binary spatial relationship (included or excluded) between floodplain polygons and centroids in those geographic units is usually derived to calculate the exposed population (Crowell et al., 2010; Yager et al., 2017). However, great uncertainties might be introduced if the heterogeneity of population distribution is not well considered. For instance, if a centroid of a block group falls within the identified floodplain, people within the entire block group are assumed to be exposed to the flood risks, which is not necessarily true. Figure 5.11 presents the visual comparison between flood exposure analysis based on centroids of geographic units (Figure 5.11a) and based on building footprints (Figure 5.11b) in an example site in South Carolina. Given the fact that the two block group centroids (circled in blue) are within the FEMA floodplain, residents within the two block groups are all assumed to be exposed, unavoidably leading to great uncertainty in terms of estimating the flood exposure. In comparison, a direct spatial relationship between residential buildings and floodplain greatly aids in summarizing the population residing in flood risk zones as only people living in buildings with flood risks are denoted as exposed population (Figure 5.11b).

Secondly, this study compares the estimations of flood exposure from multiple floodplain products, allowing us to gain a comprehensive understanding of the population facing flood risks in the CONUS. Studies have found that commonly used FEMA

floodplains have numerous limitations, such as their incomprehensiveness (Qiang et al., 2017) and aging issues (Birkland et al., 2003). A great disagreement was also noticed among many floodplain products as they largely vary in extent, particularly in semi-arid zones and wetlands (Trigg et al., 2016). The discrepancy among different floodplain products is explored thoroughly in this study via the investigation of official FEMA floodplain product, a spatially complete FEMA 100-year floodplain, i.e., the RFCON, and two other well-recognized floodplain products, GAR and JRC. This study did not indicate which product is better or more accurate. Rather, the comparative estimations provide general benchmark information regarding the current 100-year flood exposure in the CONUS, enhancing our understanding of how different floodplain products spatially vary in estimations, which could provide advisory information for both local and federal authorities in future policy and decision making.

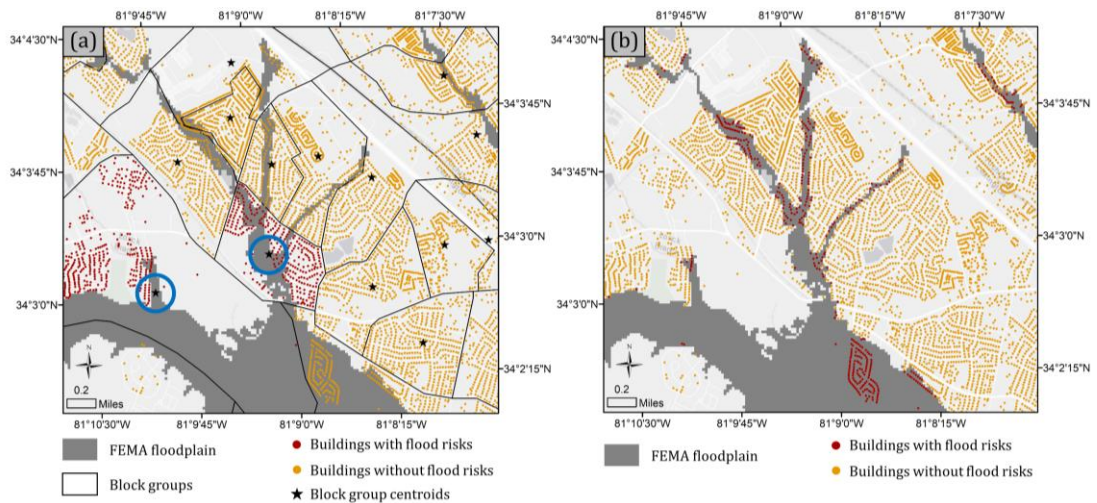


Figure 5.11 Comparison between flood exposure analysis based on centroids of geographic units (block groups) (a) and based on building footprints (b).

FEMA floodplain product has been commonly adopted as an official source of 100-year floodplain coverage in the United States. Based on this product, this chapter estimates that a total of 11.119 million people in the CONUS are facing the danger of 100-year

floods. This number looks less striking than other studies in similar efforts. Using population density data from US Environmental Protection Agency (USEPA), which distributes the 2010 census block population counts into 30m pixels based on land use and slopes, Wang et al. (2018) estimated that 13 million people are exposed to the FEMA 100-year floods. Even more dramatically, Yager et al. (2017) estimated a total of 15 million by calculating the percentage of block centroids covered by FEMA floodplain in each census tract. This chapter reveals that, with the national building footprint product, a better proxy for population distribution than land use and centroids of geographic units, 2 - 4 million fewer people with flood risks are counted in the CONUS.

As assuring as the result might sound, however, the cross-comparison among different floodplain products raises the alarm. Comparing with the estimation from FEMA (F/P) floodplain, estimations from JRC and GAR respectively indicated that 1.099 million and 3.169 million more people are exposed to the flood risks. Similarly, with the inclusion of coastal floods, RFCON estimates 890 thousand more than the estimation from FEMA (F/P + Coastal) floodplain. Two comparisons above reach the same suggestion that FEMA floodplain, potentially limited by its partial coverage, tends to underestimate the flood exposure compared with other sources. This conclusion coincides with the findings from Blessing et al. (2017), who reported the significant mismatch between FEMA's estimated flood loss and the real flood loss. Spatially, estimations from different floodplain products vary. However, an agreement can be reached that JRC, GAR, and RFCON all overestimated the exposed population in the state of Idaho and Montana, compared to the estimation from FEMA. Coincidentally, Idaho and Montana happen to be the states where FEMA floodplains are considerably less available (see the availability of FEMA floodplain

in Figure 5.1), revealing the existence of a large amount of exposed population that failed to be captured by FEMA. In addition, special attention should be paid to the regions where estimations from different floodplains disagree with each other, e.g., regions along the Mississippi River and regions in the Kentucky/West Virginia. Additional research and possibly official data from local authorities may help to shed light on the flood exposure in those regions.

Through the examination of demographic variables in the floodplains, this study also conducts some preliminary examination of environmental justice and social vulnerability on flood hazards in the CONUS. Race and ethnicity are major drivers of flood-related social vulnerability since these may impose cultural and language barriers that affect pre-disaster mitigation and access to post-disaster resources for recovery (Cutter et al., 2003). The results of this chapter indicate that, while estimations from FEMA floodplain suggest no racial bias towards flood exposure, estimations from other floodplains reveal that the white group tends to be more exposed proportionally and the African American group otherwise. The identified racial inequity from other floodplain products agrees with some local studies in Miami (Chakraborty et al., 2014) and in New York City (Maantay and Maroko, 2009). Estimations based on FEMA floodplains found a distinctive higher proportion of Hispanic or Latino group facing flood risks, however, inconclusive results are found in terms of flood exposure on communities of ethnicity, as estimations from different floodplain products show no consistency. Socioeconomic status drivers are among the most prominently measured characteristics in social vulnerability studies (Rufat et al., 2015) and can easily translate into social vulnerability through access to resources, coping behavior, and stress (Adger, 1999). This study explores several

socioeconomic indicators, including unemployment rate, poverty, and tenure status, in response to the flood exposure. No bias is found for the unemployment rate against flood exposure, as the exposed unemployment percentages from all selected floodplains are close to the national statistics. Divergent results are found for the tenure status with flood exposure as estimations vary upon different floodplain products. However, despite small variances, estimations from all selected floodplains reveal that the poor are facing more flood risks than the wealthy. Although the human-flood hazard relationship has been structured with spatial heterogeneity (Maldonado et al., 2016), the inequitable flood risk experienced by the poor in the CONUS, identified by all selected floodplains, emphasizes the importance for future environmental justice and hazard vulnerability studies to emphasize the need for the vulnerable groups.

This study suggests FEMA prioritize improving floodplain identification spatially and temporally to provide the public with a reliable and up-to-date rendering of their true flood exposure, ensuring that NFIP rates reflect the real risk of flooding. High attention should be paid to regions where floodplain maps are unavailable (mostly located in the Mountain States), as the results reveal a large potentially uncaptured population with flood risks in those regions. As of December 2016, the “New, Valid, or Updated Engineering (NVUE)” rate of FEMA was at 42%, meaning that only 42 percent of the NFIP’s maps adequately identified the level of flood risk (Office of Inspector General, 2017). Therefore, the necessity of accurate, complete, up-to-date, and publicly available flood hazard maps is obvious. The FEMA’s MMS program has been taking place, and its continuation is essential for local communities and various stakeholders as it provides updated NIFP maps that reflect the dynamics of flood hazards, encouraging wise community-based floodplain

management and improved citizens' flood hazard awareness. The statistical results also reveal that the poor group experiences heightened exposure to flood risks, which is a particular concern due to their generally reduced capacities to prepare for, respond to, and recover from flood events (Chakraborty et al., 2014). Measures should be taken as the concentration of socially vulnerable groups at high risks potentially increases the pressure to mitigate severe flood events in a significant way.

The NFIP flood insurance rates should continue to be subsidized for groups residing in flood risks zones, especially with lower income, who otherwise are incapable of paying the increased rates. It should be noted that the conclusion at the national level should not be regionalized without caution. An opposite example is Miami, where a study found that the wealthy appear inclined, rather than disinclined, to place themselves at risk to flooding in exchange for the benefits that come with the risk, as the flood insurance is available to externalize the economic risks of flooding (Maldonado et al., 2016). However, the nationwide inequitable flood risk faced by the poor identified in this study should raise the alarm for the federal as well as the local government.

Finally, it is important to recognize several limitations of this study for the benefit of exploring related avenues for future research. Firstly, the limitations of the nationwide Microsoft building footprints are worth mentioning. The Microsoft building footprint product used in this study does not contain building height information. Uncertainty is inevitably introduced when the census population is disaggregated into those buildings due to the lack of information in the vertical dimension. Although the Microsoft building footprint dataset, released in June 2018, is believed to be the most up-to-date and comprehensive building footprint dataset in the U.S, its vintage depends on the underlying

Bing Imagery. Despite the fact that the Bing Map team extracted the footprints using their most up-to-date high-resolution imagery, it is still difficult to know the exact dates for individual pieces of data (Microsoft, 2019). The temporal ambiguity in the dataset might cause problems for studies that require certain temporal restrictions. Secondly, the spatial disparities (estimated via Getis-Ord G_i^*) in flood exposure from different floodplain products are estimated at the county-level, as counties usually share similar political and governmental functions. However, changes in aggregated units (e.g., from counties to grids or from counties to states) might alter the resulted spatial conclusions due to the famous Modifiable Areal Unit Problem (MAUP) (details in Fotheringham and Wong (1991)), a fundamentally unsolvable issue in spatial statistics. Therefore, caution is advised when extrapolating the spatial findings in this study to studies with other spatial units or scales. Thirdly, despite that the Getis-Ord G_i^* statistic can identify significant spatial patterns by investigating the similarity of a certain feature with its neighboring features, it fails to distinguish on a global scale which hot/cold spot clusters have the higher/lower values compared with other hot/cold spots (Songchitruksa and Zeng, 2010). That is, Getis-Ord G_i^* statistic highlights the county-level disparities in exposure estimations from multiple floodplains via identified hot/cold spots but fails to prioritize them. Lastly, the comparative assessment of the exposed population in this study is limited to several selected floodplains with only 1% of annual exceedance probability. Comparison among more floodplain products with various flood risk levels (i.e., 500- year flood) is needed.

5.6 CONCLUDING REMARKS

This chapter improves the estimation of the population in floodplains by considering its spatial heterogeneity within census units and provides a comparative assessment of the

population exposed to flood hazards for the entire Conterminous United States. Unlike other studies, this study utilizes the latest national building footprints, recently open-sourced by the Microsoft Bing Map team in 2018, to capture the heterogeneity of population distribution at the micro-level. To better quantify the exposure, the population in block groups from the ACS 5-year estimates (2013-2017) is disaggregated to residential buildings, identified from NLUD 2010 and OpenStreetMap Land Use polygons. A comparative study is then conducted by examining the 100-year flood exposure from FEMA and from the other three publicly available 100-year floodplains, i.e., JRC, GAR, and RECON.

Based on the FEMA floodplain (both F/P and coastal), the results suggest that 11.119 million people in the CONUS are currently facing the 100-year flood risk. The other three selected floodplains, however, all reveal higher numbers than the estimation from FEMA. From a spatial perspective, estimations from other floodplain products suggest that a large population of residents are found in regions where FEMA floodplain product is unavailable, indicating that FEMA potentially underestimates the exposure in those regions, presumably responsible for the uncaptured losses reported from other studies. Attention should be paid to regions where estimations from different floodplains disagree with each other, especially the Lower Mississippi River.

Through the examination of racial/ethnic and socioeconomic variables in the geographic distribution of flood exposure, the results indicate that the low-income people are facing higher flood risks than the wealthy in the floodplain. Despite that some local case studies indicate otherwise, the inequitable flood risk experienced by the poor revealed across the CONUS underscores the significance of future hazard vulnerability studies to

emphasize the need for this vulnerable group. Meanwhile, divergent results are found in terms of flood exposure on communities of ethnicity, as estimations from different floodplain products show no consistency. In light of the inconsistency among the selected floodplains in the exposure analysis, FEMA should continue its MMS program to provide the public with reliable, up-to-date floodplain maps and ensure that NFIP rates reflect the real risk of flooding.

The benchmark information regarding the 100-year flood exposure and the knowledge of how different floodplain products vary spatially in exposure analysis greatly enhance our understanding of the current flood risks in the CONUS, largely benefiting both local and federal authorities for future policymaking.

CHAPTER 6

CONCLUSIONS

Flood, one of the most common natural hazards on Earth, poses great threats to a large amount of population in the world. As the severity and frequency of flood events have noticeably increased in the U.S, improving flood awareness and exposure analysis for better flood mitigation strategy is in great need. Fortunately, innovative spatial algorithms and data sources have flourished in the emerging Big Data Era.

This dissertation focuses on obtaining improved flood awareness and exposure analysis through innovative geospatial analytics, taking advantage of Big Data technologies. The improved flood awareness is achieved via a data fusion enabled (Chapter 2) and deep learning supported (Chapter 3) flood monitoring framework that systematically integrates a variety of heterogeneous data sources, including satellite imagery, water gauges, and crowdsourcing platforms. The improved exposure assessment is achieved via the application of nighttime remote sensing series for estimating hurricane exposure in U.S Atlantic/Gulf coasts (Chapter 4) and a comparative assessment of the exposed population within 100-year floodplains in the entire CONUS (Chapter 5).

Chapter 2 builds a flood inundation reconstruction model by enhancing the NRT normalized difference water index (NDWI) derived from remote sensing imagery with the RT data, including stream gauge readings and social media (tweets). Splitting into three modules: water height module, global enhancement module, and local enhancement module, the proposed model first incorporates the gauge readings and the NDWI image to

reconstruct a macroscale flood probability layer, which is then locally enhanced using the verified flood-related tweets. The final output of the model matches well with the USGS inundation map and its surveyed high-water marks. Results suggest that by enhancing NRT imagery with RT data sources, the proposed flood inundation probability reconstruction model renders a more robust, spatially enhanced flood probability index for emergency responders to quickly identify areas in need of urgent attention. The study in this chapter proves the feasibility of fusing heterogeneous data sources in a flood event, leading to enhanced flood awareness in a near real-time manner. However, retrieving flood relevant posts remains a great challenge, as on-topic social media posts only comprise a small proportion of the enormous volume of information in social media space. The method of retrieving flood relevant posts in this chapter (keyword-matching coupled with manual verification) is rather time/labor-consuming. Thus, an automatic approach to retrieve on-topic social media posts is in great need.

Chapter 3 solves the remaining problem in Chapter 2 by presenting an automatic approach to labeling on-topic social media posts using visual-textual fused features. Two convolutional neural networks (CNNs), Inception-V3 CNN and word embedded CNN, are applied to extract visual and textual features respectively from social media posts. Well-trained on our training sets, the extracted visual and textual features are further concatenated to form a fused feature to feed the final classification process. The results suggest that both CNNs perform remarkably well in learning visual and textual features. The fused feature proves that additional visual feature leads to more robustness compared with the situation where only the textual feature is used. The on-topic posts, classified by their texts and pictures automatically, represent timely disaster documentation during an

event. Coupling with rich spatial contexts when geotagged, social media could greatly aid in a variety of disaster mitigation approaches. The proposed visual-textual CNN architecture significantly automates the on-topic social media retrieval, largely expanding searching scope, ensuring more robustness of classification, and seeding a wide range of social media based disaster studies. Chapter 2 and Chapter 3 form a deep learning multi-source flood monitoring framework, which can be applied to other flooding cases in the future. The continuous input of socially sensed information via the approach designed in Chapter 3 can be fused with river gauge readings and temporal-discrete remotely sensed images via the model designed in Chapter 2, enabling the framework to monitor flood at different flooding phases, providing uninterrupted situational awareness that greatly benefits local authorities and first responders.

Chapter 4 delves into the perspective of flood exposure of human settlement in a broader geographic context. This chapter investigated the long-term human settlement development in response to frequent hurricane hits in the U.S Atlantic/Gulf Coasts, given that many floods in the U.S are hurricane-induced. A better understanding of the spatiotemporal dynamics of human settlement in hurricane-prone areas largely benefits sustainable development. The study in Chapter 4 used the nighttime light (NTL) data from the Defense Meteorological Satellite Program's Operational Linescan System (DMSP/OLS) to examine human settlement development in areas with different levels of hurricane proneness from 1992 to 2013. A popular index that quantifies human settlement intensity, Vegetation Adjusted NTL Urban Index (VANUI), was derived and examined with the Mann–Kendall test and Theil–Sen test to identify significant spatiotemporal trends. The results clearly exhibit a north-south and inland-coastal discrepancy of human

settlement dynamics and reveal that both the zonal extent and zonal increase rate of human settlement positively correlate with hurricane proneness levels. The ongoing intensification of anthropogenic environmental changes coupled with more frequent and severe hurricanes is likely to cast more pressure on coastal resilience, potentially leading to severer damage caused by hurricane-induced floods. The spatiotemporal changes of human settlement revealed from nighttime remote sensing in hurricane-prone areas provide valuable information to evaluate the hurricane-induced damages and to support decision making of future urban development.

Lastly, Chapter 5 further extends the study in Chapter 4 and obtains baseline information about flood risk perception by quantifying the general exposure of floods in the entire CONUS and assessing its impact on those likely to bear the eventual cost of flooding. In light of the limitations of previous flood exposure studies in the U.S, this chapter used the recently released Microsoft building footprint dataset to capture the heterogeneity of population distribution at the micro-level. The population at block group level from ACS 5-year estimates (2013-2017) was further disaggregated to residential buildings, identified via NLUD 2010 and OpenStreetMap Land Use polygons. A comparative study was then conducted to investigate the 100-year flood exposure from FEMA and from the other three publicly available 100-year floodplains. Although the exposure analysis shows varying spatial patterns for selected floodplains, it indicates that a large number of exposed residents are found in regions where FEMA floodplain product is unavailable, presumably responsible for the uncaptured losses reported from other studies. In addition, the inequitably high flood risk experienced by the poor revealed at the national level underscores the significance of flood vulnerability studies to emphasize the

need for this vulnerable group. The benchmark information regarding the 100-year flood exposure and the knowledge of how different floodplain products vary spatially in exposure analysis greatly enhance our understanding of the current flood risks in the CONUS, largely benefiting both local and federal authorities for future policymaking.

With this dissertation research, I have gained rich set of theoretical, methodological, and contextual knowledge of how to obtain better flood awareness and how to achieve comprehensive exposure analysis for flooding events in the Big Data Era. It greatly advances the flood-related studies by proving the possibility of fusing heterogeneous data sources for enhanced flooding situational awareness, illustrating the efficacy of using deep learning algorithms for automating on-topic crowdsourcing data retrieval, demonstrating the application of nighttime remote sensing in hurricane-induced disaster exposure analysis for the U.S coastal regions, and benchmarking the current 100-year flood exposure in the entire CONUS via nationwide building footprints. The methodologies and results presented in this dissertation greatly benefit local authorities and the federal government for mitigating both short-term and long-term flood-induced damages.

REFERENCES

- Adger, W. N. (1999). Social vulnerability to climate change and extremes in coastal Vietnam. *World development*, 27(2), 249-269.
- Ashktorab, Z., Brown, C., Nandi, M., & Culotta, A. (2014, May). Tweedr: Mining twitter to inform disaster response. In ISCRAM.
- Avgerinakis, K., Moumtzidou, A., Andreadis, S., Michail, E., Gialampoukidis, I., Vrochidis, S., & Kompatsiaris, I. (2017). Visual and textual analysis of social media and satellite images for flood detection@ multimedia satellite task MediaEval 2017. In *Working Notes Proc. MediaEval Workshop* (p. 2).
- Avvenuti, M., Cresci, S., Del Vigna, F., & Tesconi, M. (2016). Impromptu crisis mapping to prioritize emergency response. *Computer*, 49(5), 28-37.
- Avvenuti, M., Cresci, S., Del Vigna, F., Fagni, T., & Tesconi, M. (2018). CrisMap: a big data crisis mapping system based on damage detection and geoparsing. *Information Systems Frontiers*, 1-19.
- Avvenuti, M., Cresci, S., Marchetti, A., Meletti, C., & Tesconi, M. (2014, August). EARS (earthquake alert and report system): a real time decision support system for earthquake crisis management. In *Proceedings of the 20th ACM SIGKDD international conference on knowledge discovery and data mining* (pp. 1749-1758). ACM.
- Avvenuti, M., Cresci, S., Nizzoli, L., & Tesconi, M. (2018, June). GSP (Geo-Semantic-Parsing): geoparsing and geotagging with machine learning on top of linked data. In *European Semantic Web Conference* (pp. 17-32). Springer, Cham.
- Bakillah, M., Li, R. Y., & Liang, S. H. (2015). Geo-located community detection in Twitter with enhanced fast-greedy optimization of modularity: the case study of typhoon Haiyan. *International Journal of Geographical Information Science*, 29(2), 258-279.
- Bar, Y., Diamant, I., Wolf, L., & Greenspan, H. (2015, March). Deep learning with non-medical training used for chest pathology identification. In *Medical Imaging 2015: Computer-Aided Diagnosis* (Vol. 9414, p. 94140V). International Society for Optics and Photonics.

- Berg, R. (2016) "National Hurricane Center Tropical Cyclone Report. Hurricane Joaquin (AL112015)", NOAA. Retrieved from:
https://www.nhc.noaa.gov/data/tcr/AL112015_Joaquin.pdf
- Bernhofen, M. V., Whyman, C., Trigg, M. A., Sleigh, P. A., Smith, A. M., Sampson, C. C., ... & Dottori, F. (2018). A first collective validation of global fluvial flood models for major floods in Nigeria and Mozambique. *Environmental Research Letters*, 13(10), 104007.
- Birkland, T. A., Burby, R. J., Conrad, D., Cortner, H., & Michener, W. K. (2003). River ecology and flood hazard mitigation. *Natural Hazards Review*, 4(1), 46-54.
- Bischke, B., Bhardwaj, P., Gautam, A., Helber, P., Borth, D., & Dengel, A. (2017). Detection of flooding events in social multimedia and satellite imagery using deep neural networks. In *Working Notes Proc. MediaEval Workshop* (p. 2).
- Blessing, R., Sebastian, A., & Brody, S. D. (2017). Flood risk delineation in the United States: how much loss are we capturing? *Natural Hazards Review*, 18(3), 04017002.
- Bojanowski, P., Grave, E., Joulin, A., & Mikolov, T. (2017). Enriching word vectors with subword information. *Transactions of the Association for Computational Linguistics*, 5, 135-146.
- Bosch, A., Zisserman, A., & Munoz, X. (2007, October). Image classification using random forests and ferns. In *Computer Vision, 2007. ICCV 2007. IEEE 11th International Conference on* (pp. 1-8). IEEE.
- Brivio, P. A., Colombo, R., Maggi, M., & Tomasoni, R. (2002). Integration of remote sensing data and GIS for accurate mapping of flooded areas. *International Journal of Remote Sensing*, 23(3), 429-441.
- Burby, R. J., Bollens, S. A., Holloway, J. M., Kaiser, E. J., Mullan, D., & Sheaffer, J. R. (1988). Cities under water: A comparative evaluation of ten cities' efforts to manage floodplain land use. In *Cities under water: A comparative evaluation of ten cities' efforts to manage floodplain land use*. US University of Colorado. Institute of Behavioral Science. Program on Environment and Behavior.
- Ceola, S., Laio, F., & Montanari, A. (2014). Satellite nighttime lights reveal increasing human exposure to floods worldwide. *Geophysical Research Letters*, 41(20), 7184-7190.
- Ceola, S., Laio, F., & Montanari, A. (2015). Human-impacted waters: New perspectives from global high-resolution monitoring. *Water Resources Research*, 51(9), 7064-7079.
- Cervone, G., Sava, E., Huang, Q., Schnebele, E., Harrison, J., & Waters, N. (2016). Using Twitter for tasking remote-sensing data collection and damage assessment:

- 2013 Boulder flood case study. *International Journal of Remote Sensing*, 37(1), 100-124.
- Chakraborty, J., Collins, T. W., Montgomery, M. C., & Grineski, S. E. (2014). Social and spatial inequities in exposure to flood risk in Miami, Florida. *Natural Hazards Review*, 15(3), 04014006.
- Chand, T. K., Badarinath, K. V. S., Elvidge, C. D., & Tuttle, B. T. (2009). Spatial characterization of electrical power consumption patterns over India using temporal DMSP-OLS night-time satellite data. *International Journal of Remote Sensing*, 30(3), 647-661.
- Chapelle, O., Haffner, P., & Vapnik, V. N. (1999). Support vector machines for histogram-based image classification. *IEEE transactions on Neural Networks*, 10(5), 1055-1064.
- Cheng, Z., Caverlee, J., & Lee, K. (2010, October). You are where you tweet: a content-based approach to geo-locating twitter users. In *Proceedings of the 19th ACM international conference on Information and knowledge management* (pp. 759-768). ACM.
- Chenoweth, M., & Landsea, C. (2004). The San Diego Hurricane of 2 October 1858. *Bulletin of the American Meteorological Society*, 85(11), 1689-1698.
- Ciresan, D. C., Meier, U., Masci, J., Maria Gambardella, L., & Schmidhuber, J. (2011, July). Flexible, high performance convolutional neural networks for image classification. In *IJCAI Proceedings-International Joint Conference on Artificial Intelligence* (Vol. 22, No. 1, p. 1237).
- Collobert, R., Weston, J., Bottou, L., Karlen, M., Kavukcuoglu, K., & Kuksa, P. (2011). Natural language processing (almost) from scratch. *Journal of Machine Learning Research*, 12(Aug), 2493-2537.
- Crampton, J. W. (2009). Cartography: maps 2.0. *Progress in Human Geography*, 33(1), 91-100.
- Crossett, K. M., Culliton, T. J., Wiley, P. C., & Goodspeed, T. R. (2004). Population trends along the coastal United States: 1980-2008 (Vol. 55). US Department of Commerce, National Oceanic and Atmospheric Administration, National Ocean Service, Management and Budget Office, Special Projects.
- Crowell, M., Coulton, K., Johnson, C., Westcott, J., Bellomo, D., Edelman, S., & Hirsch, E. (2010). An estimate of the US population living in 100-year coastal flood hazard areas. *Journal of Coastal Research*, 201-211.
- Cutter, S. L., Boruff, B. J., & Shirley, W. L. (2003). Social vulnerability to environmental hazards. *Social science quarterly*, 84(2), 242-261.

- de Jong, R., de Bruin, S., de Wit, A., Schaepman, M. E., & Dent, D. L. (2011). Analysis of monotonic greening and browning trends from global NDVI time-series. *Remote Sensing of Environment*, 115(2), 692-702.
- Dmowska, A., & Stepinski, T. F. (2017). A high resolution population grid for the conterminous United States: The 2010 edition. *Computers, Environment and Urban Systems*, 61, 13-23.
- Doll, C. H., Muller, J. P., & Elvidge, C. D. (2000). Night-time imagery as a tool for global mapping of socioeconomic parameters and greenhouse gas emissions. *AMBIO: a Journal of the Human Environment*, 29(3), 157-162.
- Dottori, Francesco; Alfieri, Lorenzo; Salamon, Peter; Bianchi, Alessandra; Feyen, Luc; Hirpa, Feyera (2016): Flood hazard map of the World - 100-year return period. European Commission, Joint Research Centre (JRC) [Dataset]
PID: http://data.europa.eu/89h/jrc-floods-floodmapgl_rp100y-tif
- Douben, K. J. (2006). Characteristics of river floods and flooding: a global overview, 1985–2003. *Irrigation and drainage*, 55(S1), S9-S21.
- Dredze, M. (2012). How social media will change public health. *IEEE Intelligent Systems*, 27(4), 81-84.
- Earle, P. S., Bowden, D. C., & Guy, M. (2012). Twitter earthquake detection: earthquake monitoring in a social world. *Annals of Geophysics*, 54(6).
- Elvidge, C. D., Baugh, K. E., Dietz, J. B., Bland, T., Sutton, P. C., & Kroehl, H. W. (1999). Radiance calibration of DMSP-OLS low-light imaging data of human settlements. *Remote Sensing of Environment*, 68(1), 77-88.
- Elvidge, C. D., Baugh, K. E., Zhizhin, M., & Hsu, F. C. (2013). Why VIIRS data are superior to DMSP for mapping nighttime lights. *Proceedings of the Asia-Pacific Advanced Network*, 35(62).
- Elvidge, C. D., Ziskin, D., Baugh, K. E., Tuttle, B. T., Ghosh, T., Pack, D. W., ... & Zhizhin, M. (2009). A fifteen year record of global natural gas flaring derived from satellite data. *Energies*, 2(3), 595-622.
- Elvidge, C., Baugh, K., Hobson, V., Kihn, E., Kroehl, H., Davis, E., & Cocero, D. (1997). Satellite inventory of human settlements using nocturnal radiation emissions: a contribution for the global toolchest. *Global Change Biology*, 3(5), 387-395.
- Fang, Y., Du, S., Scussolini, P., Wen, J., He, C., Huang, Q., & Gao, J. (2018). Rapid population growth in Chinese floodplains from 1990 to 2015. *International journal of environmental research and public health*, 15(8), 1602.

- Fazeli, H. R., Said, M. N., Amerudin, S., & Rahman, M. Z. A. (2015). A study of volunteered geographic information (VGI) assessment methods for flood hazard mapping: A review. *Jurnal Teknologi*, 75(10).
- Feaster, T. D., Shelton, J. M., & Robbins, J. C. (2015). Preliminary peak stage and streamflow data at selected USGS streamgaging stations for the South Carolina flood of October 2015 (No. 2015-1201). US Geological Survey.
- Federal Emergency Management Agency (FEMA), 2019. Flood zones [online]. Available from: <https://www.fema.gov/flood-zones>
- Feick, R., & Roche, S. (2013). Understanding the Value of VGI. In *Crowdsourcing geographic knowledge* (pp. 15-29). Springer, Dordrecht.
- Feng, Y., & Sester, M. (2018). Extraction of pluvial flood relevant volunteered geographic information (VGI) by deep learning from user generated texts and photos. *ISPRS International Journal of Geo-Information*, 7(2), 39.
- Fernandes, R., & Leblanc, S. G. (2005). Parametric (modified least squares) and non-parametric (Theil–Sen) linear regressions for predicting biophysical parameters in the presence of measurement errors. *Remote Sensing of Environment*, 95(3), 303-316.
- Fohringer, J., Dransch, D., Kreibich, H., & Schröter, K. (2015). Social media as an information source for rapid flood inundation mapping. *Natural Hazards and Earth System Sciences (NHESS)*, 15, 2725-2738.
- Fotheringham, A. S., & Wong, D. W. (1991). The modifiable areal unit problem in multivariate statistical analysis. *Environment and planning A*, 23(7), 1025-1044.
- Frey, W. H. (2019). “U.S. growth rate hits new low as migration to the Sun Belt continues”. Retrieved from: <https://www.brookings.edu/blog/the-avenue/2016/12/23/u-s-growth-rate-hits-new-low-as-migration-to-the-sun-belt-continues/>.
- Gao, B. C. (1996). NDWI—A normalized difference water index for remote sensing of vegetation liquid water from space. *Remote sensing of environment*, 58(3), 257-266.
- Gao, Y., Wang, M., Zha, Z. J., Shen, J., Li, X., & Wu, X. (2013). Visual-textual joint relevance learning for tag-based social image search. *IEEE Transactions on Image Processing*, 22(1), 363-376.
- Gao, Y., Wang, S., Padmanabhan, A., Yin, J., & Cao, G. (2018). Mapping spatiotemporal patterns of events using social media: a case study of influenza trends. *International Journal of Geographical Information Science*, 32(3), 425-449.

- Gaquin, D. A., & Ryan, M. M. (Eds.). (2018). *The Who, What, and where of America: Understanding the American Community Survey*. Rowman & Littlefield.
- Getis, A., & Ord, J. K. (2010). The analysis of spatial association by use of distance statistics. In *Perspectives on Spatial Data Analysis* (pp. 127-145). Springer, Berlin, Heidelberg.
- Ghosh, T., L Powell, R., D Elvidge, C., E Baugh, K., C Sutton, P., & Anderson, S. (2010). Shedding light on the global distribution of economic activity. *The Open Geography Journal*, 3(1).
- Goldenberg, S. B., Landsea, C. W., Mestas-Nuñez, A. M., & Gray, W. M. (2001). The recent increase in Atlantic hurricane activity: Causes and implications. *Science*, 293(5529), 474-479.
- Goodchild, M. F. (2007). Citizens as sensors: the world of volunteered geography. *GeoJournal*, 69(4), 211-221.
- Gupta, A., Lamba, H., Kumaraguru, P., & Joshi, A. (2013, May). Faking sandy: characterizing and identifying fake images on twitter during hurricane sandy. In *Proceedings of the 22nd international conference on World Wide Web* (pp. 729-736). ACM.
- Hannak, A., Anderson, E., Barrett, L. F., Lehmann, S., Mislove, A., & Riedewald, M. (2012, June). Tweetin'in the Rain: Exploring Societal-Scale Effects of Weather on Mood. In *ICWSM*.
- Haworth, B., & Bruce, E. (2015). A review of volunteered geographic information for disaster management. *Geography Compass*, 9(5), 237-250.
- He, K., Zhang, X., Ren, S., & Sun, J. (2016). Deep residual learning for image recognition. In *Proceedings of the IEEE conference on computer vision and pattern recognition* (pp. 770-778).
- Hershey, S., Chaudhuri, S., Ellis, D. P., Gemmeke, J. F., Jansen, A., Moore, R. C., ... & Slaney, M. (2017, March). CNN architectures for large-scale audio classification. In *2017 IEEE International Conference on Acoustics, Speech and Signal Processing (ICASSP)* (pp. 131-135). IEEE.
- Hochreiter, S., & Schmidhuber, J. (1997). Long short-term memory. *Neural computation*, 9(8), 1735-1780.
- Hogan, T. D. (1987). Determinants of the seasonal migration of the elderly to sunbelt states. *Research on Aging*, 9(1), 115-133.
- Horita, F. E., de Albuquerque, J. P., Degrossi, L. C., Mendiondo, E. M., & Ueyama, J. (2015). Development of a spatial decision support system for flood risk

- management in Brazil that combines volunteered geographic information with wireless sensor networks. *Computers & Geosciences*, 80, 84-94.
- Hsu, F. C., Baugh, K. E., Ghosh, T., Zhizhin, M., & Elvidge, C. D. (2015). DMSP-OLS radiance calibrated nighttime lights time series with intercalibration. *Remote Sensing*, 7(2), 1855-1876.
- Hu, F., Xia, G. S., Hu, J., & Zhang, L. (2015). Transferring deep convolutional neural networks for the scene classification of high-resolution remote sensing imagery. *Remote Sensing*, 7(11), 14680-14707.
- Huang, X., Li, Z., Wang, C., & Ning, H. (2019a). Identifying disaster related social media for rapid response: a visual-textual fused CNN architecture. *International Journal of Digital Earth*, 1-23.
- Huang, X., Schneider, A., & Friedl, M. A. (2016). Mapping sub-pixel urban expansion in China using MODIS and DMSP/OLS nighttime lights. *Remote Sensing of Environment*, 175, 92-108.
- Huang, X., Wang, C., & Li, Z. (2018a). A near real-time flood-mapping approach by integrating social media and post-event satellite imagery. *Annals of GIS*, 24(2), 113-123.
- Huang, X., Wang, C., & Li, Z. (2018b). Reconstructing Flood Inundation Probability by Enhancing Near Real-Time Imagery with Real-Time Gauges and Tweets. *IEEE Transactions on Geoscience and Remote Sensing*, DOI: 10.1109/TGRS.2018.2835306
- Huang, X., Wang, C., & Li, Z. (2019b). Linking picture with text: tagging flood relevant tweets for rapid flood inundation mapping. *PrICA*, 2, 45.
- Huang, X., Wang, C., & Li, Z. (2019e, November). High-resolution population grid in the CONUS using microsoft building footprints: a feasibility study. In *Proceedings of the 3rd ACM SIGSPATIAL International Workshop on Geospatial Humanities* (pp. 1-9).
- Huang, X., Wang, C., & Lu, J. (2019c). Understanding the spatiotemporal development of human settlement in hurricane-prone areas on the US Atlantic and Gulf coasts using nighttime remote sensing. *Natural Hazards and Earth System Sciences*, 19(10), 2141-2155.
- Huang, X., Wang, C., Li, Z., & Ning, H. (2018c). A visual-textual fused approach to automated tagging of flood-related tweets during a flood event. *International Journal of Digital Earth*, DOI: 10.1080/17538947.2018.1523956
- Huang, X., Xu, D., Li, Z., & Wang, C. (2019d). Translating multispectral imagery to nighttime imagery via conditional generative adversarial networks. arXiv preprint arXiv:2001.05848.

- Iceland, J., Sharp, G., & Timberlake, J. M. (2013). Sun Belt rising: Regional population change and the decline in black residential segregation, 1970–2009. *Demography*, 50(1), 97-123.
- Imhoff, M. L., Lawrence, W. T., Stutzer, D. C., & Elvidge, C. D. (1997). A technique for using composite DMSP/OLS “city lights” satellite data to map urban area. *Remote Sensing of Environment*, 61, 361-370.
- Imran, M., Castillo, C., Diaz, F., & Vieweg, S. (2015). Processing social media messages in mass emergency: A survey. *ACM Computing Surveys (CSUR)*, 47(4), 67.
- Jackson, S. P., Mullen, W., Agouris, P., Crooks, A., Croitoru, A., & Stefanidis, A. (2013). Assessing completeness and spatial error of features in volunteered geographic information. *ISPRS International Journal of Geo-Information*, 2(2), 507-530.
- Jain, S. K., Saraf, A. K., Goswami, A., & Ahmad, T. (2006). Flood inundation mapping using NOAA AVHRR data. *Water Resources Management*, 20(6), 949-959.
- Jain, S. K., Singh, R. D., Jain, M. K., & Lohani, A. K. (2005). Delineation of flood-prone areas using remote sensing techniques. *Water Resources Management*, 19(4), 333-347.
- Joyce, K. E., Belliss, S. E., Samsonov, S. V., McNeill, S. J., & Glassey, P. J. (2009). A review of the status of satellite remote sensing and image processing techniques for mapping natural hazards and disasters. *Progress in Physical Geography*, 33(2), 183-207.
- Kalchbrenner, N., Grefenstette, E., & Blunsom, P. (2014). A convolutional neural network for modelling sentences. *arXiv preprint arXiv:1404.2188*.
- Kent, J. D., & Capello Jr, H. T. (2013). Spatial patterns and demographic indicators of effective social media content during the Horseshoe Canyon fire of 2012. *Cartography and Geographic Information Science*, 40(2), 78-89.
- Kim, Y. (2014). Convolutional neural networks for sentence classification. *arXiv preprint arXiv:1408.5882*.
- Klotzbach, P. J., Bowen, S. G., Pielke Jr, R., & Bell, M. (2018). Continental US hurricane landfall frequency and associated damage: Observations and future risks. *Bulletin of the American Meteorological Society*, 99(7), 1359-1376.
- Krizhevsky, A., Sutskever, I., & Hinton, G. E. (2012). Imagenet classification with deep convolutional neural networks. In *Advances in neural information processing systems* (pp. 1097-1105).

- Krupa, M. (2018). "Hurricane Florence's toll on US homes and businesses has now hit 11 figures". Retrieved from: <https://www.cnn.com/2018/10/07/us/florence-storm-damage-estimates/index.html>.
- Kyba, C. C., Kuester, T., De Miguel, A. S., Baugh, K., Jechow, A., Hölker, F., ... & Guanter, L. (2017). Artificially lit surface of Earth at night increasing in radiance and extent. *Science advances*, 3(11), e1701528.
- Lamos, V., & Cristianini, N. (2012). Nowcasting events from the social web with statistical learning. *ACM Transactions on Intelligent Systems and Technology (TIST)*, 3(4), 72.
- Landsea, C. W., Vecchi, G. A., Bengtsson, L., & Knutson, T. R. (2010). Impact of duration thresholds on Atlantic tropical cyclone counts. *Journal of Climate*, 23(10), 2508-2519.
- Laura, L. F., Joost, W., Marc, B., & Harald, S. (2017). Multi-modal deep learning approach for flood detection. In *Proceedings of the MediaEval. Workshop, Dublin Google Scholar*.
- Letu, H., Hara, M., Yagi, H., Naoki, K., Tana, G., Nishio, F., & Shuhei, O. (2010). Estimating energy consumption from night-time DMPS/OLS imagery after correcting for saturation effects. *International Journal of Remote Sensing*, 31(16), 4443-4458.
- Levy, J. K., Hartmann, J., Li, K. W., An, Y., & Asgary, A. (2007). Multi-criteria decision support systems for flood hazard mitigation and emergency response in urban watersheds 1. *JAWRA Journal of the American Water Resources Association*, 43(2), 346-358.
- Lew, M. S., Sebe, N., Djeraba, C., & Jain, R. (2006). Content-based multimedia information retrieval: State of the art and challenges. *ACM Transactions on Multimedia Computing, Communications, and Applications (TOMM)*, 2(1), 1-19.
- Li, X., & Zhou, Y. (2017). Urban mapping using DMSP/OLS stable night-time light: a review. *International Journal of Remote Sensing*, 38(21), 6030-6046.
- Li, Z., Wang, C., Emrich, C. T., & Guo, D. (2018). A novel approach to leveraging social media for rapid flood mapping: a case study of the 2015 South Carolina floods. *Cartography and Geographic Information Science*, 45(2), 97-110.
- Lin, J., Liu, X., Li, K., & Li, X. (2014). A maximum entropy method to extract urban land by combining MODIS reflectance, MODIS NDVI, and DMSP-OLS data. *International Journal of Remote Sensing*, 35(18), 6708-6727.
- Lin, Z., Jin, H., Robinson, B., & Lin, X. (2016). Towards an accurate social media disaster event detection system based on deep learning and semantic representation. In *proceedings of the Australasian Data Mining Conference*.

- Liu, L., & Leung, Y. (2015). A study of urban expansion of prefectural-level cities in South China using night-time light images. *International Journal of Remote Sensing*, 36(22), 5557-5575.
- Liu, X., Hu, G., Ai, B., Li, X., & Shi, Q. (2015). A normalized urban areas composite index (NUACI) based on combination of DMSP-OLS and MODIS for mapping impervious surface area. *Remote Sensing*, 7(12), 17168-17189.
- Liu, Z., He, C., Zhang, Q., Huang, Q., & Yang, Y. (2012). Extracting the dynamics of urban expansion in China using DMSP-OLS nighttime light data from 1992 to 2008. *Landscape and Urban Planning*, 106(1), 62-72.
- Lu, D., Tian, H., Zhou, G., & Ge, H. (2008). Regional mapping of human settlements in southeastern China with multisensor remotely sensed data. *Remote Sensing of Environment*, 112(9), 3668-3679.
- Lu, H., Zhang, C., Liu, G., Ye, X., & Miao, C. (2018). Mapping China's ghost cities through the combination of nighttime satellite data and daytime satellite data. *Remote Sensing*, 10(7), 1037.
- Ma, Q., He, C., Wu, J., Liu, Z., Zhang, Q., & Sun, Z. (2014). Quantifying spatiotemporal patterns of urban impervious surfaces in China: An improved assessment using nighttime light data. *Landscape and Urban Planning*, 130, 36-49.
- Maantay, J., & Maroko, A. (2009). Mapping urban risk: Flood hazards, race, & environmental justice in New York. *Applied Geography*, 29(1), 111-124.
- Maldonado, A., Collins, T. W., Grineski, S. E., & Chakraborty, J. (2016). Exposure to flood hazards in Miami and Houston: are Hispanic immigrants at greater risk than other social groups?. *International journal of environmental research and public health*, 13(8), 775.
- Mallinis, G., Gitas, I. Z., Giannakopoulos, V., Maris, F., & Tsakiri-Strati, M. (2013). An object-based approach for flood area delineation in a transboundary area using ENVISAT ASAR and LANDSAT TM data. *International Journal of Digital Earth*, 6(sup2), 124-136.
- Mann, H. B. (1945). Nonparametric tests against trend. *Econometrica: Journal of the Econometric Society*, 245-259.
- Mather, M., Rivers, K. L., & Jacobsen, L. A. (2005). The American Community Survey. *Population Bulletin*, 60(3), 1-20.
- McCann, S., & Lowe, D. G. (2012, June). Local naive bayes nearest neighbor for image classification. In *Computer Vision and Pattern Recognition (CVPR), 2012 IEEE Conference on* (pp. 3650-3656). IEEE.

- McDougall, K., & Temple-Watts, P. (2012). The use of LIDAR and volunteered geographic information to map flood extents and inundation. *ISPRS Annals of the Photogrammetry, Remote Sensing and Spatial Information Sciences*, 1, 251-256.
- McFeeters, S. K. (1996). The use of the Normalized Difference Water Index (NDWI) in the delineation of open water features. *International journal of remote sensing*, 17(7), 1425-1432.
- Microsoft USBuildingFootprints. (2018). Retrieved from <https://github.com/Microsoft/USBuildingFootprints>
- Microsoft. (2019, March 04). Microsoft/USBuildingFootprints. Retrieved from <https://github.com/Microsoft/USBuildingFootprints>
- Middleton, S. E., Middleton, L., & Modafferi, S. (2014). Real-time crisis mapping of natural disasters using social media. *IEEE Intelligent Systems*, 29(2), 9-17.
- Mikolov, T., Chen, K., Corrado, G., & Dean, J. (2013). Efficient estimation of word representations in vector space. *arXiv preprint arXiv:1301.3781*.
- Mikolov, T., Karafiát, M., Burget, L., Černocký, J., & Khudanpur, S. (2010). Recurrent neural network based language model. In *Eleventh annual conference of the international speech communication association*.
- Milesi, C., Elvidge, C. D., Nemani, R. R., & Running, S. W. (2003). Assessing the impact of urban land development on net primary productivity in the southeastern United States. *Remote Sensing of Environment*, 86(3), 401-410.
- Muralidharan, S., Rasmussen, L., Patterson, D., & Shin, J. H. (2011). Hope for Haiti: An analysis of Facebook and Twitter usage during the earthquake relief efforts. *Public Relations Review*, 37(2), 175-177.
- Murphy, J. D. (2015). "The Historic South Carolina Floods of October 1-5, 2015", National Weather Service, Silver Spring, Maryland. Retrieved from: https://www.weather.gov/media/publications/assessments/SCFlooding_072216_Signed_Final.pdf
- Musser, J. W., Watson, K. M., Painter, J. A., & Gotvald, A. J. (2016). Flood-inundation maps of selected areas affected by the flood of October 2015 in central and coastal South Carolina (No. 2016-1019). US Geological Survey.
- Neumann, B., Vafeidis, A. T., Zimmermann, J., & Nicholls, R. J. (2015). Future coastal population growth and exposure to sea-level rise and coastal flooding-a global assessment. *PloS one*, 10(3), e0118571.
- Nguyen, D. T., Ofli, F., Imran, M., & Mitra, P. (2017, July). Damage assessment from social media imagery data during disasters. In *Proceedings of the 2017*

- IEEE/ACM International Conference on Advances in Social Networks Analysis and Mining 2017* (pp. 569-576). ACM.
- NOAA Earth Observation Group, OLS – Operational Linescan System. (2018). Retrieved from: <https://ngdc.noaa.gov/eog/sensors/ols.html>.
- NOAA's National Weather Service, 2018. Retrieved from: Available: <http://www.nws.noaa.gov/hic/>.
- Office of Inspector General. (2017). FEMA Needs to Improve Management of Its Flood Mapping Programs (Report No. OIG-17-110). Retrieved from <https://www.oig.dhs.gov/sites/default/files/assets/2017/OIG-17-110-Sep17.pdf>
- Ofli, F., Meier, P., Imran, M., Castillo, C., Tuia, D., Rey, N., ... & Joost, S. (2016). Combining human computing and machine learning to make sense of big (aerial) data for disaster response. *Big data*, 4(1), 47-59.
- Ord, J. K., & Getis, A. (1995). Local spatial autocorrelation statistics: distributional issues and an application. *Geographical analysis*, 27(4), 286-306.
- OSM, 2019a. Stats – OpenStreetMap Wiki [online]. Available from: <http://wiki.openstreetmap.org/wiki/Statistics>
- OSM, 2019b. Tag:landuse=residential – OpenStreetMap Wiki [online]. Available from: <https://wiki.openstreetmap.org/wiki/Tag:landuse%3Dresidential>
- Ouyang, X., Zhou, P., Li, C. H., & Liu, L. (2015, October). Sentiment analysis using convolutional neural network. In *Computer and Information Technology; Ubiquitous Computing and Communications; Dependable, Autonomic and Secure Computing; Pervasive Intelligence and Computing (CIT/IUCC/DASC/PICOM)*, 2015 IEEE International Conference on (pp. 2359-2364). IEEE.
- Pandey, B., Joshi, P. K., & Seto, K. C. (2013). Monitoring urbanization dynamics in India using DMSP/OLS night time lights and SPOT-VGT data. *International Journal of Applied Earth Observation and Geoinformation*, 23, 49-61.
- Pennington, J., Socher, R., & Manning, C. (2014). Glove: Global vectors for word representation. In *Proceedings of the 2014 conference on empirical methods in natural language processing (EMNLP)* (pp. 1532-1543).
- Peters, M. E., Neumann, M., Iyyer, M., Gardner, M., Clark, C., Lee, K., & Zettlemoyer, L. (2018). Deep contextualized word representations. *arXiv preprint arXiv:1802.05365*.
- Pielke Jr, R. A., & Downton, M. W. (2000). Precipitation and damaging floods: Trends in the United States, 1932–97. *Journal of Climate*, 13(20), 3625-3637.

- Qiang, Y., Lam, N. S., Cai, H., & Zou, L. (2017). Changes in exposure to flood hazards in the United States. *Annals of the American Association of Geographers*, 107(6), 1332-1350.
- Resch, B., Usländer, F., & Havas, C. (2018). Combining machine-learning topic models and spatiotemporal analysis of social media data for disaster footprint and damage assessment. *Cartography and Geographic Information Science*, 45(4), 362-376.
- Rudari, R., Silvestro, F., Campo, L., Rebora, N., Boni, G., & Herold, C. (2015). Improvement of the Global Food Model for the GAR 2015. United Nations Office for Disaster Risk Reduction (UNISDR), Centro Internazionale in Monitoraggio Ambientale (CIMA), UNEP GRID-Arendal (GRID-Arendal): Geneva, Switzerland, 69.
- Rufat, S., Tate, E., Burton, C. G., & Maroof, A. S. (2015). Social vulnerability to floods: Review of case studies and implications for measurement. *International Journal of Disaster Risk Reduction*, 14, 470-486.
- Ruiz Sinoga, J. D., & León Gross, T. (2013). Droughts and their social perception in the mass media (southern Spain). *International Journal of Climatology*, 33(3), 709-724.
- Sakaki, T., Okazaki, M., & Matsuo, Y. (2010, April). Earthquake shakes Twitter users: real-time event detection by social sensors. In *Proceedings of the 19th international conference on World wide web* (pp. 851-860). ACM.
- Sanders, B. F. (2007). Evaluation of on-line DEMs for flood inundation modeling. *Advances in water resources*, 30(8), 1831-1843.
- Schmidt, C. W. (2012). Trending now: using social media to predict and track disease outbreaks. *Environmental health perspectives*, 120(1), a30.
- Schnebele, E., & Cervone, G. (2013). Improving remote sensing flood assessment using volunteered geographical data.
- Schnebele, E., & Waters, N. (2014). Road assessment after flood events using non-authoritative data. *Natural Hazards and Earth System Sciences*, 14(4), 1007.
- Schnebele, E., Cervone, G., Kumar, S., & Waters, N. (2014). Real time estimation of the Calgary floods using limited remote sensing data. *Water*, 6(2), 381-398.
- Sen, P. K. (1968). Estimates of the regression coefficient based on Kendall's tau. *Journal of the American statistical association*, 63(324), 1379-1389.
- Serengil, S. L. (2018, March 12). Transfer Learning in Keras Using Inception V3. Retrieved June 12, 2018, from <https://sefiks.com/2017/12/10/transfer-learning-in-keras-using-inception-v3/>.

- Shao, Z., & Liu, C. (2014). The integrated use of DMSP-OLS nighttime light and MODIS data for monitoring large-scale impervious surface dynamics: A case study in the Yangtze River Delta. *Remote Sensing*, 6(10), 9359-9378.
- Simonyan, K., & Zisserman, A. (2014). Very deep convolutional networks for large-scale image recognition. *arXiv preprint arXiv:1409.1556*.
- Slavkovikj, V., Verstockt, S., Van Hoecke, S., & Van de Walle, R. (2014). Review of wildfire detection using social media. *Fire safety journal*, 68, 109-118.
- Sloan, L., & Morgan, J. (2015). Who tweets with their location? Understanding the relationship between demographic characteristics and the use of geoservices and geotagging on Twitter. *PloS one*, 10(11), e0142209.
- Sloan, L., Morgan, J., Housley, W., Williams, M., Edwards, A., Burnap, P., & Rana, O. (2013). Knowing the Tweeters: Deriving sociologically relevant demographics from Twitter. *Sociological research online*, 18(3), 1-11.
- Smith, L. C. (1997). Satellite remote sensing of river inundation area, stage, and discharge: A review. *Hydrological processes*, 11(10), 1427-1439.
- Songchitruksa, P., & Zeng, X. (2010). Getis–Ord spatial statistics to identify hot spots by using incident management data. *Transportation research record*, 2165(1), 42-51.
- Spruce, J. P., Gasser, G. E., & Hargrove, W. W. (2016). MODIS NDVI Data, Smoothed and Gap-filled, for the Conterminous US: 2000-2014. ORNL Distributed Active Archive Center Available at: <https://daac.ornl.gov/cgi-bin/dsviewer.pl>.
- Srivastava, N., Hinton, G., Krizhevsky, A., Sutskever, I., & Salakhutdinov, R. (2014). Dropout: A simple way to prevent neural networks from overfitting. *The Journal of Machine Learning Research*, 15(1), 1929-1958.
- Stefanidis, A., Crooks, A., & Radzikowski, J. (2013). Harvesting ambient geospatial information from social media feeds. *GeoJournal*, 78(2), 319-338.
- Stewart, M. G., Rosowsky, D. V., & Huang, Z. (2003). Hurricane risks and economic viability of strengthened construction. *Natural hazards review*, 4(1), 12-19.
- Sutskever, I., Vinyals, O., & Le, Q. V. (2014). Sequence to sequence learning with neural networks. In *Advances in neural information processing systems* (pp. 3104-3112).
- Sutton, J. N., Palen, L., & Shklovski, I. (2008). Backchannels on the front lines: Emergency uses of social media in the 2007 Southern California Wildfires (pp. 624-632). University of Colorado.
- Szegedy, C., Ioffe, S., Vanhoucke, V., & Alemi, A. A. (2017, February). Inception-v4, inception-resnet and the impact of residual connections on learning. In *AAAI* (Vol. 4, p. 12).

- Szegedy, C., Liu, W., Jia, Y., Sermanet, P., Reed, S., Anguelov, D., ... & Rabinovich, A. (2015). Going deeper with convolutions. In Proceedings of the IEEE conference on computer vision and pattern recognition (pp. 1-9).
- Szegedy, C., Vanhoucke, V., Ioffe, S., Shlens, J., & Wojna, Z. (2016). Rethinking the inception architecture for computer vision. In Proceedings of the IEEE Conference on Computer Vision and Pattern Recognition (pp. 2818-2826).
- Tai, K. S., Socher, R., & Manning, C. D. (2015). Improved semantic representations from tree-structured long short-term memory networks. *arXiv preprint arXiv:1503.00075*.
- Tan, M. (2016). Use of an inside buffer method to extract the extent of urban areas from DMSP/OLS nighttime light data in North China. *Giscience & Remote Sensing*, 53(4), 444-458.
- Tang, Z., Zhang, L., Xu, F., & Vo, H. (2015). Examining the role of social media in California's drought risk management in 2014. *Natural Hazards*, 79(1), 171-193.
- Theobald, D. M. (2014). Development and applications of a comprehensive land use classification and map for the US. *PloS one*, 9(4), e94628.
- Tran, P., Shaw, R., Chantry, G., & Norton, J. (2009). GIS and local knowledge in disaster management: a case study of flood risk mapping in Viet Nam. *Disasters*, 33(1), 152-169.
- Trigg, M. A., Birch, C. E., Neal, J. C., Bates, P. D., Smith, A., Sampson, C. C., ... & Ward, P. J. (2016). The credibility challenge for global fluvial flood risk analysis. *Environmental Research Letters*, 11(9), 094014.
- Triglav-Čekada, M., & Radovan, D. (2013). Using volunteered geographical information to map the November 2012 floods in Slovenia. *Natural Hazards and Earth System Sciences Discussions*, 1(3), 2859-2881.
- Tucker, C. J., Pinzon, J. E., Brown, M. E., Slayback, D. A., Pak, E. W., Mahoney, R., ... & El Saleous, N. (2005). An extended AVHRR 8-km NDVI dataset compatible with MODIS and SPOT vegetation NDVI data. *International Journal of Remote Sensing*, 26(20), 4485-4498.
- Twitter MAU in the United States 2018 | Statistic. (n.d.). Retrieved August 21, 2018, retrieved from <https://www.statista.com/statistics/274564/monthly-active-twitter-users-in-the-united-states/>
- U.S Census Bureau. (2018). Retrieved from: <https://www.census.gov/topics/population.html>.
- Vadicamo, L., Carrara, F., Cimino, A., Cresci, S., Dell'Orletta, F., Falchi, F., & Tesconi, M. (2017). Cross-media learning for image sentiment analysis in the wild.

- In *Proceedings of the IEEE International Conference on Computer Vision* (pp. 308-317).
- Van der Sande, C. J., De Jong, S. M., & De Roo, A. P. J. (2003). A segmentation and classification approach of IKONOS-2 imagery for land cover mapping to assist flood risk and flood damage assessment. *International Journal of applied earth observation and geoinformation*, 4(3), 217-229.
- Vecchi, G. A., & Knutson, T. R. (2018). "Historical Changes in Atlantic Hurricane and Tropical Storms". Retrieved from: <https://www.gfdl.noaa.gov/historical-atlantic-hurricane-and-tropical-storm-records/>.
- Verma, S., Vieweg, S., Corvey, W. J., Palen, L., Martin, J. H., Palmer, M., ... & Anderson, K. M. (2011, July). Natural language processing to the rescue? extracting "situational awareness" tweets during mass emergency. In *Fifth International AAAI Conference on Weblogs and Social Media*.
- Viero, D. P., Roder, G., Matticchio, B., Defina, A., & Tarolli, P. (2019). Floods, landscape modifications and population dynamics in anthropogenic coastal lowlands: The Polesine (northern Italy) case study. *Science of The Total Environment*, 651, 1435-1450.
- Vieweg, S., Hughes, A. L., Starbird, K., & Palen, L. (2010, April). Microblogging during two natural hazards events: what twitter may contribute to situational awareness. In *Proceedings of the SIGCHI conference on human factors in computing systems* (pp. 1079-1088). ACM.
- Villarini, G., Vecchi, G. A., Knutson, T. R., & Smith, J. A. (2011). Is the recorded increase in short-duration North Atlantic tropical storms spurious?. *Journal of Geophysical Research: Atmospheres*, 116(D10).
- Wang, C., Li, Z., & Huang, X. (2018). Geospatial assessment of wetness dynamics in the October 2015 SC flood with remote sensing and social media. *southeastern geographer*, 58(2), 164-180.
- Wang, T., Wu, D. J., Coates, A., & Ng, A. Y. (2012, November). End-to-end text recognition with convolutional neural networks. In *Pattern Recognition (ICPR), 2012 21st International Conference on* (pp. 3304-3308). IEEE.
- Wang, Y., Colby, J. D., & Mulcahy, K. A. (2002). An efficient method for mapping flood extent in a coastal floodplain using Landsat TM and DEM data. *International Journal of Remote Sensing*, 23(18), 3681-3696.
- Wardrop, N. A., Jochem, W. C., Bird, T. J., Chamberlain, H. R., Clarke, D., Kerr, D., ... & Tatem, A. J. (2018). Spatially disaggregated population estimates in the absence of national population and housing census data. *Proceedings of the National Academy of Sciences*, 115(14), 3529-3537.

- Wing, O. E., Bates, P. D., Smith, A. M., Sampson, C. C., Johnson, K. A., Fargione, J., & Morefield, P. (2018). Estimates of present and future flood risk in the conterminous United States. *Environmental Research Letters*, 13(3), 034023.
- Woznicki, S. A., Baynes, J., Panlasigui, S., Mehaffey, M., & Neale, A. (2019). Development of a spatially complete floodplain map of the conterminous United States using random forest. *Science of the total environment*, 647, 942-953.
- Xu, H. (2008). A new index for delineating built-up land features in satellite imagery. *International Journal of Remote Sensing*, 29(14), 4269-4276.
- Xu, Z., Liu, Y., Yen, N., Mei, L., Luo, X., Wei, X., & Hu, C. (2016). Crowdsourcing based description of urban emergency events using social media big data. *IEEE Transactions on Cloud Computing*.
- Yager, J., Peri, C., & Rosoff, S. (2017). Population in the U.S floodplains (Rep.). NYU Furman Center.
- Yates, D., & Paquette, S. (2010, October). Emergency knowledge management and social media technologies: A case study of the 2010 Haitian earthquake. In *Proceedings of the 73rd ASIS&T Annual Meeting on Navigating Streams in an Information Ecosystem-Volume 47* (p. 42). American Society for Information Science.
- Yi, K., Tani, H., Li, Q., Zhang, J., Guo, M., Bao, Y., ... & Li, J. (2014). Mapping and evaluating the urbanization process in northeast China using DMSP/OLS nighttime light data. *Sensors*, 14(2), 3207-3226.
- Yih, W. T., He, X., & Meek, C. (2014). Semantic parsing for single-relation question answering. In *Proceedings of the 52nd Annual Meeting of the Association for Computational Linguistics (Volume 2: Short Papers)* (Vol. 2, pp. 643-648).
- Yin, J., Lampert, A., Cameron, M., Robinson, B., & Power, R. (2012). Using social media to enhance emergency situation awareness. *IEEE Intelligent Systems*, 27(6), 52-59.
- Yosinski, J., Clune, J., Bengio, Y., & Lipson, H. (2014). How transferable are features in deep neural networks?. In *Advances in neural information processing systems* (pp. 3320-3328).
- You, Q., Luo, J., Jin, H., & Yang, J. (2016, February). Cross-modality consistent regression for joint visual-textual sentiment analysis of social multimedia. In *Proceedings of the Ninth ACM International Conference on Web Search and Data Mining* (pp. 13-22). ACM.
- Yu, B., Shu, S., Liu, H., Song, W., Wu, J., Wang, L., & Chen, Z. (2014). Object-based spatial cluster analysis of urban landscape pattern using nighttime light satellite images: A case study of China. *International Journal of Geographical Information Science*, 28(11), 2328-2355.

- Yue-Hei Ng, J., Hausknecht, M., Vijayanarasimhan, S., Vinyals, O., Monga, R., & Toderici, G. (2015). Beyond short snippets: Deep networks for video classification. In *Proceedings of the IEEE conference on computer vision and pattern recognition* (pp. 4694-4702).
- Zha, Y., Gao, J., & Ni, S. (2003). Use of normalized difference built-up index in automatically mapping urban areas from TM imagery. *International journal of remote sensing*, 24(3), 583-594.
- Zhang, Q., Li, B., Thau, D., & Moore, R. (2015). Building a better urban picture: Combining day and night remote sensing imagery. *Remote Sensing*, 7(9), 11887-11913.
- Zhang, Q., Schaaf, C., & Seto, K. C. (2013). The vegetation adjusted NTL urban index: A new approach to reduce saturation and increase variation in nighttime luminosity. *Remote Sensing of Environment*, 129, 32-41.
- Zhang, Y., & Wallace, B. (2015). A sensitivity analysis of (and practitioners' guide to) convolutional neural networks for sentence classification. *arXiv preprint arXiv:1510.03820*.
- Zhou, Y., Smith, S. J., Elvidge, C. D., Zhao, K., Thomson, A., & Imhoff, M. (2014). A cluster-based method to map urban area from DMSP/OLS nightlights. *Remote Sensing of Environment*, 147, 173-185.
- Zikopoulos, P., & Eaton, C. (2011). *Understanding big data: Analytics for enterprise class hadoop and streaming data*. McGraw-Hill Osborne Media.

APPENDIX A

SUPPORTING TABLES

Table A.1 Available land use categories in NLUD 2010.

Land use major type	Subcategories
Water	Natural – area (lake, swamp, and playa) Human – area (reservoir) Natural – linear (river and wash) Human – linear (canal/ditch) Estuary (Estuary/complex channels) Wetlands Ocean (open ocean and bay inlet)
Build-up	Residential Commercial (office, retail/shopping centers, entertainment, and lodge) Industrial (factory/plant, landfill, confined animal feeding, and utilities) Institutional (school, medical, government/public, military, fire/police stations, church, and prison) Transportation (airports, highway/railway, port, train station, other transportation and undeveloped) Miscellaneous (cemetery and rural buildings)
Production	General (general agricultural) Cropland (cropland/row crops, pastureland, orchards, sod/switch grass, and aquaculture) Rangeland (grazed and stock tank) Mining (mining strip mines, quarries, gravel pits, and mine shifts) Timber (timber harvest and timber plantations) Extraction/barren land (oil/gas wells and misc. barren)
Recreation	Undifferentiated park (general park) Developed park (urban park, golf course, motorized, OHV Staging area/trailhead, resort/ski area, Marina, campground/ranger station, picnic/trailhead, and boat/fishing access) Natural park (natural park, designated recreation area, and designated scenic area)
Conversation	Public (wildlife habitat, conservation area, natural reserve, wilderness, areas of Critical Env. Concerns, Research Natural Area,

fish/wildlife service area, archaeology/historical/ scenic area, and wild/scenic river)
 Public-limited access (municipal watershed, Corps of Engineers dam and marine protected area)
 Private easement (wildlife conservation and agricultural conservation)

Note. This table was summarized from Theobald (2014)

Table A.2 OSM land use statistics in CONUS

Land use class	Total records	Total size (km^2)	Land use class	Total records	Total size (km^2)
Allotments	1,681	4.52	Industrial	52,537	9,079.45
Commercial	64,216	2,949.86	Meadow	42,615	23,430.72
Farm	186,297	73,989.69	Military	3,124	112,921.92
Forest	358,426	274,690.80	Natural reserve	27,215	683926.68
Grass	262,348	2,356.47	Orchard	18,259	3583.34
Park	124,472	34,573.64	Quarry	7119	4,197.45
Recreation Ground	21,545	3,238.34	Residential	373,261	42,348.51
Retail	42,913	2,164.11	Scrub	62,416	13,940.30
Vineyard	15,137	1,847.07	Cemetery	45,904	1,529.74
Health	4,587	16,063.60			

Note. OSM data used in this study was downloaded on March 1st, 2019.

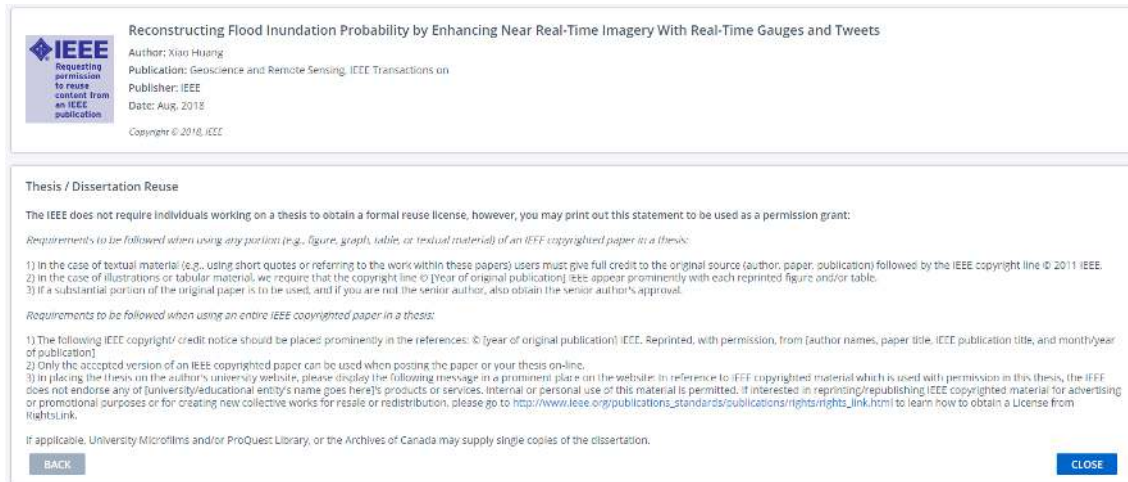
Table A.3 Detailed profile of population statistics exposed to 100-year floodplains in the CONUS

Category	Subcategory	100-year floodplain (F/P)			100-year floodplains (F/P + Coastal)	
		(in thousands)			(in thousands)	
		FEMA (F/P)	JRC	GAR	FEMA (F/P + Coastal)	RFC ON
Age	Under 5	650	776	841	655	713
	5 to 14	1,307	1,566	1,779	1,316	1,469
	14 to 25	1,395	1,662	1,892	1,405	1,577
	25 to 34	1,487	1,725	1,711	1,499	1,579
	35 to 44	1,362	1,503	1,629	1,374	1,454
	45 to 54	1,472	1,565	1,838	1,489	1,600
	55 to 64	1,441	1,526	1,952	1,463	1,637
	65 to 74	1,067	1,023	1,443	1,090	1,185
	75 to 84	572	523	769	585	613
	Above 85	239	223	307	243	254
Race	White	8,296	8,672	11,741	8,412	9,604

	Black or African American	1,390	1,734	1,359	1,395	1,115
	American Indian and Alaska native	70	114	254	71	141
	Asian	433	610	149	435	402
	Native Hawaiian and Pacific Islander	11	20	9	11	13
	Some other races	512	589	317	514	468
	Two or more races	280	351	333	282	338
Ethnicity	Hispanic or Latino	2,712	2,727	1,455	2,724	2,142
	Not Hispanic or Latino	8,281	9,364	12,706	8,396	9,938
Employment	Employed	4,959	5,399	6,032	5,013	5,422
	Unemployed	373	434	455	376	395
Tenure	Owner Occupied	2,547	2,685	3,761	2,590	3,021
	Renter Occupied	1,600	1,803	1,744	1,615	1,664
Poverty	Under 1.0	1,804	2,274	2,478	1,817	1,911
	1.00 to 1.99	2,185	2,523	3,012	2,201	2,300
	Above 2	6,747	6,975	8,170	6,841	7,566

APPENDIX B

MANUSCRIPT COPYRIGHT RELEASE



Reconstructing Flood Inundation Probability by Enhancing Near Real-Time Imagery With Real-Time Gauges and Tweets

Author: Xiao Huang
Publication: Geoscience and Remote Sensing, IEEE Transactions on
Publisher: IEEE
Date: Aug, 2018
Copyright © 2018, IEEE

Requesting permission to reuse content from an IEEE publication

Thesis / Dissertation Reuse

The IEEE does not require individuals working on a thesis to obtain a formal reuse license, however, you may print out this statement to be used as a permission grant:

Requirements to be followed when using any portion (e.g., figure, graph, table, or textual material) of an IEEE copyrighted paper in a thesis:

- 1) In the case of textual material (e.g., using short quotes or referring to the work within these papers) users must give full credit to the original source (author, paper, publication) followed by the IEEE copyright line © 2011 IEEE.
- 2) In the case of illustrations or tabular material, we require that the copyright line © [Year of original publication] IEEE appear prominently with each reprinted figure and/or table.
- 3) If a substantial portion of the original paper is to be used, and if you are not the senior author, also obtain the senior author's approval.

Requirements to be followed when using an entire IEEE copyrighted paper in a thesis:

- 1) The following IEEE copyright/ credit notice should be placed prominently in the references: © [year of original publication] IEEE. Reprinted, with permission, from [author names, paper title, IEEE publication title, and month/year of publication]
- 2) Only the accepted version of an IEEE copyrighted paper can be used when posting the paper or your thesis on-line.
- 3) In placing the thesis on the author's university website, please display the following message in a prominent place on the website: In reference to IEEE copyrighted material which is used with permission in this thesis, the IEEE does not endorse any of [university/educational entity's name goes here]'s products or services. Internal or personal use of this material is permitted. If interested in reprinting/republishing IEEE copyrighted material for advertising or promotional purposes or for creating new collective works for resale or redistribution, please go to http://www.ieee.org/publications_standards/publications/rights/rights_link.html to learn how to obtain a License from Rightslink.

If applicable, University Microfilms and/or ProQuest Library, or the Archives of Canada may supply single copies of the dissertation.

[BACK](#) [CLOSE](#)

Figure B.1 Screenshot of copyright clearance from IEEE Transactions on Geoscience and Remote Sensing.



Identifying disaster related social media for rapid response: a visual-textual fused CNN architecture

Author: Xiao Huang, . . . et al
Publication: International Journal of Digital Earth
Publisher: Taylor & Francis
Date: Jun 23, 2019
Rights managed by Taylor & Francis

Taylor & Francis
Taylor & Francis Group

Thesis/Dissertation Reuse Request

Taylor & Francis is pleased to offer reuses of its content for a thesis or dissertation free of charge contingent on resubmission of permission request if work is published.

[BACK](#) [CLOSE](#)

Figure B.2 Screenshot of copyright clearance from International Journal of Digital Earth.

Licence and copyright agreement



[Author's certification](#) ▶

[Copyright](#) ▶


- Authors retain the copyright of the article. Regarding copyright transfers please see below.
- Authors grant Copernicus Publications an irrevocable non-exclusive licence to publish the article electronically and in print format and to identify itself as the original publisher.
- Authors grant Copernicus Publications commercial rights to produce hardcopy volumes of the journal for sale to libraries and individuals.
- Authors grant any third party the right to use the article freely as long as its original authors and citation details are identified.
- The article is distributed under the [Creative Commons Attribution 4.0 License](#). Unless otherwise stated, associated published material is distributed under the same licence:

[Creative Commons Attribution 4.0 License](#)

You are free to:

-  **Share** — copy and redistribute the material in any medium or format
-  **Adapt** — remix, transform, and build upon the material for any purpose, even commercially.

Under the following conditions:

-  **Attribution** — You must give appropriate credit, provide a link to the licence, and indicate if changes were made. You may do so in any reasonable manner, but not in any way that suggests the licensor endorses you or your use.

No additional restrictions — You may not apply legal terms or technological measures that legally restrict others from doing anything the licence permits.

[Copyright transfers](#) ▶

Many authors have strict regulations in their contract of employment regarding their works. A transfer of copyright to the institution or company, as well as the reservation of specific usage rights, is typical. Please note that in the case of open-access publications in combination with a Creative Commons License, a transfer of the **copyright** to the institution is possible, as it belongs to the author anyway and is not subject to the publisher.

Any **usage rights** are regulated through the Creative Commons License. As Copernicus Publications uses the Creative Commons Attribution 4.0 License, anyone (the author, their institution/company, the publisher, as well as the public) is free to copy, distribute, transmit, and adapt the work as long as the original author is given credit (see above). Therefore, specific usage rights cannot be reserved by the author or their institution/company, and the publisher cannot include a statement "all rights reserved" in any published paper.

A copyright transfer from the author to their institution/company must be expressed in a special "copyright statement" according to our manuscript preparation guidelines. Authors are asked to include the following sentence: "The author's copyright for this publication is transferred to *institution/company*".

[Crown copyright](#) ▶

The licence and copyright agreement of Copernicus Publications respects the Crown copyright. For works written by authors affiliated with the British Government and its institutions, a copyright statement must be included according to our manuscript preparation guidelines. Authors are asked to use the following statement, which has been approved by the Information Policy department of The National Archives:

The works published in this journal are distributed under the Creative Commons Attribution 4.0 License. This licence does not affect the Crown copyright work, which is re-usable under the Open Government Licence (OGL). The Creative Commons Attribution 4.0 License and the OGL are interoperable and do not conflict with, reduce or limit each other.

© Crown copyright YEAR

[Reproduction request](#) ▶

All articles published by Copernicus Publications have been licenced under the Creative Commons Attribution 4.0 License since 6 June 2017 or under its former version 3.0 since 10 December 2007. Under these licences the authors retain the copyright. There is no need from the publisher's side to allow/confirm a reproduction. We suggest contacting the authors to inform them about the further usage of the material. In any case, the authors must be given credit. If articles contain figures, maps, or other objects cited by the authors, the individual copyrights and distribution licences must be clarified individually.

Figure B.3 Screenshot of copyright clearance from Natural Hazards and Earth System Sciences.